BERGISCHE UNIVERSITÄT
WUPPERTAL

FACHBEREICH C
Mathematik und
Naturwissenschaften

Finite-Size Effects in Lattice QCD with Dynamical Wilson Fermions

Dissertation
zur Erlangung des Doktorgrades
des Fachbereichs Mathematik und Naturwissenschaften
(Fachrichtung Physik)
der Bergischen Universität Wuppertal

vorgelegt von

Boris Orth

aus Trier

WUB-DIS 2004-03

Juni 2004

Abstract

Due to limited computing resources choosing the parameters for a full lattice QCD simulation always amounts to a compromise between the competing objectives of a lattice spacing as small, quarks as light, and a volume as large as possible. Aiming at pushing unquenched simulations with the standard Wilson action towards the computationally expensive regime of small quark masses, the GRAL project addresses the question whether computing time can be saved by sticking to lattices with rather modest numbers of grid sites and extrapolating the finite-volume results to the infinite volume (prior to the usual chiral and continuum extrapolations). In this context we investigate in this work finite-size effects in simulated light hadron masses. Understanding their systematic volume dependence may not only help saving computer time in light quark simulations with the Wilson action, but also guide future simulations with dynamical chiral fermions which for a foreseeable time will be restricted to rather small lattices.

We analyze data from hybrid Monte Carlo simulations with the $N_f = 2$ Wilson action at two values of the coupling parameter, $\beta = 5.6$ (lattice spacing $a \approx 0.08\,\mathrm{fm}$) and $\beta = 5.32144$ ($a \approx 0.13\,\mathrm{fm}$). The larger β corresponds to the coupling used previously by SESAM/TχL. The considered hopping parameters $\kappa = 0.1575, 0.158$ (at the larger β) and $\kappa = 0.1665$ (at the smaller β) correspond to quark masses of 85, 50 and 36% of the strange quark mass, respectively. At each quark mass we study at least three different lattice extents in the range from $L = 10$ to $L = 24$ (0.85–2.04 fm). Estimates of autocorrelation times in the stochastic updating process and of the computational cost of every run are given. For each simulated sea quark mass we calculate quark propagators and hadronic correlation functions in order to extract the pion, rho and nucleon masses as well as the pion decay constant and the quark mass from the PCAC relation. We examine to what extent the volume dependence of the masses can be parameterized by simple functions based on M. Lüscher's analytic formula and previous numerical findings by other groups. The applicability of results for the pion and the nucleon from chiral effective theory in the parameter regime covered by our simulations is discussed. Cut-off effects in the PCAC quark mass are found to be under control.

Contents

Introduction

Most of the matter around us is made out of protons and neutrons which are bound by the strong force to form the nuclei of atoms. In the current view, nucleons (and *hadrons* in general) are themselves bound states and the strong force between them is, fundamentally, an interaction between *quarks*, mediated by *gluons*. The masses of the three valence quarks that form a nucleon are astonishingly small compared to the total mass of the bound state: taken together, the masses of the constituent quarks account for only about one percent of the nucleon mass [1]. This, in turn, has the remarkable implication that 99% of the nucleon mass are a consequence of the strong interaction.

The commonly accepted theory of the strong interaction, formulated in terms of gluons and quarks, is Quantum Chromodynamics (QCD) [2]. Together with the Glashow-Weinberg-Salam (GWS) theory [3] of the electroweak interactions it constitutes today's *Standard Model* of elementary particle physics [4, 5]. Like the GWS model, QCD is a renormalizable quantum field theory built on the principle of local gauge invariance [6, 7]. At first sight the QCD Lagrangian appears relatively simple, because it has only few parameters and possesses a number of convenient symmetry properties. But while the masses and many other properties of light hadrons (like the nucleon) are very precisely known from experiment, it turns out that on the theoretical side it is difficult to calculate them from first principles.

This is, on the one hand, due to the fact that the "color" gauge group $SU(3)$ of QCD is non-Abelian. Unlike the photon in Quantum Electrodynamics (QED) with Abelian gauge group $U(1)$, the gluons as the gauge bosons of QCD interact with themselves. This renders the basic equations non-linear. On the other hand, the strong coupling constant α_s is simply not small at low energies, so that perturbation theory, which has proven so immensely successful in QED, cannot be applied *e.g.* in the calculation of light hadron masses. This generally prevents us from testing QCD to the precision that has been achieved in the electroweak sector—perhaps with the notable exception of some aspects that are governed by the (approximate) chiral and flavor symmetries. But there is another important difference between QED and QCD that rescues the Feynman calculus as a legitimate tool for QCD at least in the high energy regime: while in QED the coupling strength grows—though only weakly—with increasing energy, QCD is *asymptotically free*, meaning that towards large energies the strong coupling vanishes and the quarks behave at short distances like "quasi" free particles [8]. Nevertheless it is an experimentally well-established fact that neither quarks nor gluons are asymptotic states, and even in the incoming and outgoing states of short-distance "hard" processes like deep inelastic scattering they appear only *confined* within hadrons, color-singlet objects composed of two (*mesons*) or three (*baryons*) valence quarks.[1] Confinement involves the long-range, infrared behavior of the quark-quark interaction, but this is precisely where perturbation theory fails. To really show that,

[1] Similarly, gluons are presumed to exist only within hadrons, and possibly as color-neutral *glueballs*.

as it is widely believed, QCD entails a dynamical explanation for quark confinement [9], and that the same Lagrangian that correctly describes the interaction between quarks and gluons at high energies also explains the spectrum and the properties of light hadrons, obviously requires a non-perturbative approach. Currently, the only non-perturbative method for *solving* rather than just *modeling* the theory is the numerical simulation of Lattice QCD (LQCD) [10, 11, 12].

The formulation of QCD on a discrete lattice in Euclidean space-time was first proposed by Wilson in 1974 [13]. The starting point of the lattice approach is the functional quantization of the classical theory. In the Feynman path-integral framework, expectation values of observables are obtained by integrating over all possible system "configurations", weighted according to their relative "importance" [14]. After an analytic continuation of the time variable to imaginary values the weight of a given configuration is determined by a real-valued exponential of the Euclidean action analogous to the Boltzmann factor in statistical mechanics. Discretizing space-time now renders the theory mathematically well-defined in two respects: First of all, the discrete space-time grid provides a non-perturbative, gauge invariant regularization scheme. The lattice spacing a introduces an ultraviolet momentum cut-off at π/a, so that for finite values of a there are no infinities. Secondly, it reduces the functional integral to a large but finite number of bounded integrals over the compact gauge group that can be evaluated stochastically using well-established Monte Carlo methods. In practice, these methods are implemented on massively parallel computers in order to generate importance-sampled sets of gauge field configurations that are to serve as "background" fields for the calculation of quark propagators, hadronic correlation functions and, eventually, expectation values of observables. Apart from the number of grid sites the only physically relevant, tunable input parameters of such a computer simulation are the bare parameters of the QCD Lagrangian, *i.e.* the quark masses and the gauge coupling.

Due to deeper physical insight, improved algorithmic strategies and increased computer power, lattice gauge theory has by now matured into a powerful tool for non-perturbative *ab initio* calculations in QCD that can often be compared to experiment (see *e.g.* [15]). Since no heuristic model assumptions or uncontrolled approximations are needed, the lattice theory retains the fundamental character of QCD and thus provides a reliable test bed for the theory. However, computer resources are still a limiting factor for the accuracy of the numerical results, so that apart from the statistical errors that inevitably occur in any stochastic simulation, there are a number of systematic uncertainties. Perhaps the most obvious source of systematic error is the nonzero lattice spacing a. As it is connected to the bare coupling g through the renormalization group equation, the Callan-Symanzik β-function governs the flow of g as a function of the associated momentum cut-off a^{-1}. There is compelling evidence that in QCD the strong coupling g approaches zero as $a \to 0$ without a phase transition at intermediate values of g, and so the continuum limit can in principle be obtained by computing the quantities of interest for several values of a and extrapolating the results to $a = 0$. Since the computational cost grows with decreasing a, one cannot perform numerical simulations at arbitrary small lattice spacings, however. In fact, current lattice spacings in hadron mass calculations, for example, are usually not much smaller than 0.1 fm. Recent years have seen a number of attempts to reduce discretization errors and accelerate the approach to the continuum limit by "improving" the lattice action and operators.[2] Most of these methods have been built around Symanzik's early idea of including additional operators into the action to systematically remove lattice artefacts up to a given order in the lattice spacing [16]. The disadvantage of improved actions, however, is that they are computationally more demanding and in general more complicated to handle.

[2]The way in which the action is regularized by discretization is not unique. In principle, any bare action in the same universality class as QCD will produce universal results in the continuum limit.

Another limitation of lattice QCD lies in the quark masses that can be simulated on current computers. In order to accommodate light hadrons in currently feasible lattice volumes of about $(2-3\,\mathrm{fm})^3$, the simulated quarks must be considerably heavier than the physical u and d quarks. While, typically, their masses are of the order of the strange quark mass, recent exploratory simulations by UKQCD [17], the qq+q collaboration [18] and CP-PACS [19] have reached sea quark masses as small as $m_s/3$, $m_s/4$ and $m_s/7$, respectively.[3] The computational argument for simulating unphysically heavy quarks is twofold: First of all, the generation of gluon field configurations with the widely used Hybrid Monte Carlo (HMC) algorithm [20] necessitates the repeated inversion of a huge Dirac matrix, the cost of which grows significantly towards smaller quark masses [21, 22, 23]. Secondly, simulations with Wilson's action are increasingly affected by statistical fluctuations as the quark mass is decreased. The first problem can be circumvented by using the "quenched approximation" in which the fermionic determinant is omitted from the action, and which in physical terms amounts to completely neglecting sea quark polarization effects in the QCD vacuum ($N_f = 0$). It has the advantage of reducing the computational cost by about three orders of magnitude compared to a "full" QCD simulation, but at the prize of uncontrolled systematic errors of the order of 10% in the resulting hadronic spectrum [24]. Originally adopted solely for reasons of expediency, the quenched approximation has been more and more abandoned in favor of QCD simulations with dynamical sea quarks after the advent of sufficiently fast computers. While the first obstacle can thus be overcome, in principle, by sheer computer power, the problem of fluctuations is more fundamental, as it is connected to the fact that the Wilson action breaks—at finite a—the chiral symmetry of the original QCD action. This breaking of chiral symmetry is a consequence of Wilson's fix of the notorious "fermion doubling" problem inherent in the naive discretization of the quark action [25].[4] Promising approaches that preserve an exact lattice chirality also at finite values of the lattice spacing and thus allow—at least in principle—for simulations at arbitrary small quark masses, are the *domain-wall* [29] and the *overlap* [30] formulations. Although dynamical simulations using these methods with realistic parameters are still prohibitively expensive (about a factor of 100 times the cost for the Wilson action), there is little doubt that more years will bring the computer power needed to do the calculations right (see *e.g.* [31, 32]). Until then, however, simulations with the Wilson action remain an important tool in studying full QCD.

While first results of simulations with three dynamical quark flavors are becoming available from a few collaborations [33, 34], most full QCD simulations so far have been obtained with only two mass-degenerate flavors [35, 36, 37, 38, 39, 40, 41, 66], which are usually identified with exactly isospin-symmetric u and d quarks. The original limitation to $N_f = 2$ primarily owes to the fact that the standard HMC algorithm can handle only even numbers of quark flavors, but nevertheless it is believed to be a reasonably good approximation in those cases in which only the light quarks are relevant. Physical results for quantities involving light quarks are usually obtained by extrapolating in the quark mass using functional forms derived from chiral perturbation theory (ChPT), a low-energy effective field theory in which the dynamics of the Goldstone bosons is described by an expansion in terms of momenta and quark masses [42, 43].

[3] The natural light quark mass is $\overline{m} = (m_u + m_d)/2 \approx m_s/25$.

[4] An alternative approach to the solution of the doubling problem is the Kogut-Susskind (*staggered*) action [26]. It retains a remnant of chiral symmetry also at finite lattice spacing, but at the prize of an unwanted four-fold degeneracy in flavor ("tastes"). An improved variant of the staggered action is extensively used by the HPQCD-MILC-UKQCD collaboration [27]. Very recently they have reported on three-flavor simulations with dynamical light quark masses below $m_s/2$ and down to $m_s/8$ [28]. There is, however, a fundamental concern associated with the need to take the fourth root of the quark determinant in their action to convert the four-fold duplication of "tastes" into one quark flavor.

In practice, however, there is a limited range of quark masses where both lattice simulations are feasible and ChPT is applicable. This problem can be somewhat alleviated by exploiting a particular merit of lattice QCD, namely that the valence quark masses in quark propagator calculations can be reduced independently of the sea quark mass that has been used for the generation of the underlying gluon field configurations. This is computationally less demanding and may be used in combination with partially quenched ChPT (PQChPT) to extrapolate to light valence quark masses [44, 45, 46]. PQChPT is one example for recent extensions of ChPT aiming at bridging the gap between results from the lattice and phenomenology. Another promising development in this respect is ChPT for Wilson-type quarks (WChPT), which takes the finite lattice spacing into account and in this way leads to an improved chiral extrapolation [47, 48, 49, 50].

Besides the finite lattice spacing and unphysically large quarks, the third main source of systematic error in lattice QCD is the lattice *volume*, which in any numerical simulation is necessarily finite. The finite lattice size is responsible, for example, for systematic shifts in the numerically calculated masses or decay constants of light hadrons, and exactly these shifts are what we will be mainly concerned with in this work. Since the size of a hadron may be characterized by its Compton wavelength which is inversely proportional to its mass m, and as the pion is the lightest particle in the theory, it is convenient to consider the linear spatial extent of a given lattice in units of the Compton wave length of the pion, *i.e.* in terms of $m_\pi L$. In summary, the physical picture of how finite-size effects emerge is as follows: If L is much larger than the size of a pion ($m_\pi L \gg 1$), then a single hadron is practically unaffected by the finite volume (except that its momentum must be an integer multiple of $2\pi/L$). Then, if the box size is decreased until the hadron barely fits into the box, the virtual pion cloud surrounding the particle is slightly distorted, and a pion may be exchanged "around the world" (provided that periodic boundary conditions have been imposed). A consequence of this effect is that the mass of the hadron is shifted relative to its asymptotic value by terms of order $e^{-m_\pi L}$. At still smaller values of L the quark wave functions of the enclosed hadron are squeezed and one observes rapidly increasing finite volume effects, approximately proportional to some negative power of L.

The ultimate goal of lattice QCD is of course to make physically relevant predictions at "realistic" values of the fundamental parameters, and in particular of the quark masses. In view of limited computer resources, however, the selection of parameters for numerical simulations always remains a compromise between large volume, small lattice spacing and small quark masses. Usually, in the context of spectrum calculations, extrapolations are attempted in the lattice spacing and the quark mass, whereas the physical volume is mostly chosen such that finite-size effects can be largely neglected right from the start. In this work we take a complementary approach in that we investigate, for various fixed values of the gauge coupling and quark mass, the functional volume dependence of the light hadron masses. Against the background of our "GRAL" project, whose name is an acronym for "Going Realistic And Light", we address in particular the question if and under what conditions an extrapolation in the lattice volume is possible [51, 52]. This issue is interesting in at least two respects: First of all, if one can get away with simulations on small or medium-sized lattices (followed by an extrapolation to the infinite volume), this may be helpful in reaching lighter quark masses with the Wilson action. Secondly, given that simulations with chiral fermions will become feasible in due course, they will initially be restricted to rather small volumes. Extrapolations in the lattice size will then be inevitable to obtain infinite-volume estimates of the quantities of interest.

While in recent years the chiral extrapolation and the reduction of discretization errors (by both improvement and extrapolation) have been at the center of many theoretical and numerical

studies, there have been rather few systematic investigations into the lattice size dependence of light hadron masses. These include, first of all, a seminal analytic work by M. Lüscher of 1986, in which he proved a universal formula for the asymptotic volume dependence of stable particle masses in arbitrary massive quantum field theories [53]. Later on, in a series of papers published between 1992 and 1994, Fukugita *et al.* carried out a systematic numerical investigation of finite-size effects in pion, rho and nucleon masses from quenched and unquenched simulations (with the staggered action) [56, 57, 58, 59, 60]. Related numerical studies with staggered quarks came also, at about the same time, from the MILC collaboration [61, 62, 63]. Today it appears that the systematic dependence of the light hadron masses on the lattice volume is receiving renewed attention. Beside our own work with its rather heuristic approach there have recently been important analytical contributions from effective field theory [64, 65, 66, 67, 68, 69, 70]. These include, on the one hand, a determination of the pion mass shift in finite volume using Lüscher's asymptotic formula with input from ChPT (in infinite volume) up to next-to-next-to-leading order [65]. On the other hand, the finite-size mass shift of the nucleon has been calculated using baryon ChPT in finite volume up to next-to-next-to-leading order [66]. Comparing the pion and nucleon masses from our simulations with these calculations it will be interesting to check to what extent the theoretical formulae can account for our numerical results. As it turns out, the formula for the nucleon is a promising example of how suitable parameterizations for infinite-volume extrapolations with controlled errors may possibly be found quite generally by calculating finite-size effects consistently within the very effective field theories that also describe the quark mass dependence [71, 72, 73].

The numerical investigation of finite-volume effects described in this work requires data from simulations that differ only in the lattice volume while all other bare parameters are kept fixed. The GRAL project therefore builds on and extends previous SESAM/TχL simulations [35, 36] in which gauge field configurations for 16^3 and 24^3 lattices have been generated with the Wilson action at $\beta = 5.6$ ($a \approx 0.8\,\mathrm{fm}$ from the Sommer parameter r_0 [74]). The SESAM/TχL data at $\kappa = 0.1575$ and $\kappa = 0.158$ (corresponding to quark masses of roughly 85 and 50% of the strange quark mass) have been complemented with GRAL ensembles at various smaller lattice volumes in the range from 10^3 to 16^3, using the same unimproved $N_f = 2$ Wilson action. All of the gauge field configurations considered here have been generated with variants of the SESAM HMC code in which a parallel ll-SSOR preconditioned BiCGStab solver is used for the fast inversion of the quark matrix [75, 76]. To check on the feasibility of HMC simulations with the standard Wilson action at lighter quark masses around $m_s/3$ ($m_\pi/m_\rho \approx 0.5$) we have conducted exploratory simulations on three different lattice volumes (12^3, 14^3 and 16^3) at a stronger coupling of $\beta = 5.32144$ ($a \approx 1.5\,\mathrm{fm}$). Recent related work includes that of the qq+q collaboration which employs the same unimproved $N_f = 2$ Wilson action, but uses the two-step multi-boson (TSMB) instead of the HMC algorithm [77, 78]. At a rather strong coupling of $\beta = 5.1$ ($a \approx 0.2\,\mathrm{fm}$) they have succeeded in simulating at slightly less than a third of the strange quark mass, but as they use only one lattice volume (16^3) the issue of finite-size effects is not addressed [18]. The UKQCD and JLQCD/CP-PACS collaborations, which are working with improved actions, have also tried to push their simulations towards lighter quarks [17, 19]. They have reported earlier on potential instabilities in the molecular dynamics evolution of the HMC algorithm in the regime of $m_\pi/m_\rho \lesssim 0.5$ when using step sizes that were too large [79, 80]. It is therefore an interesting question whether we will encounter such difficulties, too. The total range of linear lattice sizes covered by our simulations is approximately $0.85 - 2.04\,\mathrm{fm}$. For our investigations, more than 80 000 gauge field configurations have been newly generated on APE machines at DESY Zeuthen [81, 82] and on the cluster computer ALiCE at the University of Wuppertal [83] in addition to the readily available SESAM/TχL

ensembles. A conservative estimate of the total cost spent on the production of the GRAL ensembles results in approximately 260 Tflops-hours. All of the required quark propagators and hadronic correlation functions have been calculated on the Cray T3E [84] at FZ Jülich.

The outline of the thesis is as follows:

QCD on the Lattice

The purpose of the first chapter is to introduce the main concepts of lattice QCD and to fix the notation. After the derivation of the QCD Lagrangian we introduce the Feynman path integral as a convenient way of quantizing the classical theory such that the close analogy between quantum field theory and statistical mechanics becomes apparent. Wilson's approach to discretizing and thus regularizing the continuum QCD action in Euclidean space-time is explained. We give a cursory overview of improvement and recent developments regarding alternative actions. The basic features of the Hybrid Monte Carlo algorithm are described. We close the chapter with a list of the most important uncertainties in lattice results.

Volume Dependence of the Light Hadron Masses

In the second chapter we review the main theoretical and numerical findings published to date about the functional form and physical origin of finite-size effects in light hadron masses. Lüscher's exponential formula for the asymptotic mass shift in finite volume is quoted and discussed in some detail for the special cases of the pion and the nucleon. We recapitulate possible explanations for the observation made by Fukugita *et al.* that at small volumes the volume-dependence of the pion, rho and nucleon masses can be described by a power law. A recent result by Ali Khan *et al.* for the nucleon mass-shift from baryon chiral perturbation theory in finite volume is presented.

Numerical Simulation

The third chapter deals with the numerical aspects of our work. We describe the main features of the specific implementation of the HMC algorithm that we use for the generation of gauge field configurations, and list the run parameters of our simulations. For reference and comparison we also quote the corresponding numbers for all previous SESAM/TχL runs. Estimates of the computational costs for each run are given. We discuss the main aspects of the computation of smeared quark propagators and hadronic correlation functions and introduce the parameterizations to which these correlation functions are fitted in order to obtain the desired physical quantities. We close the chapter with an account of our methods for fitting and error analysis.

Light Hadron Spectroscopy

The fourth chapter is dedicated to the main results of this work, the analysis of finite-size effects. To set the physical scale in our simulations at $\beta = 5.32144$ we first determine the Sommer parameter r_0 from a fit of the static quark potential. We describe in detail how we obtain hadron masses and decay constants by fitting the mesonic and baryonic two-point functions to appropriate parameterizations, and how the fit ranges are optimized. The resulting masses

of the pion and rho mesons and of the nucleon (before chiral or continuum extrapolation) are given. We also present results for the (unrenormalized) pion decay constant and the bare PCAC quark mass. The role of spatial Polyakov-type loops in finite volume is discussed. To investigate the functional form of the volume-dependence of our calculated hadron masses we first examine various "naive" parameterizations motivated by Lüscher's formula and the observations made by Fukugita *et al.*. In a second step we check on the validity of available theoretical predictions from effective field theory in the parameter regime covered by our simulations. The issue of the feasibility of infinite-volume extrapolations (based on data from small and intermediate lattices) is discussed. Finally we use the PCAC quark mass to check on the role of discretization errors in our simulations.

Chapter 1

QCD on the Lattice

Quantum chromodynamics (QCD) is a renormalizable quantum field theory of the strong interaction observed between *hadrons*. Together with quantum electrodynamics (QED) and the Glashow-Salam-Weinberg (GWS) theory of electroweak processes it constitutes today's *Standard Model* of elementary particle physics. The Standard Model has the remarkable and aesthetically appealing feature that all fundamental interactions (except gravity) follow from a single general principle, the requirement of local gauge invariance. This requirement leads, respectively, to the appearance of interacting massless vector bosons that couple to appropriately charged massive fermions.[1] The gauge symmetry group of QCD is the non-Abelian "color" group $SU(3)$, and the corresponding gauge bosons, called *gluons*, belong to its adjoint representation. The massive constituents of QCD are the spin-1/2 *quarks* which transform according to the fundamental representation of the gauge group. In nature, quarks come in $N_f = 6$ different flavors called up (u), down (d), strange (s), charm (c), bottom (b) and top (t). As the latter three have masses above the GeV-scale they effectively decouple at the energy scale we are interested in, which is a few hundred MeV. In this work we will be concerned exclusively with light hadrons consisting primarily of u and d quarks (namely the pion, the rho and the nucleon), so that for our purpose it will be sufficient to consider the case $N_f = 2$.

One of the fundamental properties of QCD is the phenomenon of *asymptotic freedom*: Inside a hadron (*i.e.* at very short short distances) the quarks behave like quasi-free particles, because at the associated high momenta the strong coupling constant g tends to zero. This can be seen most clearly from the running of the coupling as expressed by the leading order perturbative solution to the renormalization group equation,

$$g^2(\Lambda) = \frac{8\pi^2}{(11 - 2/3N_f)\log(\Lambda/\Lambda_{\mathrm{QCD}})}, \tag{1.1}$$

where Λ is the momentum scale and $\Lambda_{\mathrm{QCD}} \approx 200\,\mathrm{MeV}$ the characteristic reference scale at which g becomes strong as Λ is decreased. Asymptotic freedom implies that perturbation theory is applicable in the description of hard processes such as deep inelastic scattering, when $\Lambda_{\mathrm{QCD}} \ll \Lambda$. At intermediate and low energies, however, when $\Lambda \lesssim \Lambda_{\mathrm{QCD}}$ and g is large, more and more diagrams in the Feynman diagram expansion contribute and perturbation theory breaks down. In order to calculate low-energy properties of light hadrons (like their masses or decay constants), one has to revert to a non-perturbative method like lattice QCD.

[1] The heavy mediators of the weak interaction, the $W^{\pm}$ and Z^0, acquire their masses by the *Higgs mechanism* [85].

The present chapter is intended to give a brief overview of the main aspects of lattice QCD relevant to this work. We begin with the derivation of the classical QCD Lagrangian in the continuum, using a notation that will facilitate the subsequent transcription to a lattice. Setting out from free quarks we will see how the gluons emerge as a consequence of the postulate of local gauge symmetry. We will then introduce the Feynman path integral as a way of quantizing the classical theory that is particularly convenient for lattice theories. A further ingredient of the lattice formulation is the analytic continuation of the time variable to imaginary values (Wick rotation). The discretization of the QCD action in Euclidean space-time will then both serve us as a non-perturbative regularization scheme and allow for the numerical treatment of the theory with Monte Carlo methods. In this context we will also discuss some alternatives to and modifications of the Wilson formulation of lattice QCD used in this work. We then give a brief introduction to the Hybrid Monte Carlo algorithm that we employ for the numerical evaluation of the path integral, before we conclude the chapter with a summary of typical sources of error in lattice simulations.

1.1 The QCD Lagrangian

The local Lagrangian for a free quark of flavor q with mass m_q, represented by the color-spinor field $q_c^\alpha(x)$ with $SU(3)$ color index $c = 1, 2, 3$ and Dirac spinor index $\alpha = 0, 1, 2, 3$ (we suppress these indices in the following) is given by

$$\mathcal{L}_{\text{free}} = \overline{q}(x)(i\gamma^\mu \partial_\mu - m_q)q(x), \tag{1.2}$$

with $\overline{q} = q^\dagger \gamma^0$ being the corresponding antiquark field.[2] The Dirac γ-matrices are defined such that they satisfy the anti-commutation relation $\{\gamma^\mu, \gamma^\nu\} = 2g^{\mu\nu}$, where $g^{\mu\nu} = g_{\mu\nu} = \text{diag}(1, -1, -1, -1)$ is the metric tensor in Minkowski space.

Postulating local gauge invariance, we demand that the Lagrangian (1.2), which is invariant under the global gauge transformation $q \mapsto \exp(i\alpha^a t^a)\, q$, be also symmetric under the *local* transformation

$$q(x) \mapsto V(x)\, q(x), \quad \text{where} \quad V(x) = \exp(i\alpha^a(x) t^a). \tag{1.3}$$

The previously constant coefficients α^a are now arbitrary functions of x, while the matrices t^a, $a = 1, \ldots 8$, are in both cases the Hermitian generators of $SU(3)$ (see also Appendix A.1).

In order to achieve local gauge symmetry of the free Lagrangian we need to replace the ordinary derivative in direction of the unit vector n,

$$n^\mu \partial_\mu q(x) = \lim_{a \to 0} \frac{1}{2a} \left[q(x + an) - q(x - an) \right], \tag{1.4}$$

by the *covariant derivative*

$$n^\mu D_\mu q(x) = \lim_{a \to 0} \frac{1}{2a} \left[U(x, x + an) q(x + an) - U(x, x - an) q(x - an) \right], \tag{1.5}$$

where we have introduced the unitary parallel transporter $U(y, x) \in SU(3)$ to account for the generally different gauge transformations at different space-time points; we set $U(y, y) = 1$. The comparator $U(y, x)$ itself transforms under a local gauge transformation as

$$U(y, x) \mapsto V(y) U(y, x) V^\dagger(x). \tag{1.6}$$

[2] For simplicity we consider only one quark flavor here. The generalization to N_f flavors is straightforward.

For small a it can be expanded in terms of the group generators t^a,

$$U(x+an,x) = 1 + igan^\mu A^a_\mu(x)t^a + O(a^2) \tag{1.7}$$

$$\equiv \mathcal{P}\exp\left[ig\int_P dx^\mu A_\mu(x)\right], \tag{1.8}$$

where the factor g (the bare coupling constant) has been extracted for convenience. The second expression holds for any path P connecting x and $x+an$ (for any finite a); $\mathcal{P}$ indicates path-ordering.

Inserting Eq. (1.7) into Eq. (1.5) we obtain for the covariant derivative

$$D_\mu = \partial_\mu - igA^a_\mu t^a. \tag{1.9}$$

The new fields $A_\mu(x) \equiv A^a_\mu(x)t^a$ (called *gauge fields* and identified with the gluons) transform like

$$A_\mu(x) \mapsto V(x)\left(A_\mu(x) + \frac{i}{g}\partial_\mu\right)V^\dagger(x); \tag{1.10}$$

their very existence is a consequence of the postulate of local gauge symmetry. As the covariant derivative transforms just like the quark field itself,

$$D_\mu \mapsto V(x)D_\mu, \tag{1.11}$$

any combination of the fields and their covariant derivatives that is invariant under a global gauge transformation is also locally invariant.

In order to complete the construction of a gauge symmetric Lagrangian we must find a kinetic energy term for the fields A_μ that is locally invariant and depends only on A_μ and its derivatives. Such a term can be obtained from the commutator of covariant derivatives,

$$[D_\mu, D_\nu] = -igF^a_{\mu\nu}t^a, \tag{1.12}$$

where the gluonic field tensor $F_{\mu\nu} \equiv F^a_{\mu\nu}t^a$ is explicitely given by

$$F_{\mu\nu} = \partial_\mu A_\nu - \partial_\nu A_\mu - ig\,[A_\mu, A_\nu] \tag{1.13}$$

$$= \partial_\mu A^a_\nu t^a - \partial_\nu A^a_\mu t^a + gf^{abc}A^b_\mu A^c_\nu\, t^a. \tag{1.14}$$

(See Appendix A.1 for the definition of the $SU(3)$ structure constants f^{abc}.) The transformation law for $F_{\mu\nu}$ is

$$F_{\mu\nu}(x) \mapsto V(x)F_{\mu\nu}(x)V^\dagger(x). \tag{1.15}$$

The non-vanishing gauge-field commutator $[A_\mu, A_\nu]$ in Eq. (1.13) reflects the fact that in contrast to the photon in QED the gluons interact with themselves, a fact that renders the theory mathematically considerably more complicated than QED.

From the infinitesimal forms of Eqns. (1.3), (1.10) and (1.15) one can show that any globally symmetric function of q, $F^a_{\mu\nu}$ and their covariant derivatives is also locally symmetric. However, the most general gauge-invariant Lagrangian for QCD with terms up to dimension 4 that is renormalizable and also invariant under parity transformation and time-reversal is (for one quark flavor) given by

$$\mathcal{L} = \overline{q}(i\gamma^\mu D_\mu - m_q)q - \frac{1}{4}(F^a_{\mu\nu})^2. \tag{1.16}$$

1.2 Functional Quantization

The construction of the classical QCD Lagrangian is only the first step in the process of relating the idea of non-Abelian gauge invariance to the real interactions of particle physics. In this section we introduce the Feynman *path integral*, an ingenious alternative to the "second quantization" of the classical fields. As it builds on the Lagrangian rather than the Hamiltonian it preserves explicitly all the symmetries of the theory. With regard to lattice gauge theories the functional integral formalism offers a particular advantage: appropriately defined it reveals the close analogy between quantum field theory and statistical mechanics, thus making the powerful techniques of the latter readily available for non-perturbative, *ab-initio* calculations in QCD.

In the path integral formalism, the fundamental quantity is the action $S = \int d^4x\ \mathcal{L}$, which for QCD is explicitly given by the space-time integral over the Lagrangian density (1.16),

$$S = S_{\mathrm{q}} + S_{\mathrm{g}} = \int d^4x\ \left[\overline{q}(i\gamma^\mu D_\mu - m_q)q - \frac{1}{4}(F^a_{\mu\nu})^2\right]. \tag{1.17}$$

The expectation value of a physical observable $\mathcal{O}$ is given by the functional integral

$$\langle\mathcal{O}\rangle = \frac{1}{Z}\int \mathcal{D}\overline{q}\,\mathcal{D}q\,\mathcal{D}A\ \mathcal{O}[\overline{q},q,A]\ e^{iS[\overline{q},q,A]}, \tag{1.18}$$

normalized by the partition function

$$Z = \int \mathcal{D}\overline{q}\,\mathcal{D}q\,\mathcal{D}A\ \ e^{iS[\overline{q},q,A]}. \tag{1.19}$$

The idea of integrating over all possible "paths" (contributing to a given outcome according to their relative "importance") goes back to the superposition principle in quantum mechanics, stating that if a process can take place in more than one way, its total amplitude is the coherent sum of the amplitudes for each way. A practical aspect facilitating actual (numerical) calculations is that the functional integral is an integral over ordinary functions, not operators. But there is a caveat, because in the case of anticommuting fermions even the classical fields in the functional integral must be replaced by *anticommuting* numbers (so-called Grassmann numbers). The Gaussian integration over the Grassmannian quark fields can then be carried out analytically, however, leading to the appearance of the fermionic *functional determinant*,

$$\int \mathcal{D}\overline{q}\,\mathcal{D}q\ \exp\left[i\int d^4x\ \overline{q}Mq\right] = \det M, \tag{1.20}$$

where we have set $M \equiv i\gamma^\mu D_\mu - m_q$. It can be shown that the functional determinant is, in fact, equivalent to the sum of vacuum Feynman diagrams.

In practice, an observable $\mathcal{O}$ is typically given in terms of time-ordered products of gauge and quark fields, the latter of which can be re-expressed in terms of quark propagators using Wick's theorem for the contraction of fields. As the quark propagator, $M[A]^{-1}$, does not explicitly depend on the quarks as dynamical fields, we can write for the expectation value of $\mathcal{O}$:

$$\langle\mathcal{O}\rangle = \frac{1}{Z}\int \mathcal{D}A\ \ \mathcal{O}[A]\,e^{iS[A]} \quad \text{with} \quad Z = \int \mathcal{D}A\ \ e^{iS[A]}, \tag{1.21}$$

where we have defined the effective action

$$S = \int d^4x\ \left[\log\det M - \frac{1}{4}(F^a_{\mu\nu})^2\right]. \tag{1.22}$$

In order to give the path integral a well-defined mathematical meaning we need to suitably regularize the measure, $\mathcal{D}A$, by discretizing space-time. Moreover, in order to make the exponential weight factor real we will continue the time variable to imaginary values in the next section.

1.3 Euclidean Space-Time

The *Wick rotation* in configuration space is defined by a rotation of the time coordinate in the complex plane,

$$t \equiv x^0 \;\mapsto\; \tau \equiv x_4 = -ix^0, \quad x^i \;\mapsto\; x_i = x^i \quad (i = 1, 2, 3), \tag{1.23}$$

yielding a Euclidean scalar product:

$$x_M^2 = (x^0)^2 - \mathbf{x}^2 \quad \mapsto \quad x_E^2 = x_1^2 + x_2^2 + x_3^2 + x_4^2 = -x_M^2. \tag{1.24}$$

The covariant and contravariant components of a Euclidean 4-vector are identical, $x^\mu = x_\mu$, and the metric tensor is just $\delta_{\mu\nu}$. The Euclidean γ-matrices are related to their counterparts in Minkowski space, γ_M^μ, by

$$\gamma_M^0 \;\mapsto\; \gamma_4 = \gamma_M^0, \quad \gamma_M^i \;\mapsto\; \gamma_i = i\gamma_M^i \quad (i = 1, 2, 3). \tag{1.25}$$

(See Appendix A.2 for our explicit choice of Euclidean γ-matrices.)

After Wick rotation, the Euclidean action S_E is real and given by

$$S \;\mapsto\; S_E = -iS, \tag{1.26}$$

or, more explicitly,

$$S_E = \int d^4x \; \left[\overline{q}(\gamma_\mu D_\mu + m_q)q + \frac{1}{4}(F_{\mu\nu}^a)^2 \right]. \tag{1.27}$$

The QCD partition function now takes the form

$$Z_E = \int \mathcal{D}\overline{q}\, \mathcal{D}q\, \mathcal{D}A \; e^{-S_E}, \tag{1.28}$$

which is analogous to a partition function in statistical mechanics with a real weight corresponding to the Boltzmann factor.[3] Unless otherwise stated we will exclusively work in Euclidean space-time from now on and therefore drop the subscript E.

In order to illustrate how one can extract physical observables like masses or decay constants from expectation values of operators, we consider the Euclidean two-point function

$$\langle 0|\mathrm{T}\left[\mathcal{O}_f(\mathbf{x}, \tau)\mathcal{O}_i(\mathbf{0}, 0)\right]|0\rangle, \tag{1.29}$$

where T is the time-ordered product, for $\tau > 0$. The creation operator $\mathcal{O}_i$ and the annihilation operator $\mathcal{O}_f$ are, typically, currents. The two-point correlation function gives the amplitude for the creation of a state with the quantum numbers of the *source* operator $\mathcal{O}_i$ out of the vacuum at space-time point 0, the propagation of this state to the space-time point x, and its annihilation by the *sink* operator $\mathcal{O}_f$. If we insert a complete set of energy eigenstates and integrate over

[3] The reality of the action is actually only guaranteed if the functional determinant of the Dirac operator is positive. We will come back to this point in Section 1.6.

the space-like coordinates we obtain a sum over all intermediate zero-momentum states with the right quantum numbers, exponentially damped in Euclidean time:

$$\langle 0|\int d^3x\ \mathcal{O}_f(\mathbf{x},\tau)\mathcal{O}_i(\mathbf{0},0)|0\rangle = \sum_n \frac{\langle 0\,|\mathcal{O}_f|\,n\rangle\langle n\,|\mathcal{O}_i|\,0\rangle}{2E_n} e^{-E_n\tau} \tag{1.30}$$

If there is a single-particle state $|1\rangle$ in the given channel, then the lowest energy, E_1, is equal to its mass M, and the asymptotic behavior of the correlation function for large times is

$$\langle 0|\int d^3x\ \mathcal{O}_f(\mathbf{x},\tau)\mathcal{O}_i(\mathbf{0},0)|0\rangle \overset{\tau\to\infty}{\longrightarrow} \frac{\langle 0\,|\mathcal{O}_f|\,1\rangle\langle 1\,|\mathcal{O}_i|\,0\rangle}{2M} e^{-M\tau}. \tag{1.31}$$

Using this relation the mass of a particle can be extracted from the rate of the exponential fall-off in Euclidean time of a suitable correlation function, because it can be shown that the mass M in Eq. (1.31) corresponds precisely to the pole mass of the particle's propagator in Minkowski space.

We note in passing that if a Euclidean correlation function obeys the Osterwalder-Schrader reflection positivity it can, in principle, be translated back to Minkowski space by analytic continuation[86].

1.4 Discretization

Having introduced the path integral and the QCD action in Euclidean space-time we are now prepared to finally define the lattice theory. To this end we need to discretize space-time and, accordingly, the fields, the action and the operators. We have seen in the previous section that there is a close analogy between Euclidean field theory and statistical mechanics, and how one can obtain physical information from the calculation of Euclidean correlation functions. Discretizing the continuum theory now serves two purposes: First, a discretized path integral is mathematically well-defined and allows for the numerical computation of exactly those correlation functions. Second, it provides a non-perturbative regularization scheme, with a hard ultraviolet (UV) momentum cut-off given by the inverse of the lattice spacing.

Let us, then, define a finite, isotropic hypercubic space-time grid with lattice spacing a and L sites in the spatial directions and T sites in temporal direction. This discretization introduces a UV cut-off because the allowed momenta on the lattice are discrete,

$$k_i = \pm\frac{2\pi n_i}{La}, \quad n_i = 0,\ldots,L/2, \tag{1.32}$$

so that the maximum momentum is π/a. At the opposite end of the momentum scale we have an infrared cut-off at $2\pi/La$, corresponding to the smallest non-zero momentum that can be realized on a finite lattice.

The quark field $q_c^\alpha(x)$ in Euclidean space-time with $SU(3)$ color index $c = 1,2,3$ and Dirac spinor index $\alpha = 1,2,3,4$ is simply defined at the lattice sites $x = an$, with $n_1, n_2, n_3 \in \{0,1,\ldots,L-1\}$ and $n_4 \in \{0,1,\ldots,T-1\}$. The construction of gauge fields on the lattice is, on the other hand, less straightforward. In Eq. (1.7) the continuum gauge fields $A_\mu(x)$ naturally appeared when we expanded the parallel transporter, $U(x+an,x)$, around the space-time point x for an infinitesimally small a in the direction of an arbitrary unit vector n. The parallel transporter was introduced in order to make the derivative gauge-covariant. Let us, then, consider the lattice

version of the covariant derivative, with the shortest distance between any two sites being the finite lattice spacing a. In fact, if we denote by $\hat{\mu}$ a unit vector along the grid-axis in the μ'th dimension ($\mu \in \{1,2,3,4\}$), then the lattice covariant derivative in the corresponding direction is given by the finite form of its continuum counterpart, Eq. (1.5), as

$$D_\mu q(x) = \frac{1}{2a}\left[U_\mu(x) q(x+a\hat{\mu}) - U_\mu^\dagger(x) q(x-a\hat{\mu})\right], \tag{1.33}$$

where we conveniently defined $U_\mu(x) \equiv U(x, x+a\hat{\mu})$ and used the fact that $U_\mu^\dagger(x) = U_{-\mu}(x)$. As they are associated with the connecting links between neighboring sites, the $SU(3)$-matrices $U_\mu(x)$ are called *gauge links*. In order to write down the path integral for lattice QCD we need a locally gauge invariant, discrete version of the QCD action. In the next section we will see that it is convenient to formulate the gauge part of this action directly in terms of the gauge links.

1.4.1 Gauge Action

There are only two gauge invariant objects one can construct on a lattice: First, so-called *strings*, path-ordered products of links that either have a fermion on one end and an antifermion at the other, or, in case of periodic boundary conditions, wind around the lattice. If a string goes around the lattice in temporal direction it is called a *Polyakov line* (or *loop*), otherwise it is a so-called *Wilson line*. We will come back to these objects in Chapter 4. The second class of gauge-invariant objects consists of closed *Wilson loops*. The simplest Wilson loop is the product of comparators around the smallest possible square on the lattice:

$$W_{\mu\nu}^{1\times 1}(x) = U_\mu(x) U_\nu(x+a\hat{\mu}) U_\mu^\dagger(x+a\hat{\nu}) U_\nu^\dagger(x). \tag{1.34}$$

This object is the so-called *plaquette variable*. For convenience we will use the term *plaquette* also for the real part of the mean diagonal entry of the $SU(3)$-matrix $W_{\mu\nu}^{1\times 1}(x)$, averaged over all smallest squares of a given lattice:

$$\square = \frac{1}{L^3 T} \sum_x \frac{1}{6} \sum_{\mu<\nu} \frac{1}{3} \operatorname{Re}\operatorname{Tr} W_{\mu\nu}^{1\times 1}(x). \tag{1.35}$$

A possible discrete representation of the gluonic part of the action in terms of the plaquette variable, originally due to Wilson, is given by

$$S_{\mathrm{g}} = \beta \sum_x \sum_{\mu<\nu} \left[1 - \frac{1}{3} \operatorname{Re}\operatorname{Tr} W_{\mu\nu}^{1\times 1}(x)\right] \tag{1.36}$$

$$= \frac{1}{4} \sum_x a^4 \; F_{\mu\nu}^a(x) F_{\mu\nu}^a(x) + O(a^6) \tag{1.37}$$

$$\to \frac{1}{4} \int d^4x \; (F_{\mu\nu}^a)^2. \tag{1.38}$$

This so-called *plaquette action*, Eq. (1.36), reproduces the gluonic continuum action, Eq. (1.38), in the limit $a \to 0$, with $O(a^2)$ corrections at finite a.

The parameter $\beta(a) = 6/g^2(a)$ in Eq. (1.36) is proportional to the inverse bare gauge coupling squared. In the context of numerical simulations it is an input parameter that (in a mass-independent renormalization scheme) implicitly sets the lattice spacing. The relation between the bare coupling g and the momentum scale, characterized by the inverse lattice spacing a^{-1}, is described by the renormalization group equation.

1.4.2 Fermionic Action

Just as in the gluonic case one would like to write down a discrete action for the quarks that preserves the fundamental properties of QCD not only in the continuum limit but also at finite lattice spacing. This refers in particular to gauge invariance and chiral symmetry. There is, however, a "no-go" theorem by Nielsen and Ninomiya proving quite generally that, on a lattice, there is no local, Hermitian quark action that is chirally symmetric and, at the same time, provides an unambiguous one-to-one correspondence between lattice and continuum fields [87]. This becomes manifest when one writes down the naive, straightforward discretization of the fermionic quark action, using the covariant derivative of Eq. (1.33):

$$a^4 \sum_x \overline{q}(x)(\gamma_\mu D_\mu + m_q)q(x) =$$

$$a^4 \sum_{x,\mu} \overline{q}(x)\gamma_\mu \frac{1}{2a}\left[U_\mu(x)q(x+a\hat{\mu}) - U_\mu^\dagger(x)q(x-a\hat{\mu})\right] + m_q\overline{q}(x)q(x). \tag{1.39}$$

While this fermion action is chirally invariant in the limit $m_q = 0$, it exhibits the problem of *doublers*: When we compare the inverse of the massless free fermion propagator (obtained by a Fourier transform of the massless naive lattice Dirac operator with all $U_\mu(x) \equiv 0$),

$$G^{-1}_{\text{naive}}(p) = \frac{i}{a}\sum_\mu \gamma_\mu \sin p_\mu a, \tag{1.40}$$

to that, in the continuum,

$$G^{-1}_{\text{cont}}(p) = i\gamma_\mu p_\mu, \tag{1.41}$$

then it is evident that on a 4-dimensional lattice the naive propagator has $2^4 = 16$ poles in a Brillouin zone instead of just one in the continuum.[4]

Faced with the choice of tolerating either spurious doubler states or explicit chiral symmetry breaking, Wilson opted for the latter by adding the following irrelevant, gauge-symmetric dimension 5 operator (in form of a second derivative, $-r/2\; a^5 \sum_x \overline{q}\,\Box\, q$) to Eq. (1.39):

$$-\frac{r}{2}a^5 \sum_{x,\mu} \overline{q}(x)\gamma_\mu \frac{1}{a^2}\left[U_\mu(x)q(x+a\hat{\mu}) - 2q(x) + U_\mu^\dagger(x)q(x-a\hat{\mu})\right]. \tag{1.42}$$

Due to this term the 15 doublers of the naive action aquire heavy masses proportional to $2r/a$ and decouple in the continuum limit. If we define the quark mass parameter κ (also called *hopping parameter*) as

$$\kappa = \frac{1}{2am_q + 8r} \tag{1.43}$$

and rescale the quark fields according to

$$a^{3/2}(am_q + 4r)^{1/2}\, q \quad \longmapsto \quad q, \tag{1.44}$$

we can write the resulting Wilson action for fermions as

$$S_{\text{q}} = \sum_{x,y} \overline{q}(x)M(x,y)q(y), \tag{1.45}$$

[4] One important consequence of the existence of doublers in the naive fermion action is the absence of the Adler-Bell-Jackiw anomaly: The axial current, which is conserved for gauge theories at the classical level but not conserved at the quantum level in the continuum theory, is conserved for naive lattice fermions.

where the quark interaction matrix $M(x, y)$ is explicitly given by

$$M(x,y) = \delta_{xy} - \kappa \sum_{\mu} \left[(r - \gamma_\mu) U_\mu(x) \delta_{x+a\hat{\mu},y} + (r + \gamma_\mu) U_\mu^\dagger(x - a\hat{\mu}) \delta_{x-a\hat{\mu},y} \right]. \tag{1.46}$$

The parameter r is usually set equal to one, because this choice results in a particularly convenient spin structure of $M(x, y)$.[5] Chiral symmetry is explicitly broken by the Wilson term (1.42) at finite a, but can be recovered in the continuum limit.

According to Eq. (1.43) the mass of a Wilson quark is given by

$$am_q = \frac{1}{2\kappa} - 4r = \frac{1}{2\kappa} - \frac{1}{2\kappa_c}; \tag{1.47}$$

it vanishes in the free case for $\kappa = \kappa_c \equiv 1/8r$. We define $am_q = 1/2\kappa - 1/2\kappa_c$ also for the interacting theory, so that κ_c becomes dependent on the lattice spacing a. As a consequence the quark mass receives not only multiplicative but also additive renormalizations.

In practice there are two ways to determine κ_c at any given a, which may differ in general by corrections of $O(a)$: First, assume the chiral relation $m_\pi^2 \propto m_q$, calculate m_π^2 as a function of $1/2\kappa$ and extrapolate to zero. Or, second, calculate the quark mass using the PCAC relation (based on the axial vector Ward identity) as a function of $1/2\kappa$ and again extrapolate to zero. In this work we will consider the PCAC quark mass in a slightly different context: as the PCAC relation is an operator identity it holds irrespective of the lattice volume and other parameters of the simulation, as long as the gauge coupling β and the bare quark mass parameter κ are kept constant. The PCAC quark mass thus depends on the lattice size only through $O(a)$ effects and may be used to assess the impact of these effects on a given simulation (see Section 4.5).

1.4.3 Improvement and Alternative Actions

The main drawbacks of the Wilson action are the explicit violation of the chiral symmetry of the original continuum action, and the relatively large discretization errors. These are only of order a^2 in the plaquette action, but the Wilson term in the quark action degrades this to $O(a)$. In recent years there have been many attempts to find better (so-called *improved*) discretizations of both the gauge and the quark part of the action with reduced errors, *i.e.* errors of higher order in the lattice spacing a. An early approach that goes by the name of *Symanzik's improvement program* is to remove lattice artefacts order by order in a by incorporating higher-dimensional, *irrelevant* terms (*i.e.* those that vanish in the continuum limit) in both the action and the considered operators [16]. A widely used example of an $O(a)$ improved quark action is the Sheikholeslami-Wohlert (*clover*) action [89]. For the involved coefficient c_{SW} mean-field improved perturbative values can be used [90], but non-perturbative values (determined with the help of the Schrödinger functional method [91]) are also available [92]. There are, furthermore, improved actions inspired by the renormalization group [93], ranging from the Iwasaki gauge action [94] over blocking transformations to (classically) perfect actions in the gauge and quark sectors [95]. A recent innovation is the use of "fat" links in fermionic actions which is based on the idea that discretization errors from a smooth cut-off are less severe than those associated with a hard lattice cut-off. The currently most popular variants of fat-link actions are the Asqtad ("a^2 tadpole") improved [96] and the HYP (hypercubic) actions [97].

[5] Recently, Frezzotti *et al.* have shown how this parameter can be used to improve the chiral behavior and the approach to the continuum limit of correlation functions [88].

There are, in principle, strong arguments for improvement: reducing discretization errors should, for instance, improve the scaling behavior of observables, *i.e.* one should be able to work on coarser lattices without losing accuracy.[6] One should also observe a better restoration of rotational and internal symmetries, like *e.g.* chiral invariance. But the downside of improved actions is that they are more complicated than the standard Wilson action, both theoretically and in practice. In particular, many of them are less local than the Wilson action and thus include not only nearest-neighbor interactions. This is reflected in an increased complexity of the numerical calculations and, consequently, longer simulation times.

Besides the Wilson quark action there is the so-called *staggered* (Kogut-Susskind) action [26], which is also widely used. In contrast to the Wilson action its discretization errors are only $O(a^2)$. More interesting, though, is the fact that it keeps a remnant chiral symmetry, albeit at the expense of a 4-fold increase in the number of flavors (so-called "tastes"), and spurious "taste"-changing interactions. An Asqtad improved version of a staggered fermion action is used by the HPQCD-MILC-UKQCD collaboration [27]. There are, however, unresolved fundamental concerns associated with this action, based on the need to take the fourth root of the quark determinant to convert the four-fold duplication of "tastes" into one quark flavor. This procedure may potentially lead to non-localities in the continuum limit which would spoil the claim that this action is a valid description of QCD [28].

Ultimately, with increasing computer power, approaches with exact lattice chirality that evade the Nielsen-Ninomiya theorem will become more and more attractive. The relevant developments in this direction are *domain-wall* fermions [29] and the *overlap* formulation [30] which satisfies the Ginsparg-Wilson relation [99]. However, dynamical simulations on sufficiently large and fine lattices using these actions are currently still prohibitively expensive.

Despite the above mentioned drawbacks, a very convenient feature of the Wilson fermion action is after all that the spin and flavor degrees of freedom are in one-to-one correspondence with continuum fermions. This renders the construction of interpolating field operators (see also Section 3.3) quite straightforward. The same holds true for the implementation of the Wilson action in computer programs that are to evaluate the path integral with Monte Carlo methods, as we will see in Section 1.6. We will therefore refer exclusively to the Wilson action throughout the rest of this work.

1.5 Group Integration

Before moving on to the issue of numerical lattice simulations we need to define the measure $\mathcal{D}U$ for the integration over the gauge degrees of freedom in the path integral. As the real and imaginary parts of the entries of the $SU(3)$ matrices $U_\mu(x)$ lie in the closed interval $[0,1]$, the $U_\mu(x)$ are elements of a compact Lie group. We can therefore take the integral over the gauge group to be the invariant *Haar measure* which, for any $V \in SU(3)$ and $f : SU(3) \to SU(3)$, is uniquely defined such that

$$\int dU\ f(U) = \int dU\ f(UV) = \int dU\ f(VU) \tag{1.48}$$

[6] Regarding the particular combination of $O(a)$ improved quark and standard plaquette action, some concern has been expressed recently that current $N_f = 2$ simulations at $a \approx 0.1\,\mathrm{fm}$ might be close to a phase transition, manifesting itself in unexpectedly large $O(a^2)$ cut-off effects [98].

and

$$\int dU \ = 1. \tag{1.49}$$

Property (1.48) guarantees gauge invariance, while (1.49) normalizes the measure.

For the path integral on the lattice we define

$$\mathcal{D}U = \prod_{x,\mu} dU_\mu(x), \tag{1.50}$$

where the product is over all lattice sites, x, and all positive coordinate directions, μ; it thus covers all the gauge links of the lattice.

A very convenient consequence of the fact that we integrate over a compact group is that we encounter no divergences. Hence, unless we want to do perturbative calculations, the path integral approach is well defined without fixing of a gauge. Another important point is that only gauge invariant quantities can have a non-zero expectation value. This is due to Elitzur's theorem [100], stating that a local invariance in a Euclidean gauge theory with a positive Euclidean weight in the path integral cannot be broken spontaneously.[7]

1.6 Lattice Simulations

The goal of a typical lattice simulation is the numerical computation of the expectation value of an operator $\mathcal{O}$ that is, in general, a correlation function involving gluonic fields and quark bilinears (see Eq. (1.29)). The operators that are relevant for this work will be specified in detail in Section 3.3. We assume that, after Wick contraction of the fermion fields, $\mathcal{O}$ depends on the quarks only through the fermion matrix $M[U]$. Then, having integrated out the quark degrees of freedom, the expectation value of $\mathcal{O}[U]$ is given by the purely bosonic path integral

$$\langle \mathcal{O} \rangle = \frac{1}{Z} \int \mathcal{D}U \ \mathcal{O}[U] \det M[U] \ e^{-S_{\mathrm{g}}[U]}, \tag{1.51}$$

with the partition function

$$Z = \int \mathcal{D}U \ \det M[U] \ e^{-S_{\mathrm{g}}[U]}. \tag{1.52}$$

The gauge invariant measure $\mathcal{D}U$ was defined in the previous section; the Wilson Dirac matrix M and the gauge action S_{g} were given in Eqns. (1.46) and (1.36), respectively. As we work in Euclidean space-time, the exponential $\exp(-S_{\mathrm{g}})$ is real and positive and can thus act as a statistical weight. Because of the "γ_5-Hermiticity" $M = \gamma_5 M^\dagger \gamma_5$ the determinant $\det M$ is also real, but it is not in general positive. If we consider two mass-degenerate flavors of quarks, however, we have $(\det M)^2 \geq 0$, and the expression

$$(\det M)^2 \exp(-S_{\mathrm{g}}) = \exp(\log(\det M)^2 - S_{\mathrm{g}}) \equiv \exp(-S_{\mathrm{eff}}) \tag{1.53}$$

can be considered altogether as a weight function, analogous to the Boltzmann factor in a statistical mechanics system.[8] Computing the path integral then amounts to generating *importance-sampled* gauge field configurations $\{[U_i], i = 1, \ldots, N_{\mathrm{conf}}\}$ according to the probability distribution

$$P[U] = Z^{-1} e^{-S_{\mathrm{eff}}[U]} \tag{1.54}$$

[7] See Ref. [101] for a recent re-examination of Elitzur's theorem.

[8] Physically we interpret the two mass-degenerate quark flavors as exactly isospin symmetric u and d quarks. The isospin symmetric mass is defined as $m_q = (m_u + m_d)/2$.

with

$$Z = \int \mathcal{D}U \; e^{-S_{\text{eff}}[U]}, \tag{1.55}$$

and calculating the expectation value of $\mathcal{O}$ by simply averaging over the ensemble:

$$\langle \mathcal{O} \rangle \approx \frac{1}{N_{\text{conf}}} \sum_{n=1}^{N_{\text{conf}}} \mathcal{O}[U_n]. \tag{1.56}$$

1.6.1 The Hybrid Monte Carlo Algorithm

There are a number of Monte-Carlo based algorithms that can be used to generate samples of gauge field configurations. For simulations with dynamical fermions, the most widely and in this work exclusively used is the Hybrid Monte Carlo (HMC) algorithm [20], a combination of the Metropolis algorithm with heatbath and classical molecular dynamics methods. In contrast to a local updating algorithm the HMC algorithm uses conjugate momenta and a Hamiltonian to generate a globally updated trial configuration which then undergoes a Metropolis accept-reject decision.

In every lattice simulation with fermions, the computation of the determinant in Eq. (1.53) represents the main challenge, as it is a highly non-local object and represents as such a major obstacle to any effective implementation on a parallel computer. For this reason the fermionic determinant is often simply set to a constant, which in physical terms corresponds to giving the fermions an infinite mass, so that vacuum polarization effects from virtual quark-antiquark pairs are fully suppressed. It must be stressed that, being an essentially uncontrolled simplification, this so-called *quenched approximation* is almost exclusively motivated by the requirement of computational expediency. If possible one will always prefer a full lattice QCD simulation with *dynamical* quarks, *i.e.* with the fermionic determinant taken into account.

A practical tool for this purpose is the HMC algorithm. We consider it here for two flavors of dynamical quarks with equal mass, in which case the fermion determinant can be written as

$$(\det M)^2 = \det M^\dagger M = \int \mathcal{D}\phi^\dagger \mathcal{D}\phi \; e^{-S_{\text{pf}}}, \tag{1.57}$$

where S_{pf} is given by

$$S_{\text{pf}} = \phi^\dagger (M^\dagger M)^{-1} \phi. \tag{1.58}$$

$\phi^\dagger$ and ϕ are bosonic fields with exactly the same number of degrees of freedom as the original fermion fields; they are therefore called *pseudo-fermions*. One arrives thus at a purely bosonic, effective lattice representation of the QCD action:

$$S_{\text{eff}}[U, \phi^\dagger, \phi] = S_{\text{g}}[U] + S_{\text{pf}}[U, \phi^\dagger, \phi]. \tag{1.59}$$

The expectation value of $\mathcal{O}$ is now given by

$$\langle \mathcal{O} \rangle = \frac{1}{Z} \int \mathcal{D}\phi^\dagger \mathcal{D}\phi \mathcal{D}U \; \mathcal{O}[U] \; e^{-S_{\text{eff}}[U,\phi^\dagger,\phi]}, \tag{1.60}$$

with the partition function

$$Z = \int \mathcal{D}\phi^\dagger \mathcal{D}\phi \mathcal{D}U \; e^{-S_{\text{eff}}[U,\phi^\dagger,\phi]}. \tag{1.61}$$

Introducing a momentum field Π canonically conjugate to the gauge field U, we define a conservative dynamical system with the Hamiltonian

$$H[\Pi, U, \phi^\dagger, \phi] = T[\Pi] + S_{\rm g}[U] + S_{\rm pf}[\phi^\dagger, \phi, U], \tag{1.62}$$

where the kinetic term is

$$T = \frac{1}{2}\sum_{x,\mu} \mathrm{Tr}\, \Pi_\mu^2(x). \tag{1.63}$$

The canonical momenta $\Pi_\mu(x)$ are elements of the Lie algebra of $SU(3)$ and can thus be written as linear combinations of the eight Gell-Mann matrices λ^a (see Appendix A.1). Only the gauge field will be updated by a dynamical process, while the pseudofermion fields $\phi^\dagger, \phi$ are randomly generated from a heatbath at the beginning of each "trajectory" and then kept constant as a static "background field" until the new gauge configuration has been either accepted or rejected. We therefore do not need to introduce conjugate momenta also for the pseudofermion fields.

We note that the expectation value

$$\langle \mathcal{O} \rangle = \frac{1}{Z}\int \mathcal{D}\phi^\dagger \mathcal{D}\phi \mathcal{D}U\ \mathcal{O}[U]\ e^{-H[\Pi, U, \phi^\dagger, \phi]} \tag{1.64}$$

with the partition function

$$Z = \int \mathcal{D}\phi^\dagger \mathcal{D}\phi \mathcal{D}U\ e^{-H[\Pi, U, \phi^\dagger, \phi]} \tag{1.65}$$

is equivalent to Eq. (1.60) because the constant from the Gaussian integration over the canonical momenta is canceled by the normalization.

Hamilton's equations, $\dot{U}_\mu = \partial H/\partial \Pi_\mu$ and $\dot{\Pi}_\mu = -\partial H/\partial U_\mu$, imply that $U_\mu(x)$ and $\Pi_\mu(x)$ satisfy the equations of motion

$$\dot{U}_\mu = i\Pi_\mu U_\mu, \tag{1.66a}$$

$$\dot{\Pi}_\mu = -iF_\mu \tag{1.66b}$$

with respect to a (fictitious) molecular dynamics time t. In Eq. (1.66b), $F_\mu(x)$ is the force on the momentum field, the form of which is found by imposing the constraint of conservation of energy, $\dot{H} = 0$, on the dynamical system; it reads

$$F_\mu(x) = \Big(U_\mu(x)\hat{F}_\mu(x) - \text{h.c.}\Big) - \frac{1}{3}\,\mathrm{Tr}\left[\Big(U_\mu(x)\hat{F}_\mu(x) - \text{h.c.}\Big)\right] \tag{1.67}$$

with

$$\hat{F}_\mu(x) = -\frac{\beta}{6}G_\mu(x) + \kappa W_\mu(x), \tag{1.68}$$

where

$$\begin{aligned} G_\mu(x) = \sum_{\nu\neq\mu} & U_\nu(x + a\hat{\mu})U_\mu^\dagger(x + a\hat{\nu})U_\nu^\dagger(x) \\ & + U_\nu^\dagger(x + a\hat{\mu} - a\hat{\nu})U_\mu^\dagger(x - a\hat{\nu})U_\nu(x - a\hat{\nu}) \end{aligned} \tag{1.69}$$

stands for the sum over the upper and lower *staples* at each lattice site x. Defining the fields X and Y as

$$X = \left(M^\dagger M\right)^{-1}\phi, \tag{1.70a}$$

$$Y = \left(M^\dagger\right)^{-1}\phi, \tag{1.70b}$$

the part of the force (1.67), (1.68) involving the fermionic matrix M, $W_\mu(x)$, can be written as

$$W_\mu(x) = \mathrm{Tr}\,\left[(1+\gamma_\mu)Y(x+a\hat{\mu})X^\dagger(x) + (1-\gamma_\mu)X(x+a\hat{\mu})Y^\dagger(x)\right], \tag{1.71}$$

where the trace is over the spin indices.

The Hybrid Monte Carlo algorithm now proceeds by the following steps:

1. **Heatbath:** Given an initial gauge configuration U at time $t = t_0$, generate the pseudofermion field ϕ according to the Gaussian distribution

$$P[\phi^\dagger, \phi, U] \propto e^{-S_{\mathrm{pf}}[\phi^\dagger,\phi,U]}. \tag{1.72}$$

   This can be done by generating a random spin-color vector ξ with a Gaussian distribution of zero mean and unit variance, and then putting $\phi = M^\dagger\xi$.

   Similarly, generate the momentum field Π randomly with the Gaussian distribution

$$P[\Pi] \propto e^{-T[\Pi]}. \tag{1.73}$$

2. **Dynamical evolution:** Use a symmetric symplectic numerical integration scheme (*e.g.* the *leapfrog* scheme) to integrate the equations of motion (1.66). Applying the scheme N_{MD} times with a step size δt we find trial updates Π', U' of the fields at a time $N_{\mathrm{MD}}\delta t$ later. Symmetric symplectic integration schemes are reversible and phase-space area preserving and thus ensure that the algorithm satisfies the detailed balance condition. The time evolution of the fields over some length of time is called the *trajectory*, and $N_{\mathrm{MD}}\delta t$ is the *trajectory length*.

3. **Metropolis step:** Accept the new gauge configuration with the probability

$$P_A([\Pi', U'] \leftarrow [\Pi, U]) = \min\left(1, e^{-\Delta H}\right), \tag{1.74}$$

   where

$$\Delta H = H[\Pi', U'] - H[\Pi, U]. \tag{1.75}$$

   Otherwise reject it and restore the original configuration of $t = t_0$. This step renders the numerical algorithm exact in the sense that it defines a Markov process with the distribution $Z^{-1}e^{-H}$ as its fixed point. Since Π and U are decoupled in H we obtain the desired distribution of U.

The computational challenge of a full QCD simulation with the HMC algorithm lies in the calculation of the fermionic force (1.71) in each step of the dynamical evolution. In order to obtain a single new trial configuration, the integration of the equations of motion (1.66) typically requires $N_{\mathrm{MD}} = O(100)$ steps in each of which the linear systems (1.70) must be solved. Also, the

calculation of $S_{\mathrm{pf}}[\phi^\dagger, \phi, U]$ in the Hamiltonian requires a matrix inversion. To give an example, for a typical lattice with $L^3 \times T = 16^3 \times 32$ sites the Wilson Dirac operator M is a complex matrix of dimension $1\,572\,864 \times 1\,572\,864$. In any case the rank of M is too large to consider direct solvers for its inversion, but as it couples only nearest-neighbor sites we can exploit its sparseness to use iterative Krylov subspace methods like the conjugate gradient (CG) or the stabilized bi-conjugate gradient (BiCGStab) algorithm [75]. The convergence behavior of an optimal Krylov subspace solver is solely governed by the condition number of the matrix, which is defined as the ratio of the largest to the smallest eigenvalue: the larger this number, the harder is the matrix inversion. Preconditioning the matrix in general reduces the condition number and can therefore considerably speed up the solver; in this work we use the locally-lexicographic SSOR method [76]. The computational cost of producing a given number of statistically independent gauge configurations grows significantly with decreasing quark mass and increasing lattice volume: Assuming the temporal lattice extent T to be twice as large as the spatial extent L, the cost of a $N_f = 2$ simulation roughly scales like $L^5 M_{\mathrm{PS}}^{-z}$, where the pseudoscalar mass M_{PS} characterizes the quark mass and $z = 2.8(2)..4.3(2)$ [21].

1.6.2 Errors in Lattice Results

Expectation values obtained from numerical lattice QCD simulations are subject to both statistical and systematic errors. Of course, this is in the very nature of a stochastic evaluation of a finite and discrete approximation to an infinite continuous system. In order to obtain reliable lattice QCD results that can be compared with "real" experimental data we must have control over the various error sources, the most important ones of which we will list in the following.

Statistical Errors

The Monte Carlo method we use to compute the high-dimensional path integral over the lattice gauge fields involves statistical sampling. The results, therefore, have statistical errors. However, the naive assumption that the statistical errors should decrease as $1/\sqrt{N}$, where N is the size of the sample, holds only for statistically independent measurements, whereas in a typical lattice simulation the configurations generated by the updating process are correlated. In a reliable error analysis this correlation has to be taken into account. A suitable error estimator serving this purpose is, for instance, the blocked jackknife method which we will discuss in more detail in Section 3.8.

In practice it is convenient to know, at least approximately, the autocorrelation times of the observables one is interested in, because it helps saving computer time when the cost intensive calculation of the quark propagator is done only for a subsample. Choosing a subsample essentially amounts to choosing a certain separation in Monte Carlo time between successive elements of the subsample, which is in general a trade-off between high statistics and available computing resources, with the estimated autocorrelation times taken into account.

Finite Volume

In any numerical lattice simulation, the lattice volume is necessarily finite and restricted by the available computer power. In order to control potential finite-size effects on measurable quantities such as masses one either has to ensure that they are negligible by making the lattice large enough, or eliminate them by a suitable extrapolation to the infinite volume. In either

case one has to compare results from different lattice volumes, with all other parameters held fixed. Finite volume effects are the main subject of this work, and we will discuss them in detail in the next chapters.[9]

In a lattice simulation, the physical box-size can be enlarged either by increasing the number of spatial lattice sites at fixed lattice spacing a, or by increasing a for fixed L. This, however, also increases the associated discretization errors.

Finite Lattice Spacing

In a mass-independent renormalization scheme the lattice spacing a in a simulation is implicitly determined by the choice of the gauge coupling parameter β. It can be determined in physical units by matching the lattice result for a chosen observable (the Sommer parameter r_0 [74] is the most popular choice) with the corresponding experimental value. At finite values of a the size of the cut-off effects depends on the order in a of the leading corrections to the chosen lattice action; for the Wilson action it is $O(a)$. In order to obtain continuum results one has to perform simulations at a number of values for a and extrapolate the results to $a = 0$. One generally expects discretization errors to be smaller for low-energy quantities like Goldstone boson masses or decay constants than for the nucleon, for instance, which is expected to be stronger affected by a low cut-off.

Unphysically Large Quark Masses

In summary, the previous two requirements of sufficiently large physical volume La and small lattice spacing a read

$$a \ll 1/m_{\mathrm{PS}} \ll La, \tag{1.76}$$

where $1/m_{\mathrm{PS}}$ is the correlation length of the pseudoscalar meson (the lightest hadronic state). In view of this relation the physical u and d quark masses are clearly too small to simulate them with currently feasible lattice volumes. Moreover, the condition number of the Dirac matrix grows with decreasing quark mass. In terms of the Wilson quark mass parameter κ a decreasing quark mass is equivalent to κ approaching κ_c, the critical value where the quark mass vanishes (see Eq. (1.47)). However, for a given set of simulation parameters (β, κ) the critical hopping parameter κ_c is uniquely defined only as a statistical average over the whole gauge field ensemble, while its value on individual configurations fluctuates. From this, another complication arises: If the fluctuating value of κ_c gets close to κ, the quark matrix may become singular. This problem becomes increasingly severe with decreasing quark mass, β and L.[10]

The standard way out of this dilemma is to choose the simulated quark mass sufficiently large and extrapolate the results to the regime of physical quark masses using low-order polynomials or functional forms derived from chiral perturbation theory (ChPT). However, statistical and

[9] Another consequence of the finite lattice volume is a finite momentum resolution. As can be seen from Eq. (1.32), the smallest non-zero momentum on the lattice is $2\pi/La$. While this is not problematic for the determination of ground state masses at zero momentum, one needs a rather fine resolution for the investigation of dispersion relations or decays.

[10] The problem of fluctuating zero modes (leading to so-called "exceptional configurations") is most severe in the context of quenched simulations. In full lattice QCD zero modes are suppressed by the functional determinant in the path integral. (However, they may still occur in the stochastic updating process, where they lead to an exceptionally low acceptance rate.) A recent development that prevents the appearance of exceptional configurations for $N_f = 2$ is "twisted mass" QCD [102, 103].

systematic uncertainties in lattice results often make it difficult to apply the full ChPT formulae or to assess the size of various higher order chiral corrections. Some recent developments seeking to improve on this situation are partially quenched ChPT (PQChPT) [44, 45, 46] or ChPT with Wilson-type fermions (WChPT) [47, 48, 49, 50]. These are effective theories that incorporate the effects of different valence and sea quark masses, and also account for a finite lattice spacing. Reports on promising numerical results with these schemes have been published recently by the qq+q [18] and the CP-PACS [19] collaborations.

Chapter 2

Volume Dependence of the Light Hadron Masses

In this chapter we review the main theoretical and numerical findings published to date about the nature of finite-size effects in light hadron masses. Although as a source of systematic error the finite volume has in principle always been an important issue in lattice QCD, there have been surprisingly few systematic investigations up to now into the lattice size dependence of simulated hadron masses. Usually one seeks to avoid finite-size effects altogether by working on sufficiently large lattices (where, as a rule of thumb, a lattice size of five times the Compton wave length of the pion, $M_\pi L \gtrsim 5$, is commonly considered "large").

Perhaps the most important theoretical contribution to the subject dates back to the year 1986 when M. Lüscher proved, for stable particles in largely arbitrary quantum field theories, a formula predicting an exponential suppression of the finite-size mass shift towards large volumes [53]. With input from an effective theory like chiral perturbation theory Lüscher's formula can be used to describe the asymptotic finite-size mass shifts for stable light hadrons like the pion or the nucleon [54]. The first systematic numerical investigations of finite volume effects in full lattice QCD were carried out by Fukugita *et al.* in 1992 [56]. Observing, rather unexpectedly, a power-law behavior of their data for the pion, rho and nucleon masses, they also made suggestions as to the underlying mechanism. Lüscher's formula, on the one hand, deals with asymptotically large lattice volumes where finite-size effects arise from a squeezing of the virtual pion cloud that surrounds the hadron due to vacuum polarization. In a box with periodic boundary conditions these pions can travel "around the world" and interact with each other. Thus, the finite-size mass shift is related to an (infinite volume) elastic forward scattering amplitude. In contrast, the power-law behavior of the data as observed by Fukugita *et al.* is due to a distortion of the hadron wave-function itself, as it is expected for rather small box volumes.

Recently, alongside with progress that has been made in relating effective field theory to the lattice, finite-size effects have attracted more attention again. A particularly promising new result for the volume dependence of the nucleon mass has emerged from (baryon) chiral perturbation theory [66]. We will show later in this work that it compares well with our data, over a wide range of lattice sizes.

We will now introduce the theoretical aspects of the different approaches in turn. Numerical details and comparisons with our findings are deferred to Chapter 4.

2.1 Lüscher's Formula

Lüscher's formula is a universal quantum field theoretic formula for the shift in the mass of a stable particle enclosed in a box with periodic boundary conditions. For a field theory in finite volume the spectrum of the Hamiltonian (or the transfer matrix on the lattice) is discrete, and energies associated with zero momentum eigenstates are interpreted as masses of single stable particles at rest. In a large volume these masses are close, but not equal, to the rest masses of the particles in infinite volume. Lüscher's formula states that for asymptotically large volumes the finite-size mass-shift vanishes *exponentially* with increasing box size at a rate that depends on the particle under consideration and on the spectrum of light particles in the theory.

The physical origin of the mass shift of a pointlike stable particle is that such a particle polarizes the vacuum around it, so that it is surrounded by a cloud of virtual particles. The diameter of this cloud is roughly of the order of the Compton wave length, λ, of the lightest particle in the theory. When enclosed in a box, the mass of the particle starts to deviate from its value in infinite volume as soon as the box size approaches λ. In this physical picture the size dependence of the particle's mass arises from an exchange of virtual particles "around the world". Using abstract graph theory and complex contour integration, Lüscher calculates the asymptotic volume-dependence of the self-energy diagrams contributing to the particle's full propagator, and hence of the pole mass of the propagator, in finite volume and to all orders in perturbation theory. The resulting formula relates the shift in the pole mass to the amplitude for elastic forward scattering of the particle with the lightest particle(s) in the quantum field theory under consideration. The detailed proof of this relation is given in Ref. [53].

What we are interested in here is the application of Lüscher's formula to hadronic states in lattice QCD.[1] Let us therefore consider a stable hadron H (where H stands either for the pion, π, or the nucleon, N) on a lattice with lattice spacing a, spatial volume $(La)^3$ and sufficiently large (Euclidian) time-extent Ta (ideally, $T \to \infty$). We assume periodic boundary conditions in the spatial directions. For the rest of this chapter we set the lattice spacing a equal to one, so that the mass m_H of H, which is defined through the leading exponential decay of an appropriate Euclidean 2-point function at large times, is dimensionless. Keeping both the bare gauge coupling g and the quark mass fixed, the hadron mass m_H depends on the number of lattice sites in spatial direction, L, in a particular way. If we define the infinite-volume mass at fixed lattice spacing and quark mass as

$$m_H = \lim_{L\to\infty} m_H(L), \tag{2.1}$$

then, for large L, $m_H(L)$ is supposed to become a universal function of $m_\pi L$ in the finite-volume continuum limit, which is obtained by taking $g \to 0$ and simultaneously $L \to \infty$, while keeping $m_\pi L$ fixed. However, since finite-size effects probe the system at large distances $L \gg 1$ and are

[1] Remarks: 1. The proof in Ref. [53] is given to all orders in perturbation theory, but the result itself is believed to be true beyond perturbation theory, as it is independent of the precise form of the Lagrangian of the theory and refers only to the physical masses and scattering amplitudes of the particles. In particular it is independent of a possible fixed UV cut-off, so that it should also hold for a lattice theory. In the original proof of the formula it is assumed that all the involved fields are massive. Although this is not the case for QCD, where perturbation theory in the gauge coupling constant involves massless fields, one can always describe the low energy properties of QCD by effective Lagrangians (like the chiral Lagrangian), which are of exactly the type that the Feynman diagram technique used in the proof can be applied to. 2. Although hadrons can be seen as bound states of valence quarks, due to confinement the leading finite size effect on hadron masses originates from the same mechanism as for pointlike particles, namely to the squeezing of the virtual pion cloud. 3. We exclusively refer to *full* lattice QCD here. As the formula describes vacuum polarization effects, it does *not* apply to the quenched approximation.

thus insensitive to short-distance effects, this function is expected to be largely independent of the form and magnitude of a possible ultraviolet cut-off. In particular it is then expected to hold also for finite lattice spacings.

Lüscher's formula relates the finite volume mass shift,

$$\Delta m_H(L) \equiv m_H(L) - m_H, \tag{2.2}$$

to the (infinite volume) elastic forward scattering amplitude $F_{\pi H}$. Let us consider the elastic scattering process

$$\pi^a(p)H^b(q) \to \pi^{a'}(p')H^{b'}(q'), \tag{2.3}$$

where the pion has 4-momentum p and isospin a and the particle H carries 4-momentum q and quantum numbers b (isospin, spin). The primed quantities refer to the corresponding outcoming states. All ingoing and outcoming particles are on their mass shell, respectively, so that the energy components of the 4-momenta (in Minkowski space) are given by $p^0 = E_{\mathbf{p}}$, $p'^0 = E_{\mathbf{p}'}$ *etc.*, with

$$E_{\mathbf{p}} = \sqrt{m^2 + \mathbf{p}^2}, \tag{2.4}$$

where m is the mass of the particle and $\mathbf{p}$ its 3-momentum. General one-particle states $|H^a(p)\rangle$ on their mass-shell are normalized such that

$$\langle H^{a'}(p')|H^a(p)\rangle = 2E_{\mathbf{p}}\,(2\pi)^3\,\delta^{(3)}(\mathbf{p}' - \mathbf{p})\,\delta^{a'a}. \tag{2.5}$$

The S-matrix for elastic πH scattering is given by

$${}_{\text{out}}\langle\pi^{a'}(p')H^{b'}(q')|\pi^a(p)H^b(q)\rangle_{\text{in}} \equiv \langle\pi^{a'}(p')H^{b'}(q')\,|S|\,\pi^a(p)H^b(q)\rangle, \tag{2.6}$$

and as usual we define the T-matrix (the part that accounts for interactions in the scattering event) by $S = \mathbf{1} + iT$. Matrix elements of T can be written in terms of the invariant matrix element $\mathcal{M}$ as

$$\begin{aligned}&\langle\pi^{a'}(p')H^{b'}(q')\,|iT|\,\pi^a(p)H^b(q)\rangle = \\ &\qquad (2\pi)^4\,\delta^{(4)}(p' + q' - p - q)\,i\mathcal{M}\big(\pi^a(p)H^b(q) \to \pi^{a'}(p')H^{b'}(q')\big).\end{aligned} \tag{2.7}$$

We are interested in the forward scattering amplitude

$$F_{\pi H} = \sum_a \mathcal{M}\big(\pi^a(p)H^b(q) \to \pi^a(p)H^b(q)\big), \tag{2.8}$$

which in all cases considered here is a Lorentz scalar depending only on the crossing variable

$$\nu = \frac{pq}{m_H}. \tag{2.9}$$

2.1.1 Pion

For the pion ($H = \pi$) the mass shift $\Delta m_\pi(L)$ is given in terms of the $\pi\pi$ forward scattering amplitude $F_{\pi\pi}$ by

$$m_\pi(L) - m_\pi = -\frac{3}{16\pi^2 m_\pi L}\int_{-\infty}^{\infty} dy\; e^{-\sqrt{m_\pi^2+y^2}L}F_{\pi\pi}(iy) + O(e^{-\bar{m}L}). \tag{2.10}$$

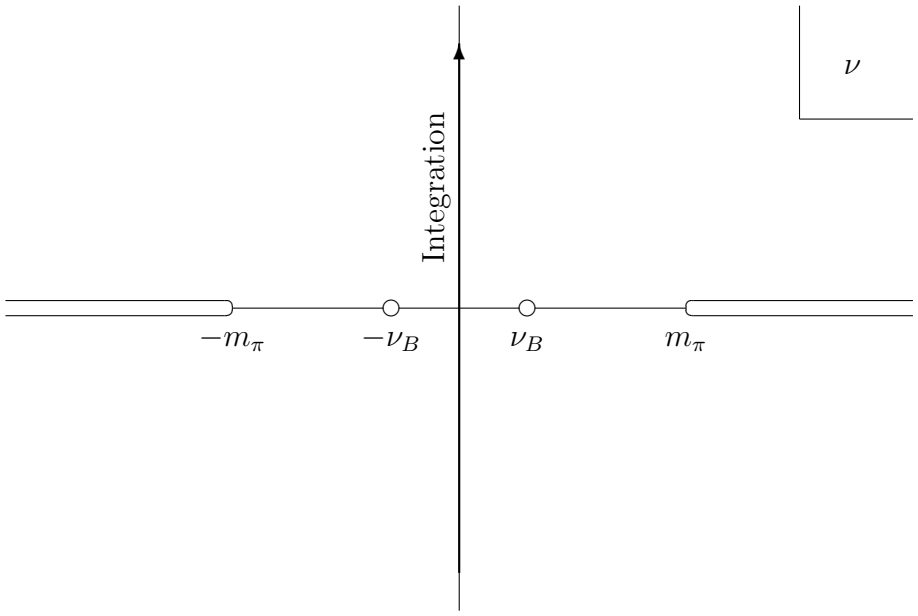

Figure 2.1: Integration contour in the complex ν-plane. The poles at $\nu = \pm\nu_B$ are due to 1-particle exchange reactions which do occur for the nucleon, but not for the pion.

Eq. (2.10) is Lüscher's formula for the asymptotic finite-size effect of the pion. Because of $\bar{m} \geq \sqrt{3/2}\, m_\pi$, the error term is exponentially suppressed compared to the first term. Due to the negative intrinsic parity of the pion and parity conservation in QCD there is no 3-pion vertex, so that the term referring to a 3-particle coupling in the original formula of Ref. [53] is absent. Hence the scattering amplitude $F_{\pi\pi}(\nu)$, which is analytic in the complex ν-plane with branch cuts between $-\infty$ and $-m_\pi$ and between m_π and ∞, has no isolated singularities from 1-particle exchange reactions. $F_{\pi\pi}(\nu)$ is integrated over along the imaginary axis in the ν-plane (see Fig. 2.1).

The crossing variable ν and the invariant matrix element $\mathcal{M}$ for elastic $\pi\pi$ scattering can be written in terms of the Mandelstam variables

$$s = (p+q)^2, \quad t = (q'-q)^2, \quad u = (q'-p)^2 \tag{2.11}$$

(satisfying $s + t + u = 4m_\pi^2$) and the isospin-invariant amplitude $A(s,t,u)$ as

$$\nu = \frac{s}{2m_\pi} - m_\pi \tag{2.12}$$

and

$$\mathcal{M}\big(\pi^a(p)\pi^b(q) \to \pi^{a'}(p')\pi^{b'}(q')\big) =$$

$$\delta_{ab}\delta_{a'b'}A(s,t,u) + \delta_{aa'}\delta_{bb'}A(t,u,s) + \delta_{ab'}\delta_{ba'}A(u,s,t), \tag{2.13}$$

respectively. Eq. (2.13) is a consequence of crossing symmetry, isospin conservation and Bose statistics. Following Eq. (2.8) we sum over isospin to obtain the following expression for the forward amplitude:

$$F_{\pi\pi}(\nu) = A\big(s(\nu), 0, u(\nu)\big) + 3A\big(0, u(\nu), s(\nu)\big) + A\big(u(\nu), s(\nu), 0\big) \tag{2.14}$$

where

$$s(\nu) = 2m_\pi^2 + 2m_\pi\nu, \quad t \equiv 0, \quad u(\nu) = 2m_\pi^2 - 2m_\pi\nu. \tag{2.15}$$

The scattering amplitude $A(s,t,u)$ is known consistently from current algebra calculations [104] and chiral perturbation theory [43]; at leading order ChPT it reads

$$A(s,t,u) = \frac{s - m_\pi^2}{f_\pi^2}, \tag{2.16}$$

where f_π is the pion decay constant. Substituting this result into Eq. (2.14) and using (2.15) we obtain the constant value

$$F_{\pi\pi} \equiv -\frac{m_\pi^2}{f_\pi^2}. \tag{2.17}$$

For this simple case the integral in Eq. (2.10) can be solved analytically, and we arrive at the relative pion finite size mass shift

$$\left.\frac{m_\pi(L) - m_\pi}{m_\pi}\right|_{\rm LO} = \frac{3}{8\pi^2}\frac{m_\pi^2}{f_\pi^2}\frac{K_1(m_\pi L)}{m_\pi L} \tag{2.18}$$

$$\simeq \frac{3}{4(2\pi)^{3/2}}\frac{m_\pi^2}{f_\pi^2}\frac{e^{-m_\pi L}}{(m_\pi L)^{3/2}}, \tag{2.19}$$

where K_1 is a modified Bessel function, and the second expression follows from its asymptotic behavior, $K_1(x) \simeq e^{-x}/\sqrt{x}$, for large x.

In Chapter 4 we will investigate the importance of higher order chiral corrections to the amplitude A and find that in the parameter region where finite size corrections to the pion mass are significant, the leading order result (2.16) is not sufficient to account for the full effect.

2.1.2 Nucleon

In case of the nucleon ($H = N$) the crossing variable (2.9) is defined as $\nu = pq/m_N$. The forward amplitude $F_{\pi N}(\nu)$ has isolated singularities at $\nu = \pm\nu_B$, where

$$\nu_B = \frac{m_\pi^2}{2m_N}, \tag{2.20}$$

with the residue

$$\lim_{\nu\to\pm\nu_B}(\nu^2 - \nu_B^2)F_{\pi N}(\nu) = -6g_{\pi N}^2\nu_B^2. \tag{2.21}$$

The poles come from one-nucleon exchange diagrams, because for $\nu = \pm\nu_B$ the intermediate 4-momenta in these diagrams are just on the nucleon's mass shell. They give rise to the first term in Lüscher's formula for the nucleon mass shift:

$$\begin{aligned} m_N(L) - m_N &= \frac{9}{4}\left[\frac{m_\pi}{m_N}\right]^2 \frac{g_{\pi N}^2}{4\pi L}\, e^{-\sqrt{m_\pi^2 - \nu_B^2}L} \\ &\quad - \frac{3}{16\pi^2 m_\pi L}\,\frac{m_\pi}{m_N}\int_{-\infty}^{\infty} dy\; e^{-\sqrt{m_\pi^2 + y^2}L}\, F_{\pi N}(iy) \\ &\quad + O(e^{-\bar{m}L}). \end{aligned} \tag{2.22}$$

Note that the second term has, up to the suppression factor m_π/m_N, the same form as the pion formula (2.10). $\bar{m}$ is now some mass with $\bar{m} \geq \sqrt{3/2}\, m_N$, while for the πN forward scattering amplitude we have $F_{\pi N}(\nu) \equiv 6m_N[A^+(\nu)+\nu B^+(\nu)]$ with the usual Lorentz invariant amplitudes A^+ and B^+ (see *e.g.* Ref. [105]).

In order to estimate $F_{\pi N}(\nu)$ near $\nu = 0$, one can separate out the pseudovector Born term [54],

$$F_{\pi N}(\nu) = \frac{6 g_{\pi N}^2 \nu_B^2}{\nu_B^2 - \nu^2} + \bar{F}_{\pi N}(\nu), \tag{2.23}$$

and expand the remainder in a convergent power series,

$$\bar{F}_{\pi N}(\nu) = \sum_{k=0}^{\infty} r_k \Big(\frac{\nu}{m_\pi}\Big)^{2k}, \quad |\nu| < m_\pi, \tag{2.24}$$

with the coefficients

$$r_0 = -60.7, \quad r_1 = 45.3, \quad r_2 = 8.1 \tag{2.25}$$

and the effective coupling $g_{\pi N}^2/4\pi = 14.3$ (from πN dispersion analyses, see Ref. [106]). It is instructive to look separately at the various contributions to the nucleon mass shift. Writing the truncated series $\bar{F}_{\pi N}^{(K)}(\nu)$ for finite K as

$$\bar{F}_{\pi N}^{(K)}(\nu) = \sum_{k=0}^{K} r_k \Big(\frac{\nu}{m_\pi}\Big)^{2k}, \quad |\nu| < m_\pi, \tag{2.26}$$

the three contributions due to one-nucleon exchange diagrams, the pseudovector Born term and $\bar{F}_{\pi N}^{(K)}$ read

$$\Delta_1(L) = \frac{9}{4}\left[\frac{m_\pi}{m_N}\right]^2 \frac{g_{\pi N}^2}{4\pi}\, \frac{e^{-\sqrt{m_\pi^2-\nu_B^2}\,L}}{L}, \tag{2.27a}$$

$$\Delta_2(L) = -\frac{9}{\pi m_\pi L}\, \frac{m_\pi}{m_N}\, \frac{g_{\pi N}^2}{4\pi} \int_0^\infty dy\, \frac{e^{-\sqrt{m_\pi^2+y^2}\,L}}{1+y^2/\nu_B^2}, \tag{2.27b}$$

$$\Delta_3^{(K)}(L) = -\frac{3}{16\pi^2 m_\pi L}\, \frac{m_\pi}{m_N} \int_{|y|<m_\pi} dy\, e^{-\sqrt{m_\pi^2+y^2}\,L}\, \bar{F}_{\pi N}^{(K)}(iy). \tag{2.27c}$$

Fig. 2.2 displays the different terms in units of the nucleon mass m_N as a function of $m_\pi L$, at the physical mass ratio $m_\pi/m_N = 0.147$. The powers of this ratio in Eqns. (2.27a)–(2.27c) lead to a strong suppression of all three contributions, so that Lüscher's formula predicts a very small mass shift of only a little more than 2% even for $m_\pi L = 1$.[2] Besides the presence of powers of m_π/m_N another reason for the smallness of the predicted effect is that for realistic m_π/m_N the positive contribution Δ_1 is almost canceled by the integral over the pole term in $F_{\pi N}$, Δ_2. The nucleon mass shift is therefore almost entirely accounted for by the integral over the non-pole contribution $\bar{F}_{\pi N}$, here given by $\Delta_3^{(2)}$. (It comes out positive because the integrand is negative for small values of $|y|$.) It is also remarkable that even if $\bar{F}_{\pi N}(\nu)$ is kept constant at $\bar{F}_{\pi N}(0) = -60.7$ (which is equivalent to truncating the series (2.26) at $K = 0$) one still obtains

[2] We will see in Chapter 4 that the predicted mass shift is too small to account for the effect observed in our simulations.

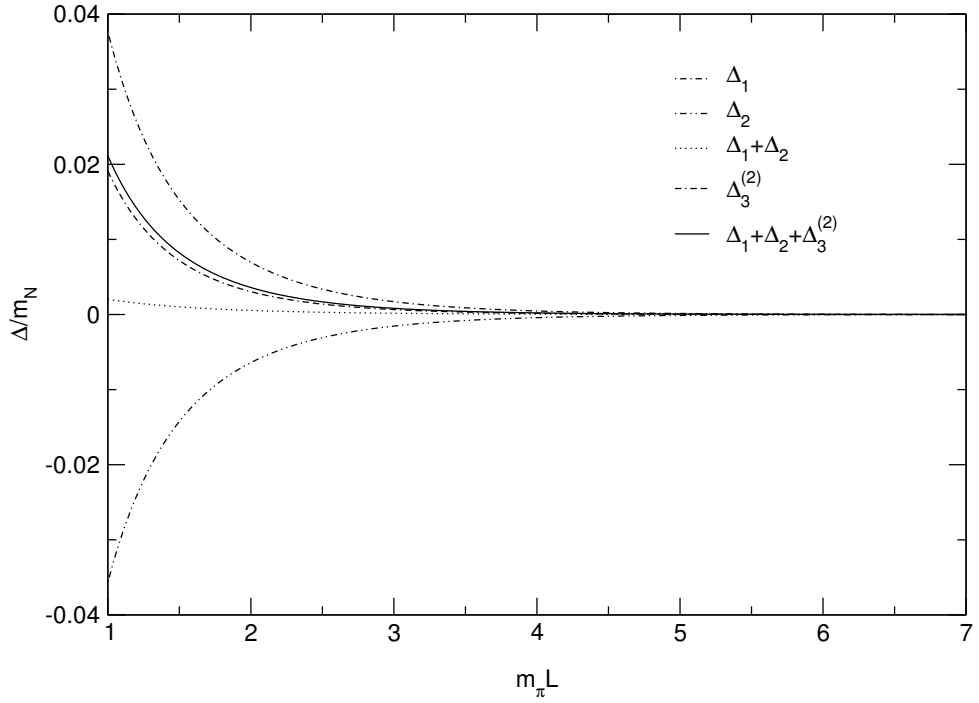

Figure 2.2: Contributions to the relative finite-size mass shift of the nucleon at the physical value of m_π/m_N. Δ_1, Δ_2 and $\Delta_3^{(2)}$ are due to one-nucleon exchange diagrams, the pseudovector Born term and $\bar{F}_{\pi N}^{(2)}$, respectively.

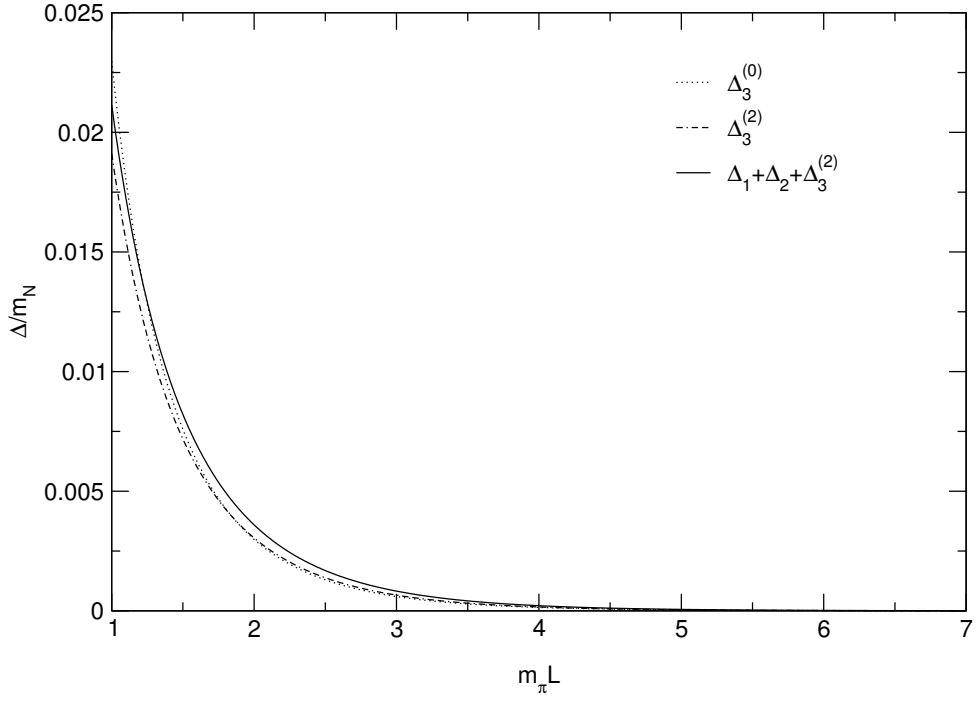

Figure 2.3: Comparison of the leading non-pole contribution $\Delta_3^{(0)}$ with $\Delta_3^{(2)}$ and the complete sum of all contributions to Lüscher's formula for the nucleon mass-shift at the physical value of m_π/m_N.

a qualitatively acceptable description of the predicted nucleon mass shift. This is demonstrated in Fig. 2.3, where we compare the resulting "zeroth" approximation

$$\frac{\Delta_3^{(0)}(m_\pi L)}{m_N} = -\bar{F}_{\pi N}(0)\,\frac{3}{8\pi^2}\left[\frac{m_\pi}{m_N}\right]^2 \frac{K_1(m_\pi L)}{m_\pi L} \tag{2.28}$$

$$\simeq -\bar{F}_{\pi N}(0)\,\frac{3}{4(2\pi)^{3/2}}\left[\frac{m_\pi}{m_N}\right]^2 \frac{e^{-m_\pi L}}{(m_\pi L)^{3/2}} \tag{2.29}$$

with $\Delta_3^{(2)}$ and the complete sum of all contributions (2.27) (normalized by m_N, respectively). Note that in their functional form the approximations (2.28) and (2.29) correspond, up to the different amplitude and the factors $(m_\pi/m_N)^2$, precisely to the pion mass shift formulae (2.18) and (2.19).

2.2 Previous Results from Full QCD Simulations

Finite-size effects in the masses of the pion, rho and nucleon were extensively studied in numerical simulations with dynamical staggered quarks about twelve years ago by Fukugita *et al.* [56, 57, 58, 59, 60]. On the one hand it was found that finite-size effects in full lattice QCD are much larger than those in quenched simulations. Based on a comprehensive study of the dependence of hadron masses on the boundary conditions the difference was ascribed to a partial cancellation of the finite-size effects among $Z(3)$-related gauge configurations in quenched lattice QCD. Such a cancellation does not occur in full QCD, as the center-symmetry of the pure gauge action is broken by dynamical quarks. On the other hand, the finite-size effects of hadron masses in full QCD simulations turned out to be much larger than predicted by Lüscher's asymptotic formula. In fact, in the parameter regime studied by Fukugita *et al.* they could be well described by a power law

$$\Delta m_H(L) \propto L^{-n} \quad \text{with} \quad n \simeq 2..3. \tag{2.30}$$

This and the fact that the nucleon was found to show a larger finite-size effect than the pion (which has the larger Compton wave length) was considered as supportive of the idea that the origin of the effect was a distortion of the hadronic wave-function, as opposed to Lüscher's picture of a squeezed cloud of virtual pions surrounding point-like hadrons. To corroborate this assumption, antiperiodic spatial boundary conditions where imposed in the calculation of the quark propagator on their smallest lattice and at their lightest quark mass. The observation that the resulting masses of the π- and ρ-mesons now displayed a negative finite-size effect lead them to the conclusion that the finite-size effects in their hadron masses were indeed a consequence of the finite hadron extent: if it had been caused by virtual mesons going around the lattice, the mesonic correlation functions should have been unaffected by the sign flip in the quark propagator.

Fukugita *et al.* proposed two possible explanations for the observed power law, which we will briefly summarize in the following. First they examined how the effect of virtual particles going around the lattice is modified when the finite extent of hadrons is taken into account. Let us consider a hadron in a box of size L. If we assume periodic boundary conditions, the hadron will see mirror images of itself at distances $\mathbf{n}L$, with $\mathbf{n}$ being a 3-dimensional vector with integer components. If $V(\mathbf{x})$ is the potential between two hadrons, the self-energy δE of the hadron is

given by

$$\delta E = \sum_{\mathbf{n}} V(\mathbf{n}L). \tag{2.31}$$

For large L this can be approximated by $V(0) + 6V(L)$. If we further assume a one-particle exchange potential which is, asymptotically, proportional to $\exp(-mr)/r$ (where m is the mass of the exchanged particle), we essentially recover, at least qualitatively, the exponential behavior of the finite-size mass shift predicted by Lüscher.

One can now incorporate the effect of the finite spatial extent of the hadron by rewriting Eq. (2.31) as

$$\delta E = \frac{1}{L^3} \sum_{\mathbf{n}} \hat{V}\left(\mathbf{n}\frac{2\pi}{L}\right), \tag{2.32}$$

where the Fourier-transformed one-particle exchange potential $\hat{V}(\mathbf{k})$ is given by

$$\hat{V}(\mathbf{k}) = \frac{F(\mathbf{k}^2)}{\mathbf{k}^2 + m^2} \tag{2.33}$$

and $F(\mathbf{k}^2)$ is a model-dependent form factor. Independently of the concrete choice of the form factor one can assume that in the regime of small and intermediate lattice sizes L, where the minimal allowed non-zero momentum $2\pi/L$ is quite large, the form factor should cause a rather strong suppression. The $\mathbf{n} = \mathbf{0}$ contribution would then be the dominant term in (2.32), and the finite-size corrections to the masses of hadrons can be expected to be proportional to $1/L^3$. For sufficiently large sizes L, however, the $1/L^3$ behavior of the finite-size mass shift is expected to disappear in favor of an exponential correction proportional to $\exp(-mL)/L$. Numerical tests have shown that the lattice size L where this happens depends on the behavior of the assumed form factor.

An alternative picture also producing a power-law is based on the following non-relativistic argument: If we suppose that the quarks inside a hadron are bound by some confining potential and characterize the asymptotic decrease of the wave function $\psi(r)$ by the length scale r', then a small finite box with Dirichlet-type boundary conditions would lead to a reduced characteristic length $r' \propto L$. As a consequence of the steeper fall-off of the squeezed wave-function the kinetic energy of the ground state is increased as $1/L^2$. While the details of the exponent of the power law depend on the adopted model assumptions, the power law behavior itself is a general feature of such a simple non-relativistic quark model picture. In the argument given above we have assumed Dirichlet-type boundary conditions, meaning that the wave function at the boundary is kept small. Fukugita *et al.* argue that this situation is given if periodic boundary conditions are used for both the valence quarks in the calculation of hadron correlators and the sea quarks in the generation of gauge configurations, which is the case for all the simulations considered in this work.

2.3 Finite-Size Effects in the Nucleon from Chiral Perturbation Theory

In a recent publication Ali Khan *et al.* calculate the volume dependence of the nucleon mass in the framework of $N_f = 2$ relativistic baryon chiral perturbation theory up to and including $O(p^4)$ in the chiral expansion [66]. Their analysis is based on the fundamental observation that finite-size effects in hadron masses can be calculated from the same effective field theories

that also describe the quark mass dependence [71, 72, 73]. As we have already argued in the previous sections, if the volume is not too small, the finite-size effects originate from virtual pions propagating "around the world". In ChPT this is the regime of the so-called p-expansion which is valid for small pion masses $m_\pi = O(p)$ and large volumes L^3 with $1/L = O(p)$, so that $m_\pi L = O(1)$.[3]

Replacing the continuous integral over the spatial loop momentum in the relevant $O(p^3)$ contribution to the nucleon mass by a discrete sum over the allowed momenta in a finite volume of linear size L, Ali Khan *et al.* obtain

$$\Delta_a(L) = \frac{3g_A^2 m_0 m_\pi^2}{16\pi^2 f_\pi^2} \int_0^\infty dx \sum_{\mathbf{n}}{}' K_0\Big(L|\mathbf{n}|\sqrt{m_0^2 x^2 + m_\pi^2(1-x)}\,\Big) \tag{2.34}$$

for the nucleon finite-size mass shift $m_N(L) - m_N$ at NLO. Here and in the following the constants g_A and f_π are to be taken in the chiral limit, m_0 is the nucleon mass in the chiral limit and the pion mass m_π parameterizes the quark mass via the Gell-Mann-Oakes-Renner relation. The pion decay constant f_π is normalized such that its physical value is 92.4 MeV. K_0 is a modified Bessel function, and the sum extends over all spatial 3-vectors $\mathbf{n}$ with integer components n_i, $i = 1, 2, 3$, except $\mathbf{n} = \mathbf{0}$. n_i can be interpreted as the number of times the pion goes around the lattice in the i-th direction.

Similarly, at $O(p^4)$ an additional contribution to the difference between the nucleon mass in a volume of size L^3 and in infinite volume is given by

$$\Delta_b(L) = \frac{3m_\pi^4}{4\pi^2 f_\pi^2} \sum_{\mathbf{n}}{}' \left[(2c_1 - c_3)\frac{K_1(|\mathbf{n}|m_\pi L)}{|\mathbf{n}|m_\pi L} + c_2 \frac{K_2(|\mathbf{n}|m_\pi L)}{(|\mathbf{n}|m_\pi L)^2}\right], \tag{2.35}$$

where c_1, c_2 and c_3 are effective coupling constants and K_1 and K_2 are again modified Bessel functions. The complete result for the nucleon finite-size mass shift at NNLO is thus

$$m_N(L) - m_N = \Delta_a(L) + \Delta_b(L) + O(p^5). \tag{2.36}$$

Compared with Lüscher's asymptotic formula an important merit of (2.36) is that virtual pions which cross the boundaries of the finite box (with periodic boundary conditions) more than just once are taken into account. This is crucial to the applicability of the formula also at rather small box volumes, that we will demonstrate in Chapter 4. The numerical evaluation of Eq. (2.36) does indeed show that unless $m_\pi L$ is rather large the sub-leading terms with $|\mathbf{n}| > 1$ are not negligible. The other advantage is that (2.36) incorporates information from chiral perturbation theory on the quark mass dependence of m_N, $g_{\pi N}$ and the scattering amplitude. Lüscher's formula (2.22) can be recovered, however, by restricting the sums in (2.34) and (2.35) to those vectors $\mathbf{n}$ with $|\mathbf{n}| = 1$.[4]

In Ref. [66] the parameters of the chiral expansion in (2.34) and (2.35) are taken partly from phenomenology and partly from a fit of numerical data for m_N from relatively fine and large

[3] The chiral series can also be organized in form of the so-called ϵ-expansion, which is valid for $m_\pi L \ll 1$ [107].

[4] Actually only up to a factor of two in the first term (Δ_1 in (2.27a)) which in Lüscher's derivation originates from one-nucleon exchange diagrams.

lattices to the (infinite volume) $O(p^4)$ formula [108]

$$\begin{aligned} m_N &= m_0 - 4c_1 m_\pi^2 - \frac{3g_A^2}{32\pi f_\pi^2}\, m_\pi^3 \\ &\quad + \left[e_1^r(\lambda) - \frac{3}{64\pi^2 f_\pi^2}\left(\frac{g_A^2}{m_0} - \frac{c_2}{2}\right) - \frac{3}{32\pi^2 f_\pi^2}\left(\frac{g_A^2}{m_0} - 8c_1 + c_2 + 4c_3\right) \ln\frac{m_\pi}{\lambda} \right] m_\pi^4 \\ &\quad + \frac{3g_A^2}{256\pi f_\pi^2 m_0^2}\, m_\pi^5 + O(m_\pi^6), \end{aligned} \tag{2.37}$$

which has been derived using infrared regularization [109]; the counterterm $e_1^r(\lambda)$ is taken at the renormalization scale λ. With all parameters fixed in this way, the formulae (2.34) and (2.35) provide parameter-free predictions of the finite-volume effects in the nucleon mass.

Chapter 3

Numerical Simulation

Aiming at the simulation of QCD with light quarks, but faced with limited computing resources, it is an interesting question if one can possibly get away with simulations on small and medium-sized lattices and yet obtain infinite-volume results through extrapolation or directly calculable finite-size corrections. One goal of the GRAL project is to address this question by an investigation into the volume dependence of the light hadron masses in the currently accessible parameter regime. This chapter deals with the simulation aspects of the project. We present details about the generation of the gauge field configurations, describe the calculation of quark propagators and hadronic correlation functions and finally introduce the parameterizations to which these correlation functions were fitted to obtain the desired physical quantities. Finally we introduce our methods for fitting and error analysis. The results of our simulations will then be presented and discussed in the next chapter.

A numerical investigation of finite-size effects requires data from simulations that differ only in the physical lattice volume, while all other parameters (gauge coupling and quark mass) are kept fixed. Although most of the gauge configurations that we analyze in this work have been newly generated, the GRAL project has benefited substantially from the fruitful work of its forerunners, the SESAM and TχL projects [35, 36].

This is reflected, on the one hand, in the Hybrid Monte Carlo (HMC) code that we could freely borrow from the SESAM/TχL project. The most recent version of the original TAO code was employed on the APE100 (QH4) parallel computer [81] at DESY Zeuthen until the machine finally broke down in January 2003. As the code had been ported to the newer APEmille [82] already some time before, production could smoothly be shifted to this machine. In fact, some GRAL runs were already under way on APEmille at this time. In addition, a C/MPI version of the SESAM HMC code [110] had been developed for the cluster computer ALiCE [83] at the University of Wuppertal. Since its first employment for production runs in November 2002 this code version has been running very efficiently on ALiCE. Like the original TAO code it features the locally-lexicographic SSOR preconditioned BiCGStab solver for a fast inversion of the fermion matrix [75, 76]. While the bulk of the code is written in C (using the standard MPICH-library [111] for message-passing), some time-critical core routines are coded in assembler for further acceleration [112]. A lot of effort has also been invested into the optimization of the parallelization and the data layout [113].

On the other hand, gauge field ensembles from SESAM and TχL runs have directly entered our analysis. As the data from both SESAM/TχL and GRAL were produced using the same unimproved $N_f = 2$ Wilson action they could be analyzed on an equal footing.

In the following we specify the parameters of our simulations in detail. For reference and for comparison we include in the tables also those SESAM simulations that have not been used for this work.

3.1 Simulation Parameters

We have performed a large-scale simulation of full QCD with two degenerate Wilson quarks at two different values of the gauge coupling parameter, $\beta = 5.32144$ and $\beta = 5.6$, for one and two different values of κ, respectively. The larger β corresponds to the SESAM/TχL value. The smaller β and the corresponding κ of 0.1665 result from a linear extrapolation of lines of constant $M_{\rm PS}/M_{\rm V}$ and $1/(M_{\rm PS}L)$ in the (β,κ)-plane, based on SESAM/TχL data and aiming at $M_{\rm PS}/M_{\rm V} \lesssim 0.5$ and $1/(M_{\rm PS}L) \approx 0.2$ on a 16^3-lattice [51]. For every (β,κ)-combination considered in this work we have produced gauge field configurations for at least three different lattice volumes $(La)^3$ with L varying between 10 and 16, thus complementing ensembles from SESAM and TχL with $L = 16$ and 24, respectively. Generating the configurations we imposed periodic boundary conditions in all four space-time dimensions for the gauge field, while for the pseudofermions we used periodic boundary conditions in the spatial directions and antiperiodic boundary conditions in the temporal direction. In addition to the original SESAM code that was employed on the 512-node APE100 (QH4) we used a modified code version on APEmille [82]. On APEmille, a 128-node partition ("crate") was used to generate the $16^3 \times 32$-lattices, while the $12^3 \times 32$-lattices were produced on a "unit" consisting of 32 nodes. On ALiCE, the 128-node "Alpha Linux Cluster Engine" at the University of Wuppertal, a C/MPI-version of the SESAM code (written mainly by Z. Sroczynski) was employed on partitions of 16 ($12^3 \times 32$ and $14^3 \times 32$ lattices) and 8 processors ($10^3 \times 32$ lattice). All the codes are implementations of the Φ-version [114] of the HMC algorithm for two degenerate quark flavors as discussed in Section 1.6.1. The bulk of the CPU costs for full QCD simulations with the HMC algorithm goes into the time consuming repeated inversion of the quark matrix M. Throughout the simulations we employed the Bi-Conjugate Gradient stabilized (BiCGStab) algorithm with ll-SSOR preconditioning for the solve of the linear system $(M^\dagger M)X = \phi$. This was done in a two-step procedure: first we solved $M^\dagger Y = \phi$ for Y and then solved $MX = Y$ for X. The TAO code on APE additionally features an implementation of the chronological start vector guess proposed in [115].

Tables 3.1–3.3 give a detailed overview over the production runs we have carried out (referred to as GRAL). For reference and to allow for direct comparison we also list the respective figures for all previous SESAM/TχL runs. Configurations from the SESAM/TχL simulations at $(\beta,\kappa,L) = (5.6, 0.1575, 16)$, $(5.6, 0.1575, 24)$ and $(5.6, 0.158, 24)$ have been included in our analysis of finite-size effects. Alongside the gauge coupling parameter β of Eq. (1.36) and the hopping parameter κ of Eq. (1.46) we display the simulated lattice volumes. While the number of lattice sites in the spatial directions, L, was varied, the time-like extent T was kept fixed at 32 ($T = 40$ in the case of TχL).

Except for some early SESAM simulations (or parts thereof) featuring an even-odd representation of the quark matrix, ll-SSOR preconditioning was used in all later runs. The depth of the extrapolation in the chronological start vector guess, $N_{\rm csg}$, was fixed to 7 in all the GRAL runs on APE machines. The step size δt in the leapfrog integration and the average number of integration steps in the molecular dynamics update, $N_{\rm MD}$, were generally chosen such as to yield an acceptance rate of 60-90% in the accept-reject step at the end of each trajectory in the HMC. The trajectory lengths $N_{\rm MD}$ were uniformly varied in the intervals given in Table 3.1 in

β	κ	L^3T	Precnd.	N_{csg}	N_{MD}	δt	Acc.	$\langle N_{\text{iter}} \rangle$	$\langle \square \rangle$
5.32144	0.1665	$12^3 32$	SSOR	-	125 ± 20	0.004	71%	*147(6)*	0.53949(14)
		$14^3 32$		-	125 ± 20	0.004	64%	*130(6)*	0.53879(15)
		$16^3 32$		7	200 ± 40	0.005	41%	315(9)	0.538290(65)
					125 ± 20	0.004	65%		
5.5	0.1580	$16^3 32$	SSOR	7	100 ± 20	0.010	77%	45(1)	0.555471(45)
	0.1590	$16^3 32$	SSOR	7	100 ± 20	0.010	71%	85(1)	0.558164(38)
	0.1596	$16^3 32$	SSOR	7	100 ± 20	0.010	61%	138(2)	0.559745(58)
	0.1600	$16^3 32$	SSOR	7	100 ± 20	0.010	40%	216(3)	0.560776(47)
5.6	0.1560	$16^3 32$	e/o	6	100 ± 20	0.010	82%	86(1)	0.569879(25)
	0.1565	$16^3 32$	SSOR	7	100 ± 20	0.010	77%	90(1)	0.570721(22)
	0.1570	$16^3 32$	SSOR	7	100 ± 20	0.010	67%	133(1)	0.571592(27)
	0.1575	$10^3 32$	SSOR	-	100 ± 20	0.010	87%	*63(1)*	0.573114(27)
		$12^3 32$	SSOR	7	100 ± 20	0.010	76%	146(2)	0.572771(30)
		$14^3 32$	SSOR	-	100 ± 20	0.010	62%	*79(1)*	0.572598(22)
		$16^3 32$	e/o	11	100 ± 20	0.010	78%	293(6)	0.572550(27)
			SSOR	3	71 ± 12	0.007	73%	160(6)	
		$24^3 40$	SSOR	6	125 ± 20	0.004	80%	109(1)	0.572476(13)
	0.1580	$12^3 32$	SSOR	7	125 ± 20	0.008	85%	150(5)	0.573793(32)
		$14^3 32$		-	100 ± 20	0.005	88%	*113(1)*	0.573677(25)
		$16^3 32$		7	125 ± 20	0.006	66%	302(5)	0.573461(25)
		$24^3 40$		6	125 ± 20	0.004	62%	256(7)	0.573375(16)

Table 3.1: Overview of the GRAL simulation parameters in the context of all previous SESAM/TχL simulations. Note that for ALiCE runs (see also Table 3.2) the *slanted* numbers for $\langle N_{\text{iter}} \rangle$ refer to the solve of $M^\dagger Y = \phi$ only, whereas in the case of APE runs they refer to the full two-step solution of $(M^\dagger M)X = \phi$. Details are explained in the text.

order to avoid deadlocks in periodic orbits of phase space due to the presence of well defined Fourier modes [116]. Both for decreasing quark mass and increasing lattice volume (all other parameters kept fixed, respectively) we observe a drop in the acceptance rate as anticipated. $\langle N_{\text{iter}} \rangle$ denotes the average number of iterations the Krylov-subspace solver needs to converge when the fermionic matrix is inverted. The stopping accuracy $R \equiv \|MX - \phi\|/\|X\|$ for the solve of the linear system $MX = \phi$ was constantly set to $R = 10^{-8}$ in all GRAL runs. For the runs on ALiCE the *slanted* numbers for $\langle N_{\text{iter}} \rangle$ quoted in Table 3.1 refer to the solve of $M^\dagger Y = \phi$ only, whereas for the APE runs they refer to the full two-step solution of $(M^\dagger M)X = \phi$ (see Table 3.2 for machines). For a comparison a relative factor of $k \approx 2$ must therefore be taken into account. $\langle \square \rangle$ in the last column is the ensemble average of the plaquette as defined in Eq. (1.35). In order to boost the initially low acceptance rate of only 41% in the simulation at $(\beta, \kappa, L) = (5.32144, 0.1665, 16)$ we decreased the step size δt from 0.005 to 0.004 and reduced N_{MD} from 200 ± 40 to 125 ± 20 at some stage of the simulation.

Table 3.2 shows estimates of the simulation costs for all runs on ALiCE and for those (parts

β	κ	L^3T	Speed [Gflop/s]	$T_{\rm tot}$ [h]	Cost [Tflops-h]	Machine	$N_{\rm proc}$	Project
5.32144	0.1665	$12^3 32$	3.3	8875	30	ALiCE	16	GRAL
		$14^3 32$	3.2	8014	26	ALiCE	16	
		$16^3 32$	10.5	5575	59	QH4	512	
			6.1	2449	15	APEm	128	
5.5	0.1580	$16^3 32$	10.4	349	4	QH4	512	SESAM
	0.1590	$16^3 32$	10.3	987	10	QH4	512	SESAM
	0.1596	$16^3 32$	9.1	1683	15	QH4	512	SESAM
	0.1600	$16^3 32$	10.5	2296	24	QH4	512	SESAM
5.6	0.1560	$16^3 32$				QH2	256	SESAM
	0.1565	$16^3 32$	7.0	1534	11	QH2	256	SESAM
	0.1570	$16^3 32$	6.7	2350	16	QH2	256	SESAM
	0.1575	$10^3 32$	1.8	5638	10	ALiCE	8	GRAL
		$12^3 32$	1.5	6487	10	APEm	32	GRAL
		$14^3 32$	2.9	7570	22	ALiCE	16	GRAL
		$16^3 32$	5.4	>932	>5	QH2	256	SESAM
		$24^3 40$	8.9	6962	62	QH4	512	TχL
	0.1580	$12^3 32$	1.5	3136	5	APEm	32	GRAL
		$14^3 32$	3.1	9240	29	ALiCE	16	GRAL
		$16^3 32$	6.1	8455	52	APEm	128	GRAL
		$24^3 40$	10.0	11151	112	QH4	512	TχL

Table 3.2: Estimates of the HMC code performances on the various machines used for the generation of gauge fields, including previous SESAM/TχL simulations. Details are explained in the text.

of) runs on APE machines in which SSOR preconditioning was used. We have estimated the code/machine performance on the basis of available run log data according to

$$\text{Speed} \approx 4 \cdot 1404 \cdot L^3 T \sum_{t=1}^{T_{\rm MC}} k N_{\rm iter}(t) N_{\rm MD}(t) / T_{\rm tot}, \tag{3.1}$$

where

$$T_{\rm tot} = \sum_{t=1}^{T_{\rm MC}} T(t) \tag{3.2}$$

is the integrated simulation time needed for the generation of $T_{\rm MC}$ trajectories. In each of the $N_{\rm MD}(t)$ molecular dynamics steps in trajectory t, $kN_{\rm iter}(t)$ BiCGStab iterations are needed (on average) for the inversion of $M^\dagger M$ (to the required accuracy R). The inversion is done in 2 steps, respectively, each of which comprises a forward and a backward solve of the ll-SSOR preconditioned system. This yields a total of 4 calls to the forward/backward solver, each of which requires 1404 floating point operations ("flop") per lattice site. The factor k in front of $N_{\rm iter}(t)$ has been inserted for convenience; it is equal to 1 for simulations on APE machines and

β	κ	L^3T	T_{MC}	T_{therm}	T_{equi}	Δt	N_{conf}
5.32144	0.1665	$12^3 32$	10100	1500	8600	50 ± 6	170
		$14^3 32$	5900	800	5100	40 ± 4	129
		$16^3 32$	15300	8600	6700	40 ± 4	169
5.5	0.1580	$16^3 32$	4000	1000	3000	25 ± 3	119
	0.1590	$16^3 32$	6000	1000	5000	25 ± 3	200
	0.1596	$16^3 32$	5500	500	5000	25 ± 3	199
	0.1600	$16^3 32$	5500	500	5000	25 ± 3	200
5.6	0.1560	$16^3 32$	5700	600	5100	25	198
	0.1565	$16^3 32$	5900	700	5200	24	208
	0.1570	$16^3 32$	6000	1000	5000	25	201
	0.1575	$10^3 32$	16000	2600	13400	48 ± 4	278
		$12^3 32$	8000	700	7300	30 ± 4	243
		$14^3 32$	8400	1400	7000	30 ± 4	231
		$16^3 32$	6500	1400	5100	25	206
		$24^3 40$	5100	500	4600	25	185
	0.1580	$12^3 32$	3000	500	2500	24 ± 2	103
		$14^3 32$	9100	1300	7800	40 ± 4	195
		$16^3 32$	6500	1100	5400	30 ± 4	181
		$24^3 40$	4500	700	3800	24	158

Table 3.3: Overview of the various HMC run lengths, thermalization times and numbers of equilibrium configurations. N_{conf} is the number of analyzed gauge configurations, separated in Monte Carlo time by ΔT. See the text for details.

set to 2 for runs on ALiCE. As the remaining program overhead of the HMC (energy calculations, computation of the fermionic force *etc.*) has not been added to the flop count, the numbers for both speed and cost in Table 3.2 have to be considered as lower bounds to the true speed and cost. They do, however, provide reasonably good estimates as the solver part is by far the most cost-intensive part of a dynamical fermion simulation.

Table 3.3 shows some more simulation details. T_{MC} denotes the total number of generated trajectories, the first T_{therm} of which we attribute to the thermalization phase and therefore discard, so that we are left with T_{equi} equilibrium configurations, respectively.[1] N_{conf} configurations out of these, separated by Δt trajectories (with a uniform, random variation as given in Table 3.3), have been analyzed further. In determining T_{therm} and Δt we let ourselves be guided by the autocorrelation analysis to be discussed next.

[1] In the thermalization phase of each production run we approached the respective target quark mass adiabatically from larger quark masses. These initial trajectories are in general not counted here. An exception to this rule is the run at $(\beta, \kappa, L) = (5.32144, 0.1665, 16)$ where a rather long initial tuning phase incorporated several changes of the simulation parameters.

3.2 Autocorrelation Times

Because successive elements of a time-series[2] resulting from an updating process are correlated, it is convenient to analyze the autocorrelation in the observables one is interested in. This serves two purposes: First, the *exponential* autocorrelation time is related to the length of the thermalization phase of the Markov chain, *i.e.* the time that the system needs to converge from its initial state to equilibrium. In order to avoid systematic errors in the final results due to an initialization bias one should discard the data from the initial transient (of length T_{therm}, say). Second, the variance of the sample mean in a dynamic Monte Carlo method (like the HMC) is a factor of two times the *integrated* autocorrelation time higher than it would be for independent sampling. Put differently, if we consider an observable A, a run of length T_{MC} contains only $T_{\text{MC}}/2\tau_{\text{int}}^A$ effectively independent data points. If a method like the blocked jackknife is used in the error analysis, this is, in general, not a problem, because one can just use the full sample to calculate means, choose an appropriate block size and then let the jackknife take care of autocorrelations in the statistical error analysis.[3] This has the obvious advantage that no statistics is lost. However, if A is a derived quantity and its computation expensive (as it is the case for all quantities based on the quark propagator M^{-1}) it is possible (and desirable) to save computer time by calculating A only on a subsample, consisting of ensemble elements with a certain separation Δt in Monte Carlo time.

For choosing both T_{therm} and Δt it is helpful to have some knowledge of τ_{exp}^A and τ_{int}^A for suitable observables A. In order to facilitate the autocorrelation analysis for our simulations we generally saw to it that the run parameters were not changed after the initial tuning phase so as to have the HMC evolve under stable conditions. (The one exception to this rule is the run at $(\beta, \kappa, L) = (5.32144, 0.1665, 16)$ where the acceptance rate was at first so low that we had to readjust δt and N_{MD} at some point. The autocorrelation times for the resulting sub-samples have been determined separately.) In Appendix B the time-series of the plaquette and the average number of solver iterations, N_{iter}, are shown for all GRAL runs. A suitable estimator of the true autocorrelation (or *autocovariance*) function for a finite time-series A_t, $t = 1, \ldots, T_{\text{MC}}$, is given by

$$C^A(t) = \frac{1}{T_{\text{MC}} - t} \sum_{s=1}^{T_{\text{MC}}-t} \left(A_s - \langle A \rangle_L\right) \left(A_{s+t} - \langle A \rangle_R\right), \tag{3.3}$$

where the use of the "left" and "right" mean-value estimators

$$\langle A \rangle_L = \frac{1}{T_{\text{MC}} - t} \sum_{r=1}^{T_{\text{MC}}-t} A_r \quad \text{and} \quad \langle A \rangle_R = \frac{1}{T_{\text{MC}} - t} \sum_{r=1}^{T_{\text{MC}}-t} A_{r+t} \tag{3.4}$$

in general leads to a faster convergence of $C^A(t)$ to the true autocorrelation function for $T_{\text{MC}} \to \infty$ [117]. In Figures B.1–B.10 we plot the estimator for the normalized autocorrelation function,

$$\rho^A(t) = C^A(t)/C^A(0), \tag{3.5}$$

for $A = 1 - \square$ (called "$1 - P$" in the appendix) and $A = N_{\text{iter}}$. From fits of ρ^A to an exponential we extract estimates for the respective exponential autocorrelation times τ_{exp}^A, defined as

$$\tau_{\text{exp}}^A = \limsup_{t \to \infty} \frac{t}{-\log|\rho^A(t)|}. \tag{3.6}$$

[2] Monte-Carlo "time", measured in trajectories.

[3] The blocked jackknife can even be used to estimate τ_{int}^A (see Section 3.8).

β	κ	L^3T	$\tau_{\mathrm{exp}}^{N_{\mathrm{iter}}}$	$\tau_{\mathrm{int}}^{N_{\mathrm{iter}}}$	$\tau_{\mathrm{exp}}^{1-\square}$	$\tau_{\mathrm{int}}^{1-\square}$
5.32144	0.1665	$12^3 32$	103(16)	116(9)	106(18)	99(5)
		$14^3 32$	90(14)	77(6)	91(13)	52(3)
		$16^3 32$	97(14)	105(7)	77(9)	54(4)
			187(43)	154(24)	147(20)	113(10)
5.5	0.1580	$16^3 32$	21(5)	20(1)	27(3)	16(1)
	0.1590	$16^3 32$	25(7)	25(1)	31(3)	13(1)
	0.1596	$16^3 32$	74(12)	38(2)	37(11)	17(1)
	0.1600	$16^3 32$	56(6)	46(3)	64(7)	34(2)
5.6	0.1560	$16^3 32$	49(11)	24(2)	10(2)	6(1)
	0.1565	$16^3 32$	29(6)	19(4)	7(1)	5(1)
	0.1570	$16^3 32$	35(6)	25(5)	9(3)	6(1)
	0.1575	$10^3 32$	62(7)	28(2)	15(3)	5(1)
		$12^3 32$	24(3)	20(1)	15(3)	6(1)
		$14^3 32$	88(27)	34(3)	26(8)	8(1)
		$16^3 32$	47(7)	33(4)	18(6)	7(4)
		$24^3 40$	51(7)	36(4)	11(2)	7(3)
	0.1580	$12^3 32$	25(5)	24(1)	9(3)	4(1)
		$14^3 32$	27(3)	24(2)	19(2)	8(2)
		$16^3 32$	57(20)	32(3)	19(5)	11(3)
		$24^3 40$	61(19)	50(5)	20(10)	20(2)

Table 3.4: Measured exponential and integrated autocorrelation times for the average number of solver iterations, N_{iter}, and the plaquette.

The notorious difficulty of determining autocorrelation times for relatively short time-series is apparent in most of the plots of $\rho^A(t)$ in the appendix. We therefore aim for rough estimates of the exponential autocorrelation time only and refrain from an elaborate optimization of the fit ranges. We have checked, however, that the differencing method described in Ref. [117] gives consistent results. The measured values for τ_{exp}^A, displayed in Table 3.4, are generally larger than the integrated autocorrelation times τ_{int}^A that we measure with the help of Sokal's "windowing" procedure and which are also shown in the table. We use the finite sum

$$\tau_{\mathrm{int}}^A = \frac{1}{2} + \sum_{t=1}^{T_{\mathrm{cut}}} \rho^A(t) \tag{3.7}$$

with a variable cut-off T_{cut} to estimate τ_{int}^A. Plotting the resulting values against T_{cut} does, ideally, reveal a plateau for $T_{\mathrm{cut}} \to T_{\mathrm{MC}}$. If a plateau does not emerge, we typically either find a maximum, or $\tau_{\mathrm{int}}^A(T_{\mathrm{cut}})$ is monotonously rising. If there is a maximum, we choose the corresponding value as best estimate of τ_{int}^A. Otherwise we reverse Sokal's proposal to choose T_{cut} larger than 4 to 6 times τ_{int}^A: we assume τ_{int}^A to lie in the interval defined by the intersections of the straight lines with slopes $T_{\mathrm{cut}}/4$ and $T_{\mathrm{cut}}/6$, respectively, with the curve $\tau_{\mathrm{int}}^A(T_{\mathrm{cut}})$.

Comparing autocorrelation times for runs with different lattice volumes it must be kept in mind

that the step size $N_{\mathrm{MD}}\delta t$ of the molecular dynamics update was not the same for all simulations; in fact it varied between 0.5 and 1.0 (see Table 3.1). At $(\beta, \kappa) = (5.6, 0.1575)$, however, the step size was the same for $L = 10, 12, 14$, so we can directly compare these runs and find, on the whole, only a weak increase of the autocorrelation times with increasing volume. More striking is the difference in the autocorrelation times between the simulations at $\beta = 5.6$ and $\beta = 5.32144$. At the latter value, which corresponds to a stronger gauge coupling, the relatively large autocorrelation times reflect the long-ranged statistical fluctuations that we observe in Figures B.7–B.10. These fluctuations are more severe on the smaller lattices where, moreover, zero modes of the Dirac matrix start playing a role. On the largest volume at this β the situation is somewhat better: While the autocorrelation times are comparable to those on the smaller volumes, we see no indication of exceptional configurations on the 16^3 lattice. (Note that from the first to the second line of the $(\beta, \kappa, L) = (5.32144, 0.1665, 16)$ entry in Table 3.4 $N_{\mathrm{MD}}\delta t$ has been halved.)

In order to determine empirically when equilibrium had been achieved we first of all looked at the time series of the plaquette and N_{iter} and noted when the initial transient appeared to end. We discarded approximately $T_{\mathrm{therm}} = 10\tau_{\mathrm{exp}}$ to $20\tau_{\mathrm{exp}}$ initial configurations, where we have conservatively chosen $\tau_{\mathrm{exp}} \equiv \tau_{\mathrm{exp}}^{N_{\mathrm{iter}}}$ because N_{iter} is closely related to the smallest eigenvalue of the Dirac matrix M, which is known to be among the slowest modes in the system (see *e.g.* [118]). Choosing the separation Δt two main aspects have been taken considered: On the one hand, estimates of τ_{int}^{A} for N_{iter} and the plaquette. These were based on autocorrelation studies at early stages of the simulations, however, when the statistical basis was still small and autocorrelation times were difficult to measure. The other aspect was the overall number of produced gauge configurations versus available computing time on the Cray T3E at Jülich, where the quark propagators and hadronic correlation functions were calculated.

3.3 Interpolating Operators

At the end of Section 1.3 we saw how the mass of a zero-momentum one-particle state can be extracted from the exponential decay of a suitable correlation function in Euclidean time. In the following we show how the left-hand side of Eq. 1.31 can be calculated on the lattice, so that we can obtain the particle mass from a fit of appropriate exponential functions to the lattice data.

In this work we investigate hadronic zero-momentum 2-point correlation functions of the form

$$\big\langle \mathcal{O}(\tau) J(0) \big\rangle \equiv \sum_{\mathbf{x}} \langle 0 | \mathcal{O}(\mathbf{x}, \tau) J(\mathbf{0}, 0) | 0 \rangle, \tag{3.8}$$

where the spatial Fourier integral of Eq. (1.31) has been replaced by a discrete sum over the spatial lattice sites and $\big\langle . \big\rangle$ is understood as the ensemble average. More specifically, for the source $J(x)$ and the sink $\mathcal{O}(x)$ we use the flavor non-singlet meson and baryon octet local interpolating fields ($x \equiv (\mathbf{x}, \tau)$)

$$P(x) = \overline{q}(x)\gamma_5 q(x) \qquad \text{(pseudo-scalar)} \tag{3.9a}$$

$$V_\mu(x) = \overline{q}(x)\gamma_\mu q(x) \qquad \text{(vector)} \tag{3.9b}$$

$$A_\mu(x) = \overline{q}(x)\gamma_5\gamma_\mu q(x) \qquad \text{(axial-vector)} \tag{3.9c}$$

$$N(x) = \epsilon_{abc}\big(q_a^T(x) C\gamma_5 q_b(x)\big) q_c(x) \qquad \text{(octet baryon)} \tag{3.9d}$$

where $C = \gamma_4\gamma_2$ is the usual charge conjugation matrix, and consider the following zero-momentum 2-point correlation functions $\langle\Gamma(\tau)\rangle \equiv \langle\mathcal{O}(\tau)J(0)\rangle$:

$$\langle\Gamma^P_\tau\rangle = \langle P^\dagger(\tau)P(0)\rangle \qquad \text{(pseudo-scalar)} \tag{3.10a}$$

$$\langle\Gamma^V_\tau\rangle = \langle V^\dagger_k(\tau)V_k(0)\rangle \qquad \text{(vector)} \tag{3.10b}$$

$$\langle\Gamma^N_\tau\rangle = \langle N(\tau)\overline{N}(0)\rangle \qquad \text{(octet baryon)} \tag{3.10c}$$

In addition we consider the following pseudoscalar correlators involving the fourth component of the axial current:

$$\langle\Gamma^A_\tau\rangle = \langle A^\dagger_4(\tau)A_4(0)\rangle \tag{3.11a}$$

$$\langle\Gamma^{AP}_\tau\rangle = \langle A^\dagger_4(\tau)P(0)\rangle \tag{3.11b}$$

$$\langle\Gamma^{PA}_\tau\rangle = \langle P^\dagger(\tau)A_4(0)\rangle \tag{3.11c}$$

Inserting the operators (3.9) into the correlators (3.10) and (3.11), performing all possible Wick-contractions (using the fact that the quark propagator is given by $\langle q(y)\overline{q}(x)\rangle \equiv M^{-1}(y,x)$) and projecting onto zero-momentum states we obtain *e.g.* the pseudo-scalar correlation function

$$\begin{aligned}\langle P^\dagger(\tau)P(0)\rangle &= \left\langle \sum_{\mathbf{x}} \mathrm{Tr}\left[\gamma_5 M^{-1}(\mathbf{0},0;\mathbf{x},\tau)\gamma_5 M^{-1}(\mathbf{x},\tau;\mathbf{0},0)\right]\right\rangle \\ &= \left\langle \sum_{\mathbf{x}} \mathrm{Tr}\left[\big(M^{-1}(\mathbf{x},\tau;\mathbf{0},0)\big)^\dagger M^{-1}(\mathbf{x},\tau;\mathbf{0},0)\right]\right\rangle,\end{aligned} \tag{3.12}$$

where the trace is over spin and color indices and the last equation is due to the relation

$$M^{-1}(y,x) = \gamma_5\big(M^{-1}(x,y)\big)^\dagger\gamma_5. \tag{3.13}$$

Similarly, the vector correlator reads

$$\begin{aligned}\langle V^\dagger_k(\tau)V_k(0)\rangle &= \left\langle \sum_{\mathbf{x}} \mathrm{Tr}\left[\gamma_k M^{-1}(\mathbf{0},0;\mathbf{x},\tau)\gamma_k M^{-1}(\mathbf{x},\tau;\mathbf{0},0)\right]\right\rangle \\ &= \left\langle \sum_{\mathbf{x}} \mathrm{Tr}\left[\big(M^{-1}(\mathbf{x},\tau;\mathbf{0},0)\big)^\dagger\gamma_5\gamma_k M^{-1}(\mathbf{x},\tau;\mathbf{0},0)\gamma_k\gamma_5\right]\right\rangle.\end{aligned} \tag{3.14}$$

All of the other mesonic 2-point functions are obtained analogously. For details on the calculation of the baryonic nucleon correlator see Refs. [12] or [119].

3.4 Wuppertal Smearing

In lattice simulations, operator smearing is essential for achieving ground state dominance before the signal is lost in the noisy large time limit. The smearing of the local operators (3.9), acting

as source and/or sink in Eq. (3.8), can be implemented by directly smearing the source and sink of the quark propagator M^{-1} (see *e.g.* Eq. (3.12)). To this end we employ the approximately Gaussian Wuppertal smearing [120] at the source only (ls) or at both source and sink (ss). We start with a point source[4], $\phi_0^{(0)}(\mathbf{x}) = \delta_{\mathbf{x}\mathbf{x}_0}$, at $\mathbf{x} = \mathbf{x}_0$ in timeslice $\tau = 0$, and apply the following iterative scheme to create a smeared source: Define $\phi_0^{(N)}(\mathbf{x}) \equiv \phi_0(\mathbf{x})$, and for $n = 0, 1, \ldots, N-1$ let

$$\phi_0^{(n+1)}(\mathbf{x}) = \frac{1}{1+6\alpha}\left[\phi_0^{(n)}(\mathbf{x}) + \alpha \sum_{k=1}^{3}\left(U_k(\mathbf{x},0)\phi_0^{(n)}(\mathbf{x}+\hat{\mathbf{k}}) + U_k^\dagger(\mathbf{x}-\hat{\mathbf{k}},0)\phi_0^{(n)}(\mathbf{x}-\hat{\mathbf{k}})\right)\right]. \tag{3.15}$$

The initial point source is thus smeared by N times adding to each lattice site the respective contributions from its six spatial neighbors with relative weight α, in a gauge invariant way.

We then solve

$$\sum_{\mathbf{y},\tau} M(\mathbf{x},0;\mathbf{y},\tau)S(\mathbf{y},\tau) = \phi_0(\mathbf{x}) \tag{3.16}$$

for S, where M is the Wilson quark matrix of Eq. (1.46), to obtain the "local-smeared" propagator

$$S(\mathbf{y},\tau) = \sum_{\mathbf{x}} M^{-1}(\mathbf{y},\tau;\mathbf{x},0)\phi_0(\mathbf{x}) \tag{3.17}$$

describing the propagation from a smeared source in timeslice 0 to the sink in timeslice τ. To obtain the fully smeared propagator, $S_\tau^{(N)}(\mathbf{y})$, we set $S_\tau^{(0)}(\mathbf{y}) \equiv S(\mathbf{y},\tau)$ and apply the smearing procedure for $n = 0, 1, \ldots, N-1$ again:

$$S_\tau^{(n+1)}(\mathbf{y}) = \frac{1}{1+6\alpha}\left[S_\tau^{(n)}(\mathbf{y}) + \alpha \sum_{k=1}^{3}\left(U_k(\mathbf{y},\tau)S_\tau^{(n)}(\mathbf{y}+\hat{\mathbf{k}}) + U_k^\dagger(\mathbf{y}-\hat{\mathbf{k}},\tau)S_\tau^{(n)}(\mathbf{y}-\hat{\mathbf{k}})\right)\right]. \tag{3.18}$$

The pseudoscalar 2-point function, for instance, with a local sink and a smeared source is then calculated via

$$\left\langle P^\dagger(\tau)P(0)\right\rangle^{ls} = \left\langle \sum_{\mathbf{y}} \mathrm{Tr}\left[\left(S_\tau^{(0)}(\mathbf{y})\right)^\dagger S_\tau^{(0)}(\mathbf{y})\right]\right\rangle, \tag{3.19}$$

while the smeared-smeared correlator is obtained from

$$\left\langle P^\dagger(\tau)P(0)\right\rangle^{ss} = \left\langle \sum_{\mathbf{y}} \mathrm{Tr}\left[\left(S_\tau^{(N)}(\mathbf{y})\right)^\dagger S_\tau^{(N)}(\mathbf{y})\right]\right\rangle. \tag{3.20}$$

The trace is again over spin and color indices. Other ls or ss correlation functions can be calculated analogously.

In all SESAM/TχL simulations, $N = 50$ smearing steps were used with a weight $\alpha = 4.0$. These parameters were originally optimized for the 16^3 SESAM lattice and then adopted for the larger 24^3 TχL lattice, too. In order to adapt these parameters to the smaller lattices considered in

[4]Spin and color indices are suppressed. The described procedure is carried out separately for each of the 4×3 independent spin-color components of ϕ_0.

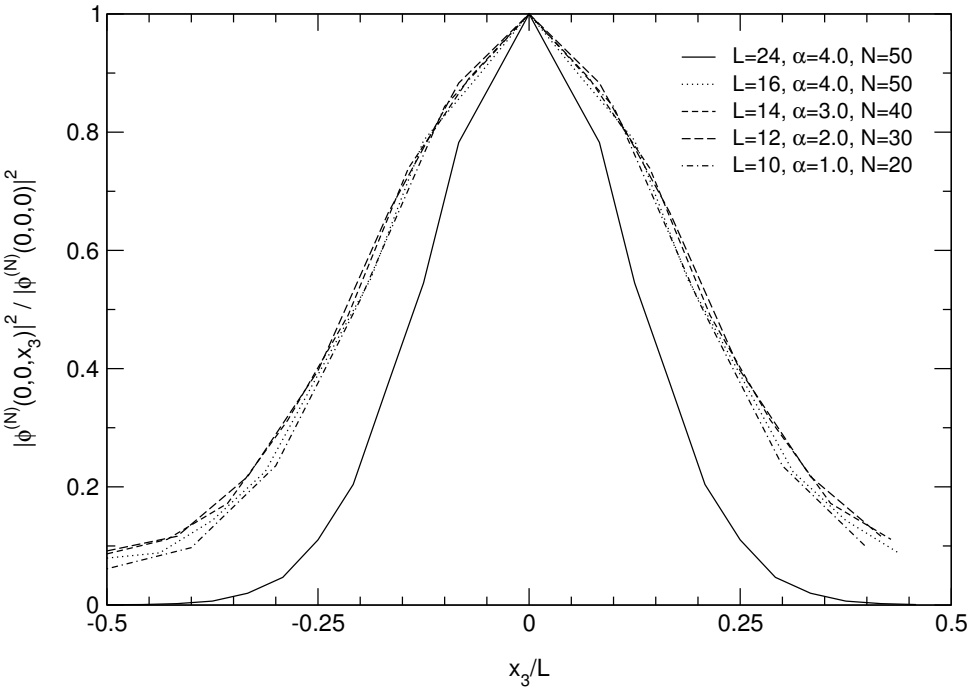

Figure 3.1: The parameters N, α for the Wuppertal smearing scheme were chosen such as to yield approximately the same wave function shapes for both the smaller lattices and the SESAM lattice ($L = 16$).

this work we have investigated the effect of smearing on the various volumes. We applied the smearing procedure described above to point sources $\phi^{(0)}(\mathbf{x})$ of size L^3 with $L = 24, 16, 14, 12, 10$. We set $\phi^{(0)}(\mathbf{x}) \equiv 0$ except for the point at $(L/2, L/2, L/2)$, which we conveniently define as the origin of the respective lattice and where we set $\phi^{(0)}(\mathbf{0}) = 1$. [5] Applying the smearing procedure (3.15) to $\phi^{(0)}$ with all $U_\mu(\mathbf{x}) \equiv 1$ we plot the amplitude of the "wave function" $\phi^{(N)}$ along the $(0, 0, 1)$-direction relative to its maximum at the origin, *i.e.* $|\phi^{(N)}(0, 0, x_3)|^2/|\phi^{(N)}(\mathbf{0})|^2$, versus x_3/L, for various values of N and α. The x_3-direction has been chosen arbitrarily. On inspection of the resulting wave function shapes we select the parameters N and α for our simulated volumes so as to make the the respective wave function profile look approximately like the SESAM one. The selected smearing parameters are listed in Table 3.5, while the corresponding wave function profiles are displayed in Fig. 3.1.

L	10	12	14	16	24
α	1.0	2.0	3.0	4.0	4.0
N	20	30	40	50	50

Table 3.5: Smearing parameters.

[5] Again, this is done for every spin-color degree of freedom of ϕ.

3.5 Quark Propagators

The smeared quark propagators (3.17) and hadronic 2-point functions (ls and ss) have been computed on the Cray T3E at the John von Neumann Institute for Computing (NIC) in Jülich. For the flavor non-singlet correlators considered here it is sufficient to calculate just one column of the quark propagator for a given source vector (see Eq. (3.17)), corresponding to the propagation from this source to all other lattice sites.

Calculating the quark propagator for a given gauge field configuration from the Wilson quark matrix M, the quark mass parameter κ in M does not need to be identical to the κ-value that was used in the generation of the underlying gauge field. We refer to the former as the "valence" quark mass parameter, $\kappa_{\rm val}$, and to the latter as the "sea" quark mass parameter, $\kappa_{\rm sea}$.[6] Varying $\kappa_{\rm val}$ for fixed $\kappa_{\rm sea} \neq 0$ is known as the *partially quenched approximation*; as it is computationally less demanding to reduce $\kappa_{\rm val}$ this approximation is often used to extrapolate lattice QCD results to physical (valence) quark masses. We have calculated ls and ss quark propagators and hadronic 2-point functions for the $\kappa_{\rm sea}$-$\kappa_{\rm val}$ combinations listed in Table 3.6. In this work we consider only the symmetric case, $\kappa_{\rm val} = \kappa_{\rm sea}$, while the other combinations are intended for future use.

3.6 Parameterization of the Two-Point Functions

For asymptotically large Euclidean times the 2-point functions (3.8) are dominated by the lowest mass state in the given channel, *i.e.*

$$\left\langle \mathcal{O}(\tau) J(0) \right\rangle \longrightarrow \frac{\langle 0 \left| \mathcal{O} \right| h \rangle \langle h \left| J \right| 0 \rangle}{2M} \, e^{-M\tau} \quad \text{for} \quad \tau \to \infty, \tag{3.21}$$

where $|h\rangle$ is the appropriate hadronic state with mass M that saturates the correlator at large τ. Calculating the quark propagator on a finite lattice, boundary conditions must be specified; we choose them to be periodic in the space directions and antiperiodic in time. For any given hadronic state this leads to an additional contribution from the corresponding anti-state propagating in the opposite direction. In case of a meson the antiparticle is degenerate in mass, so that we can average the lattice results for the 2-point function at τ and $T - \tau$ and account for the antiparticle's effect by choosing the parameterization

$$f_\tau(C, M) = C \left(e^{-M\tau} + e^{-M(T-\tau)} \right), \tag{3.22}$$

where M corresponds to the (anti-)particle mass and $C \sim \langle 0 \left| \mathcal{O} \right| h \rangle \langle h \left| J \right| 0 \rangle / 2M$ to the amplitude. In particular, the pseudoscalar and vector meson masses are obtained from fits of the local-smeared and smeared-smeared pseudoscalar and vector lattice correlators, $\left\langle P^\dagger(\tau) P(0) \right\rangle^{ls}$, $\left\langle P^\dagger(\tau) P(0) \right\rangle^{ss}$ and $\left\langle V_k^\dagger(\tau) V_k(0) \right\rangle^{ls}$, $\left\langle V_k^\dagger(\tau) V_k(0) \right\rangle^{ss}$, to the function (3.22).

In case of the nucleon we anti-symmetrize the correlator at τ and $T - \tau$. The backwards propagating negative parity partner N^* of the nucleon is an excited state with higher mass, so that its contribution is exponentially suppressed. The nucleon mass is therefore obtained from fits of

[6] Valence quarks are those which appear in external states, while sea quarks are those which appear in dynamical loops.

β	κ_{sea}	L^3T	$\kappa_{\text{val}}^{(1)}$	$\kappa_{\text{val}}^{(2)}$	$\kappa_{\text{val}}^{(3)}$	$\kappa_{\text{val}}^{(4)}$	$\kappa_{\text{val}}^{(5)}$	$\kappa_{\text{val}}^{(6)}$
5.32144	0.1665	$12^3 32$ $14^3 32$ $16^3 32$	0.1660	0.1662	**0.1665**	0.1667	0.1670	-
5.5	0.1580	$16^3 32$	**0.1580**	0.1590	0.1596	0.1600	0.1604	-
	0.1590	$16^3 32$	0.1580	**0.1590**	0.1596	0.1600	0.1604	-
	0.1596	$16^3 32$	0.1580	0.1590	**0.1596**	0.1600	0.1604	-
	0.1600	$16^3 32$	0.1580	0.1590	0.1596	**0.1600**	0.1604	-
5.6	0.1560	$16^3 32$	**0.1560**	0.1570	0.1575	0.1580	0.1585	-
	0.1565	$16^3 32$	0.1560	**0.1565**	0.1570	0.1575	0.1580	-
	0.1570	$16^3 32$	0.1555	0.1560	0.1565	**0.1570**	0.1575	-
	0.1575	$10^3 32$	0.1555	0.1560	0.1565	0.1570	**0.1575**	0.1580
		$12^3 32$	0.1555	0.1560	0.1565	0.1570	**0.1575**	0.1580
		$14^3 32$	0.1555	0.1560	0.1565	0.1570	**0.1575**	0.1580
		$16^3 32$	0.1555	0.1565	0.1570	**0.1575**	-	-
		$24^3 40$	0.1555	0.1560	0.1565	0.1570	**0.1575**	0.1580
	0.1580	$12^3 32$ $14^3 32$ $16^3 32$ $24^3 40$	0.1555	0.1560	0.1565	0.1570	0.1575	**0.1580**

Table 3.6: Combinations of κ_{sea} and κ_{val} for which quark propagators and hadronic 2-point functions have been computed.

the local-smeared and smeared-smeared lattice correlators $\left\langle N(\tau)\overline{N}(0)\right\rangle^{ls}$, $\left\langle N(\tau)\overline{N}(0)\right\rangle^{ss}$ to the single exponential

$$f_\tau(C, M) = Ce^{-M\tau}. \tag{3.23}$$

A useful parameter to control the contribution of excited states to the observed signal is the effective mass M_{eff}, which for mesonic states is computed iteratively from the implicit equation

$$\frac{\left\langle \mathcal{O}(\tau)J(0)\right\rangle}{\left\langle \mathcal{O}(\tau+1)J(0)\right\rangle} = \frac{e^{-\tau M_{\text{eff}}(\tau)} + e^{-(T-\tau)M_{\text{eff}}(\tau)}}{e^{-(\tau+1)M_{\text{eff}}(\tau)} + e^{-(T-\tau-1)M_{\text{eff}}(\tau)}}. \tag{3.24}$$

For the nucleon it is simply defined as the logarithmic derivative

$$M_{\text{eff}}(\tau) = \log \frac{\left\langle \mathcal{O}(\tau)J(0)\right\rangle}{\left\langle \mathcal{O}(\tau+1)J(0)\right\rangle}. \tag{3.25}$$

The effective mass is a measure for the local exponential decay of the correlator; for $\tau \to \infty$ it is expected to converge to the ground state mass M. The onset of a plateau in $M_{\text{eff}}(\tau)$ thus represents an important criterion for the choice of a lower boundary for the fitted time interval.

In the following we will denote the pseudoscalar mass and amplitude from a fit of $\left\langle P^\dagger(\tau)P(0)\right\rangle^{ls}$ to (3.22) by M_P^{ls} and C_P^{ls}, those from a fit of $\left\langle A_4^\dagger(\tau)P(0)\right\rangle^{ss}$ by M_{AP}^{ss} and C_{AP}^{ss}, and so on.

Amplitudes for local source and sink (ll) can generally be obtained from ls and ss amplitudes according to the factorization formula

$$C^{ll} = \frac{(C^{ls})^2}{C^{ss}}. \tag{3.26}$$

The definition of the pseudoscalar decay constant on the lattice is (for $\mathbf{p} = \mathbf{0}$)

$$Z_A \langle 0 | A_4 | \mathrm{PS} \rangle = M_{\mathrm{PS}} F_{\mathrm{PS}}, \tag{3.27}$$

where Z_A is a renormalization constant. Using Eq. (3.26) and the asymptotic relation (3.21), the unrenormalized decay constant can *e.g.* be obtained from

$$\frac{F_{\mathrm{PS}}}{Z_A} = \sqrt{\frac{2C_A^{ll}}{M_{\mathrm{PS}}}} = C_A^{ls} \sqrt{\frac{2}{M_{\mathrm{PS}} C_A^{ss}}}, \tag{3.28}$$

where the pseudoscalar mass $M_{\mathrm{PS}} = M_P^{ss}$ is taken from a fit of $\left\langle P^\dagger(\tau) P(0) \right\rangle^{ss}$. Alternatively it can be calculated from *e.g.*

$$\frac{F_{\mathrm{PS}}}{Z_A} = \frac{1}{2} \left[\frac{C_{AP}^{ls}}{2} \left(\frac{1}{\sqrt{C_P^{ss}}} + \frac{\sqrt{C_A^{ss}}}{C_{AP}^{ss}} \right) + \frac{C_A^{ls}}{2} \left(\frac{1}{\sqrt{C_A^{ss}}} + \frac{\sqrt{C_P^{ss}}}{C_{AP}^{ss}} \right) \right] \sqrt{\frac{2}{M_{\mathrm{PS}}}}, \tag{3.29}$$

where this time the pion mass M_{PS} is taken to be the average

$$M_{\mathrm{PS}} = \frac{1}{6} \left(M_P^{ss} + M_A^{ss} + M_{AP}^{ss} + M_A^{ls} + M_{AP}^{ls} + M_{PA}^{ls} \right). \tag{3.30}$$

Another quantity that can be obtained from pseudoscalar correlation functions is the quark mass as defined via the PCAC relation on the lattice,

$$a m_q = -\frac{M_{\mathrm{PS}}}{2} \frac{Z_A}{Z_P} \frac{\langle 0 | A_4 | \mathrm{PS} \rangle}{\langle 0 | P | \mathrm{PS} \rangle}. \tag{3.31}$$

In practice we calculate the unrenormalized quark mass according to

$$Z_q a m_q = \frac{M_{\mathrm{PS}}}{2} \sqrt{\frac{C_A^{ll}}{C_P^{ll}}} = \frac{M_{\mathrm{PS}}}{2} \frac{C_A^{ls}}{C_P^{ls}} \sqrt{\frac{C_P^{ss}}{C_A^{ss}}}, \tag{3.32}$$

where the renormalization constant is defined as $Z_q \equiv Z_P / Z_A$ and the pseudoscalar mass is obtained from

$$M_{\mathrm{PS}} = \frac{1}{4} \left(M_P^{ls} + M_P^{ss} + M_A^{ls} + M_A^{ss} \right). \tag{3.33}$$

3.7 Fitting Procedure

Let $N \equiv N_{\mathrm{conf}}$ be the number of gauge configurations selected from a MC time-series for which we calculate the quark propagator M^{-1} (see Section 3.1). On every configuration U_n, $n = 1, \ldots, N$, we compute the desired local-smeared and smeared-smeared hadronic 2-point functions

$$\Gamma_{\tau n} = \sum_{\mathbf{x}} \mathcal{O}(\mathbf{x}, \tau) J(\mathbf{0}, 0) \big|_{U_n}, \quad \tau = 1, \ldots, T, \tag{3.34}$$

where in each time-slice we sum over the space-like coordinates to project onto the zero-momentum state. The correlator $\langle\Gamma_\tau\rangle \equiv \langle\mathcal{O}(\tau)J(0)\rangle$ is then the ensemble average over the individual time-slices,

$$\langle\Gamma_\tau\rangle = \frac{1}{N}\sum_{n=1}^{N}\Gamma_{\tau n}, \quad \tau = 1,\ldots,T. \tag{3.35}$$

In order to obtain the mass M and amplitude C of a hadronic state we fit the averaged correlator $\langle\Gamma_\tau\rangle$ in the range $[\tau_{\min},\tau_{\max}]$ to the function

$$f_\tau(C,M) = \begin{cases} C\left(e^{-M\tau}+e^{-M(T-\tau)}\right) & \text{for mesons, and} \\ Ce^{-M\tau} & \text{for baryons} \end{cases} \tag{3.36}$$

by minimizing the χ^2-function

$$\chi^2 = \sum_{\tau,\tau'=\tau_{\min}}^{\tau_{\max}} \big(\langle\Gamma_\tau\rangle - f_\tau(C,M)\big)\Omega^{-1}_{\tau\tau'}\big(\langle\Gamma_{\tau'}\rangle - f_{\tau'}(C,M)\big), \tag{3.37}$$

where the covariance matrix

$$\Omega_{\tau\tau'} = \frac{1}{N(N-1)}\sum_{n=1}^{N}\big(\Gamma_{\tau n}-\langle\Gamma_\tau\rangle\big)\big(\Gamma_{\tau' n}-\langle\Gamma_{\tau'}\rangle\big) \tag{3.38}$$

characterizes the correlations between the time-slices. The minimization itself is done with the MINUIT package [122] from the CERN library [123]. In order to estimate the errors in the fit parameters C, M we use the jackknife method described in the next section.

3.8 Error Analysis

Let us consider a sample of N measurements of a primary quantity X ($N = N_{\text{conf}}$ and $X = \Gamma_\tau$, say). From the original sample $X_1, X_2, \ldots, X_N$ we create $N_b = N/b$ subsamples with $N-b$ elements each, where the k-th subsample is obtained from the original sample by leaving out the b elements (*block*) $X_{(k-1)b+1},\ldots,X_{kb}$. Then, if the k-th block average is given by

$$\langle X\rangle_{B(k)} = \frac{1}{b}\sum_{i=1}^{b} X_{(k-1)b+i}, \qquad k = 1,\ldots,N_b, \tag{3.39}$$

the average of the k-th subsample is

$$\langle X\rangle_{(k)} = \frac{N\langle X\rangle - b\langle X\rangle_{B(k)}}{N-b}, \qquad k = 1,\ldots,N_b. \tag{3.40}$$

The average of the re-sampled statistics,

$$\langle X\rangle = \frac{1}{N_b}\sum_{k=1}^{N_b}\langle X\rangle_{(k)} = \frac{1}{N}\sum_{i=1}^{N} X_i, \tag{3.41}$$

is identical to the usual sample mean that serves as an estimate of the true population mean μ. The variance of the resampled statistics with blocksize b is defined as

$$S_b^2/N = \frac{N_b - 1}{N_b} \sum_{k=1}^{N_b} \Big(\langle X \rangle_{(k)} - \langle X \rangle \Big)^2 \tag{3.42}$$

and agrees with the usual sample mean for $b = 1$:

$$S_1^2/N = \frac{N-1}{N} \sum_{k=1}^{N} \Big(\langle X \rangle_{(k)} - \langle X \rangle \Big)^2 = \frac{1}{N(N-1)} \sum_{i=1}^{N} (X_i - \langle X \rangle)^2 = S^2/N. \tag{3.43}$$

If the sample elements are statistically independent, S_1^2/N is a good estimate of the true variance σ^2/N. If, on the other hand, the data are correlated, then the true variance σ^2 is given by (see Section 3.2)

$$\sigma^2 \approx 2\tau_{\mathrm{int}}^X S_1^2. \tag{3.44}$$

The correlation between the sample elements can be eliminated by choosing the blocksize b large enough ($b \gg \tau_{\mathrm{int}}^X$) such that $S_b^2 \to \sigma^2$. An appropriate blocksize b may be found self-consistently without any prior knowledge of τ_{int} by plotting the b-dependence of S_b^2 (or S_b) and observing where it becomes independent of b. In this way one can even obtain an estimate of the autocorrelation time τ_{int}^X using the relation[7]

$$2\tau_{\mathrm{int}}^X \approx \frac{S_b^2}{S_1^2} \quad \text{for } b \text{ large.} \tag{3.45}$$

Suppose now we want to estimate the mean and error of a secondary quantity y, *i.e.* of a function of the primary quantity X (the parameters C and M from a fit to a correlator, say). The best estimate of a secondary quantity is $\langle y \rangle = y(\langle X \rangle)$, not $\langle y(X) \rangle$. A robust error estimate for $\langle y \rangle$ can be obtained by calculating y on the N_b subsample means (3.40), yielding the jackknife estimators

$$y_{(k)} = y(\langle X \rangle_{(k)}), \qquad k = 1, \ldots, N_b, \tag{3.46}$$

with an average

$$\langle y \rangle = \frac{1}{N_b} \sum_{k=1}^{N_b} y_{(k)}. \tag{3.47}$$

The variance of the jackknife estimators is obtained in analogy to (3.42) from

$$S_b^2/N = \frac{N_b - 1}{N_b} \sum_{k=1}^{N_b} \big(y_{(k)} - \langle y \rangle \big)^2 . \tag{3.48}$$

For large enough b we take $S_b/\sqrt{N}$ as an estimate of the standard error $\sigma/\sqrt{N}$ of $\langle y \rangle$.

[7] This is usually a "remnant" autocorrelation time in the sense that the considered sample elements (actually configurations) are already separated by a number of HMC trajectories. To obtain the "full" autocorrelation time, τ_{int}^X has to be multiplied by this separation, ΔN_{conf} (see Section 3.1).

Chapter 4

Light Hadron Spectroscopy

In this chapter we present the main results of this work. We will describe in detail how we have obtained the light hadron masses by fitting the corresponding mesonic and baryonic two-point functions to the parameterizations introduced in the previous chapter. The resulting masses (before chiral or continuum extrapolation) of the pseudoscalar (pion) and vector (rho) mesons and of the nucleon are given. We also present results for the (unrenormalized) pseudoscalar decay constant and the bare PCAC quark mass. The Sommer parameter r_0 is used to set the physical scale. After a discussion of the role of spatial Polyakov-type loops in finite volume we will examine various "naive" parameterizations of the finite-size mass shifts motivated by Lüscher's formula and the observations made by Fukugita *et al.*. We will then check on the validity of available theoretical formulae from effective field theory in the parameter regime covered by our simulations. The issue of infinite-volume extrapolations will be discussed. Finally we will exploit the volume-independence of the PCAC quark mass to check on the importance of discretization errors in our simulations.

4.1 Static Quark Potential

We calculate the static quark potential in order to determine the Sommer scale [74] that we use to set the scale in our simulations. For the SESAM/TχL simulations at $\beta = 5.5$ and $\beta = 5.6$ the Sommer radii $R_0 \equiv r_0/a$ as listed in Table 4.1 have been determined by G. Bali; they have previously been published in Refs. [124] and [125], respectively. Since the lattice-size dependence of R_0 is assumed to be small and as we want to have a common length scale for the different simulated lattice volumes at fixed gauge coupling and quark mass, we adopt the R_0-value from the largest available lattice, respectively, also for the smaller ones.

In order to determine the Sommer radius for the 16^3 lattice at $(\beta, \kappa) = (5.32144, 0.1665)$ we measure the Wilson loops $W(R, \tau)$ with temporal extents of up to $\tau = 8$ and spatial separations of up to $R = \sqrt{3} \cdot 7 \approx 12$ lattice units on the same configurations that we use for spectroscopy. We employ the modified Bresenham algorithm of Ref. [126] to include all possible lattice vectors $\mathbf{R}$ to a given separation $R \equiv |\mathbf{R}|$. Using the spatial APE smearing as described in Ref. [127], we apply

$$\text{link} \rightarrow \alpha \times \text{link} + \text{staples} \tag{4.1}$$

to the gauge links of each configuration before actually calculating the Wilson loops. We use $\alpha = 2.3$ and perform $N = 26$ iterations, followed by a projection back into the gauge group [128].

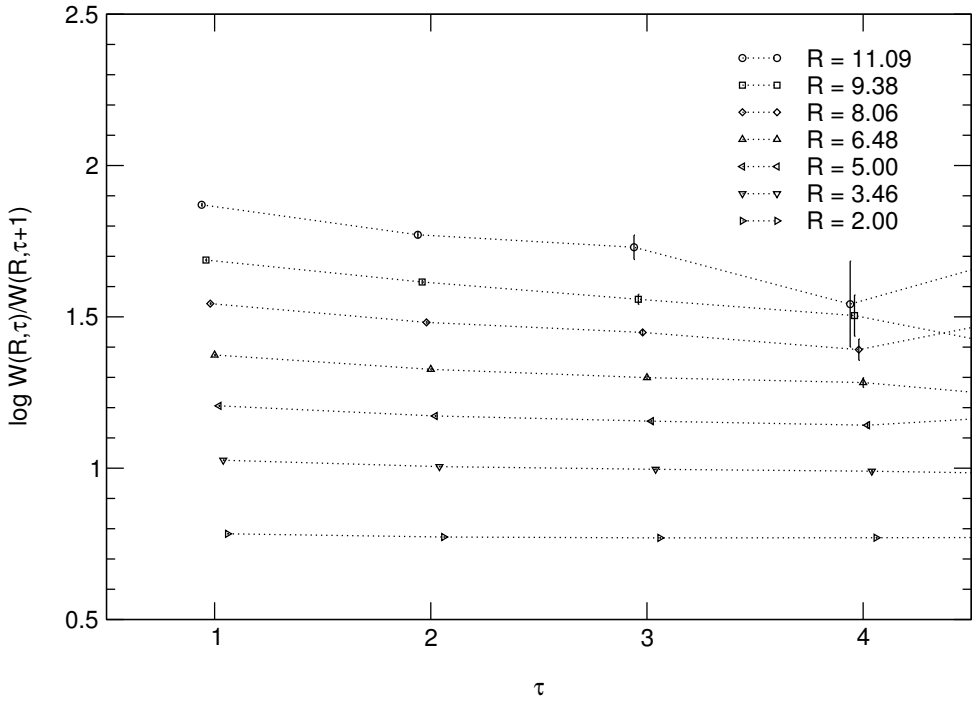

Figure 4.1: The effective potential, V_{eff}, at $(\beta, \kappa) = (5.32144, 0.1665)$ on the 16^3 lattice, for selected values of R in the range $\tau = 1, \ldots, 4$. Larger values of τ are dominated by statistical noise.

The asymptotic behavior of the static potential $V(R)$ for sufficiently large times τ is given by

$$W(R, \tau) \sim C(R)\, e^{-V(R)\tau}, \tag{4.2}$$

so that one can define an effective "local" potential

$$V_{\text{eff}}(R, \tau) = \ln \frac{W(R, \tau)}{W(R, \tau + 1)}. \tag{4.3}$$

Figure 4.1 shows the τ-dependence of the effective potential $V_{\text{eff}}(R, \tau)$ for various values of R. At $\tau = 3$ the effective potential is already largely independent of τ while the statistical errors are moderate, so that we determine $V(R)$ from a single exponential fit in the range $[\tau_{\min}, \tau_{\max}] = [3, 4]$.[1] As can be seen from Figure 4.2, the resulting values for $V(R)$ show the expected behavior. We observe no indication of string breaking and therefore fit the data in the range $[R_{\min}, R_{\max}] = [2.5, 8]$ to

$$V(R) = V_0 - \frac{e}{R} + \sigma R. \tag{4.4}$$

The upper boundary of the fitted range has been set to $R_{\max} = 8$ because up to this value the data correspond nicely to the expected linear behavior, with small statistical errors. With $R_{\max}$ held fixed the lower boundary has been determined by investigating the $R_{\min}$-dependence of r_0 for various values $R_{\min} \gtrsim 2$. (Below this value we observe a violation of rotational symmetry due to the finite lattice spacing.) From the fit we obtain the following parameters for the potential

[1] The quality of the statistical signal does not allow to extend the upper boundary of the fitted range beyond $\tau_{\max} = 4$.

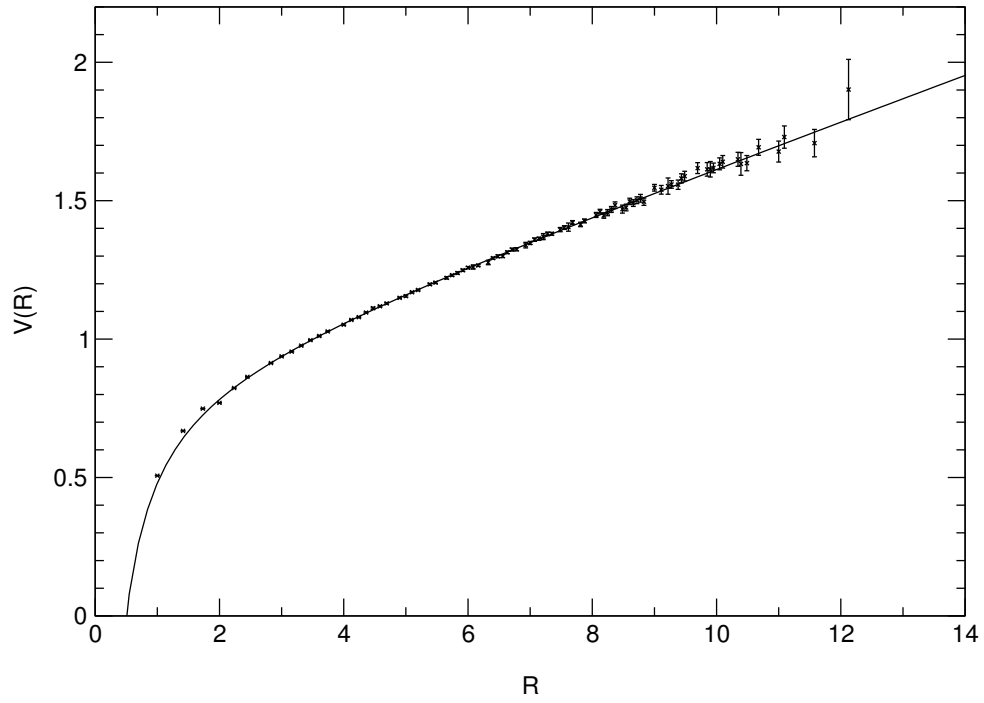

Figure 4.2: The static quark potential obtained from Wilson loops at $(\beta, \kappa) = (5.32144, 0.1665)$ on the 16^3 lattice.

(in lattice units):

$$V_0 = 0.8378(87), \quad e = 0.440(18), \quad \sigma = 0.08187(97). \tag{4.5}$$

The Sommer scale R_0, which is defined through the force between two static quarks at some intermediate distance,

$$R^2 \left.\frac{dV}{dR}\right|_{R=R_0} = 1.65, \tag{4.6}$$

is obtained from these parameters according to

$$R_0 = \sqrt{\frac{1.65 - e}{\sigma}}. \tag{4.7}$$

Our result for the simulation at $(\beta, \kappa, L) = (5.32144, 0.1665, 16)$ is given in Table 4.1. The quoted uncertainty corresponds to the statistical error.

In various nonrelativistic potential models the definition (4.6) consistently amounts to a physical value of $r_0 = 0.5\,\mathrm{fm}$ [74]. We use this value to set the scale in our simulations. The resulting physical values for the momentum cut-off a^{-1}, the lattice spacing a and the box size La are displayed in Table 4.1. As expected, the smallest simulated β of 5.32144 is associated with the largest lattice spacing (0.13 fm, corresponding to a relatively low momentum cut-off of 1.52 GeV). While we have to look out for potentially large $O(a)$ discretization errors at this coupling, the physical volume is the biggest of all simulated volumes. With a linear extension of slightly more than 2 fm it is comparable in size with the TχL lattice at $(\beta, \kappa) = (5.6, 0.1575)$.

β	κ_{sea}	L^3T	r_0/a	a^{-1} [GeV]	a [fm]	La [fm]
5.32144	0.1665	$16^3 32$	3.845(37)	1.517(15)	0.1300(13)	2.081(21)
5.5	0.1580	$16^3 32$	4.027(24)	1.5893(95)	0.12416(74)	1.987(12)
	0.1590	$16^3 32$	4.386(26)	1.731(11)	0.11400(68)	1.824(11)
	0.1596	$16^3 32$	4.675(34)	1.845(14)	0.10695(78)	1.711(13)
	0.1600	$16^3 32$	4.889(30)	1.929(12)	0.10227(63)	1.636(10)
5.6	0.1560	$16^3 32$	5.104(29)	2.014(12)	0.09796(56)	1.5674(89)
	0.1565	$16^3 32$	5.283(52)	2.085(21)	0.09464(93)	1.514(15)
	0.1570	$16^3 32$	5.475(72)	2.161(29)	0.0913(12)	1.461(20)
	0.1575	$16^3 32$	5.959(77)	2.352(31)	0.0839(11)	1.343(18)
		$24^3 40$	5.892(27)	2.325(11)	0.08486(39)	2.0367(94)
	0.1580	$24^3 40$	6.230(60)	2.459(24)	0.08026(78)	1.926(19)

Table 4.1: Sommer scale and resulting momentum cut-off, lattice spacing and lattice size for $r_0 = 0.5\,\text{fm}$.

4.2 Light Hadron Masses

As described in Section 3.6, hadron masses and decay constants can be obtained by fitting the simulated mesonic and baryonic two-point functions to the parameterizations (3.22) and (3.23), respectively. In doing so it is important to tune the fitted interval in such a way as to avoid systematic errors coming *e.g.* from excited state contributions at small Euclidean times. Therefore the lower boundary of the fitted range, τ_{min}, should correspond to the onset of the asymptotic region in which these contaminations can be neglected and the desired ground state dominates. The upper boundary τ_{max}, on the other hand, is normally kept fixed at $T/2$ for mesonic states. (Due to the symmetrization of the mesonic correlators at τ and $T-\tau$ an upper boundary $\tau_{\text{max}} > T/2$ does not lead to any further improvement.) In case of the nucleon we choose $\tau_{\text{max}} = T/2 - 1$ by default in order to avoid potential contaminations coming from the backwards propagating anti-particle. Both in the mesonic and the baryonic case it may happen, however, that due to statistical fluctuations and hence large error bars the correlator at large τ is compatible with zero. In such cases we sometimes have to shift τ_{max} to smaller values of τ in order to avoid potential systematic errors from this source.

In practice we consider three different criteria to find the optimal fit interval for a given correlator. First we examine a plot of the effective mass M_{eff} as defined by (3.24) for mesons and (3.25) for the nucleon. Since M_{eff} is a measure for the local exponential decay of the 2-point function, a plateau is expected to emerge when ground state dominance is reached. The convergence to the asymptotic mass value can be from above or from below depending on the choice of the interpolating source and sink operators J and $\mathcal{O}$. Only for $\mathcal{O}^\dagger = J$ is the correlation function positive definite and the convergence is monotonic and from above. In this work this is the case for all the correlators used for the determination of the pseudoscalar and vector meson masses and the nucleon mass. The upper left plot in Figure 4.3 shows as an example the effective masses for the pseudoscalar correlator at $(\beta, \kappa, L) = (5.6, 0.158, 16)$. The contribution of excited states is most obvious at small τ where M_{eff} decreases rapidly before flattening out. In the flat plateau region one assumes that, within the numerical precision, only the lowest mass contribution is significant. In case of a finite statistical sample, however, correlated statistical fluctuations occur

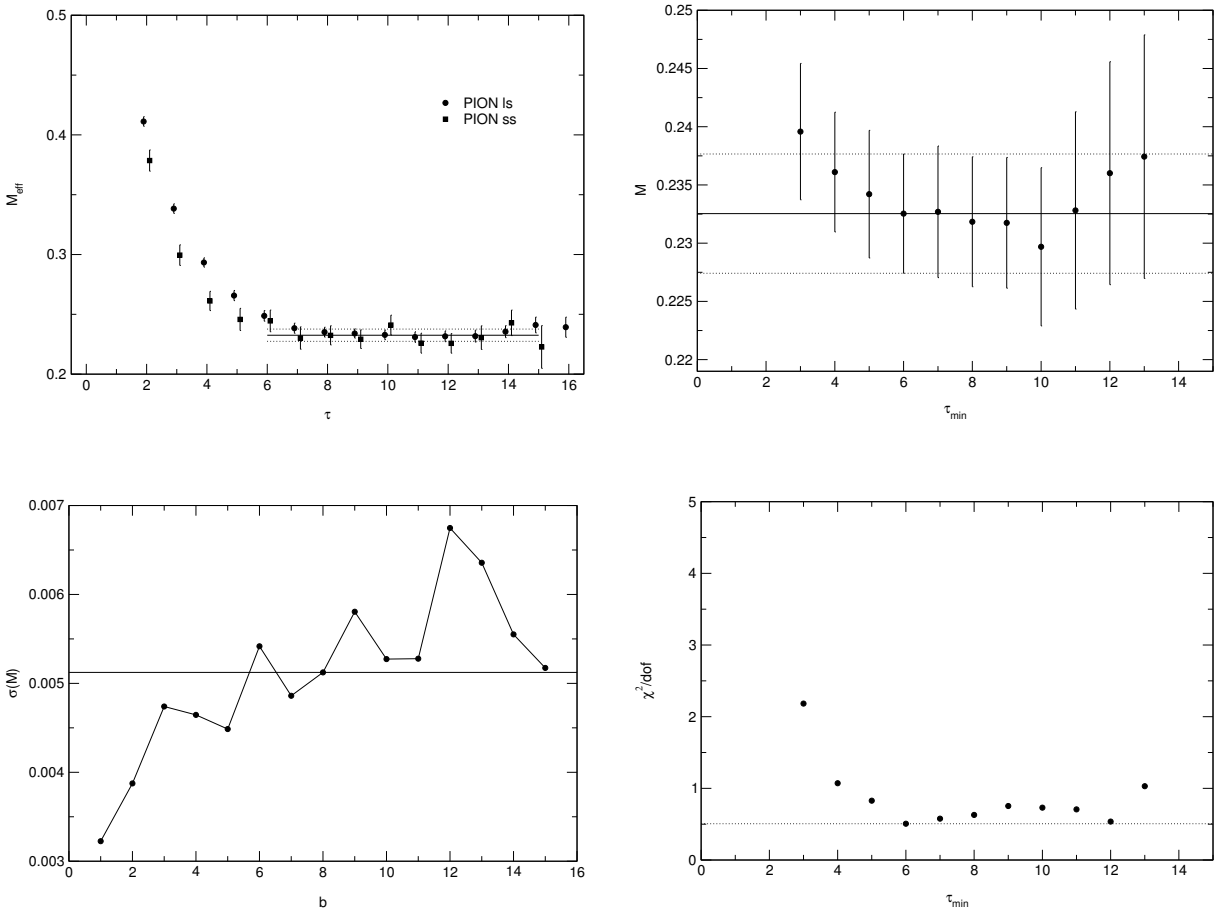

Figure 4.3: Plots used for the determination of the optimal τ-intervals in the correlator fits (here for $\left\langle P^\dagger(\tau)P(0)\right\rangle^{ss}$ at $(\beta,\kappa,L)=(5.6,0.158,16)$). The plots show, clockwise, the effective mass $M_{\text{eff}}(\tau)$, the fit result M and the χ^2/dof-value of the fit versus τ_{min}, and the standard error of M versus the jackknife blocksize b. The horizontal lines indicate the fit result, the goodness of fit and the standard error of the result, respectively, for the chosen τ-interval (here $[6,15]$) and blocksize (here $b=8$). In the upper left graph we also plot, for comparison, the effective mass from the local-smeared correlator $\left\langle P^\dagger(\tau)P(0)\right\rangle^{ls}$.

				$\langle P^\dagger(\tau)P(0)\rangle^{ss}$		$\langle V_k^\dagger(\tau)V_k(0)\rangle^{ss}$		$\langle N(\tau)\overline{N}(0)\rangle^{ss}$	
β	κ_{sea}	L^3T	b	$[\tau_{\min},\tau_{\max}]$	χ^2/df	$[\tau_{\min},\tau_{\max}]$	χ^2/df	$[\tau_{\min},\tau_{\max}]$	χ^2/df
5.32144	0.1665	$12^3 32$	7	4,14	0.89	6,14	0.88	4,12	0.57
		$14^3 32$	7	8,14	2.48	4,14	1.51	4,11	0.80
		$16^3 32$	7	3,15	1.16	3,15	1.36	3,14	1.34
5.5	0.1580	$16^3 32$	7	6,15	0.87	6,15	1.05	4,14	0.95
	0.1590	$16^3 32$	8	4,15	1.09	4,15	0.77	4,14	0.88
	0.1596	$16^3 32$	5	4,15	1.24	4,15	1.08	4,14	1.21
	0.1600	$16^3 32$	6	7,15	1.78	4,15	0.75	6,14	0.80
5.6	0.1560	$16^3 32$	5	4,15	0.43	4,15	0.59	4,14	0.60
	0.1565	$16^3 32$	7	11,15	1.96	7,15	1.56	7,14	0.85
	0.1570	$16^3 32$	7	4,15	0.45	6,15	0.50	6,14	0.91
	0.1575	$10^3 32$	9	6,15	1.90	12,15	0.79	6,14	0.72
		$12^3 32$	9	8,15	0.90	6,15	0.37	7,14	1.47
		$14^3 32$	6	8,15	1.42	8,15	0.41	5,14	0.58
		$16^3 32$	4	7,15	0.40	9,15	0.61	7,14	0.99
		$24^3 40$	7	7,19	0.81	7,19	1.31	7,18	0.40
	0.1580	$12^3 32$	3	6,15	1.07	6,15	1.31	5,14	0.94
		$14^3 32$	5	6,15	1.54	7,15	0.85	7,14	0.60
		$16^3 32$	8	6,15	0.51	10,15	1.72	4,14	0.34
		$24^3 40$	9	6,19	1.08	7,19	1.54	10,18	0.45

Table 4.2: Fit parameters for the fully smeared pseudoscalar, vector and nucleon correlators. b denotes the blocksize for the jackknife, $[\tau_{\min}, \tau_{\max}]$ is the fitted interval and χ^2/df indicates the fit quality.

also in the plateau region. The effective mass plot in Figure 4.3 demonstrates that the same asymptotic value is reached faster by the fully smeared correlation function than by the local-smeared correlator, which is usually reflected in smaller values for $\tau_{\min}$. While this is exactly the desired effect it comes at a prize, though, because the statistical fluctuations around the plateau mass and the error bars are in general larger in case of the fully smeared correlator. With the exception of the pseudoscalar correlator the statistical noise in the data generally grows with τ, until it may eventually dominate over the signal. This effect can also be controlled via the effective mass plot and accounted for by adapting $\tau_{\max}$ appropriately.

The second control parameter used to find a suitable $\tau_{\min}$ is the fit parameter M itself. Plotted against $\tau_{\min}$ (for fixed $\tau_{\max}$) it should, within the statistical uncertainty, show no bias with respect to the choice of $\tau_{\min}$. (Often, however, due to the statistical noise at large values of τ, a plateau can only be identified at intermediate values of $\tau_{\min}$.) Finally, the third criterion is supplied by the corresponding values of χ^2/dof which, ideally, should exhibit a distinctive minimum near 1.

Besides the boundaries of the fit interval we also tune the blocksize b for the jackknife as introduced in Section 3.8. Plotting the standard error $\sigma(M)$ versus b we look for a plateau indicating where the error becomes independent of the blocksize. Due to the fact that our samples are

β	$\kappa_{\rm sea}$	L^3T	$M_{\rm PS}L$	$M_{\rm PS}/M_{\rm V}$	$M_{\rm PS}$	$M_{\rm V}$	M_N
5.32144	0.1665	$12^3 32$	3.18(8)	0.521(23)	0.2648(67)	0.508(26)	0.788(26)
		$14^3 32$	3.6(1)	0.497(20)	0.2577(87)	0.518(12)	0.779(16)
		$16^3 32$	4.42(7)	0.552(11)	0.2760(42)	0.4999(78)	0.727(11)
5.5	0.1580	$16^3 32$	8.85(6)	0.8506(31)	0.5534(39)	0.6506(46)	1.026(18)
	0.1590	$16^3 32$	7.09(4)	0.8010(53)	0.4429(26)	0.5529(54)	0.8718(78)
	0.1596	$16^3 32$	5.89(4)	0.7512(51)	0.3682(27)	0.4902(52)	0.7640(75)
	0.1600	$16^3 32$	4.89(5)	0.6725(93)	0.3058(34)	0.4547(61)	0.703(10)
5.6	0.1560	$16^3 32$	7.15(4)	0.8330(16)	0.4469(23)	0.5365(36)	0.8533(62)
	0.1565	$16^3 32$	6.32(6)	0.7912(72)	0.3948(38)	0.4989(54)	0.785(10)
	0.1570	$16^3 32$	5.52(5)	0.7627(58)	0.3452(29)	0.4527(52)	0.7095(90)
	0.1575	$10^3 32$	4.92(6)	0.838(30)	0.4919(55)	0.587(20)	1.042(20)
		$12^3 32$	4.3(1)	0.724(11)	0.3576(89)	0.494(12)	0.817(16)
		$14^3 32$	4.27(6)	0.691(11)	0.3048(44)	0.4413(66)	0.719(16)
		$16^3 32$	4.49(6)	0.6952(99)	0.2806(35)	0.4036(68)	0.6254(89)
		$24^3 40$	6.64(6)	0.7010(62)	0.2765(26)	0.3944(38)	0.5920(75)
	0.1580	$12^3 32$	4.6(1)	0.722(20)	0.387(12)	0.535(17)	0.882(25)
		$14^3 32$	4.13(8)	0.630(13)	0.2949(60)	0.4677(90)	0.717(19)
		$16^3 32$	3.72(8)	0.627(21)	0.2325(51)	0.371(13)	0.622(12)
		$24^3 40$	4.78(8)	0.566(17)	0.1991(33)	0.3519(86)	0.500(12)

Table 4.3: Masses of the pseudoscalar and vector mesons and of the nucleon in lattice units.

finite, $\sigma(M)$ does of course show statistical fluctuation even when it does not display an overall tendency to rise with increasing b. In this case we assume that the elements of the chosen subsample are, at least with regard to the considered observable, statistically independent. If, on the other hand, we observe a significant initial increase of the error on top of the fluctuations and before saturation, we take this as a hint that the elements of the sub-sample are still correlated, meaning that the separation in MC time between the selected gauge configurations, Δt, has been chosen too small for the configurations to be truly independent. This remnant autocorrelation time is however eliminated by the blocked jackknife.

Figure 4.3 shows examples of the plots that we have used to determine the boundaries of the fit intervals, $\tau_{\rm min}$ and $\tau_{\rm max}$, and the blocksize b for the jackknife. The selected values for the fully smeared pseudoscalar, vector and nucleon 2-point functions are displayed in Table 4.2, together with the χ^2/dof-values the fits. The numbers for the corresponding ls correlation functions and for the pseudoscalar correlators (3.11) (ss and ls) are listed in Tables C.1–C.3 in Appendix C. Although *a priori* the onset of plateau formation is not independent of the considered correlator it has always been possible to find—at a given β, κ and L— a universal blocksize b such as to account for the errors of *all* the respective hadron masses together.

The masses (in lattice units) of the pseudoscalar and vector mesons and of the nucleon are given in Table 4.3. Having checked that the masses obtained from the local-smeared and the fully smeared correlators are consistent we only quote the values obtained from the latter here and

β	κ_{sea}	L^3T	La[fm]	$(r_0 m_{\text{PS}})^2$	m_{PS}[GeV]	m_{V}[GeV]	m_N[GeV]
5.32144	0.1665	$12^3 32$	1.56(2)	1.037(57)	0.402(11)	0.771(40)	1.195(42)
		$14^3 32$	1.82(2)	0.982(68)	0.391(14)	0.786(20)	1.182(26)
		$16^3 32$	2.08(2)	1.126(43)	0.4188(75)	0.759(14)	1.104(20)
5.5	0.1580	$16^3 32$	1.99(1)	4.97(20)	0.8795(81)	1.0340(95)	1.631(30)
	0.1590	$16^3 32$	1.82(1)	3.77(12)	0.7666(64)	0.957(11)	1.509(16)
	0.1596	$16^3 32$	1.71(1)	2.96(10)	0.6793(70)	0.904(12)	1.410(17)
	0.1600	$16^3 32$	1.64(1)	2.235(85)	0.5901(75)	0.877(13)	1.356(21)
5.6	0.1560	$16^3 32$	1.567(9)	5.20(18)	0.9002(69)	1.0807(94)	1.719(16)
	0.1565	$16^3 32$	1.51(1)	4.35(25)	0.823(11)	1.040(15)	1.637(27)
	0.1570	$16^3 32$	1.46(2)	3.57(21)	0.746(12)	0.978(17)	1.533(28)
	0.1575	$10^3 32$	0.849(4)	8.40(59)	1.144(14)	1.365(48)	2.424(47)
		$12^3 32$	1.018(5)	4.44(48)	0.832(21)	1.149(27)	1.901(38)
		$14^3 32$	1.188(5)	3.22(18)	0.709(11)	1.026(16)	1.671(39)
		$16^3 32$	1.358(6)	2.73(12)	0.6524(86)	0.938(16)	1.454(22)
		$24^3 40$	2.037(9)	2.654(90)	0.6429(67)	0.9171(98)	1.377(19)
	0.1580	$12^3 32$	0.963(9)	5.80(88)	0.951(30)	1.316(44)	2.167(66)
		$14^3 32$	1.12(1)	3.37(28)	0.725(16)	1.150(25)	1.763(50)
		$16^3 32$	1.28(1)	2.10(15)	0.572(14)	0.912(33)	1.530(32)
		$24^3 40$	1.93(2)	1.539(74)	0.4896(94)	0.865(23)	1.228(31)

Table 4.4: Masses of the pseudoscalar meson, the vector meson and the nucleon in physical units (using $r_0 = 0.5\,\text{fm}$).

in the following. The quoted errors are statistical in nature and of the order of one percent. Table 4.3 also shows $M_{\text{PS}}(L)L$, the linear box size in units of the pseudoscalar correlation length $1/M_{\text{PS}}(L)$, where $M_{\text{PS}}(L)$ is the pion mass in the given *finite* volume. It should be borne in mind that for sub-asymptotic volumes this value is in general different from $M_{\text{PS}}L$, where M_{PS} is the pseudoscalar mass in *infinite* volume. The ratios $M_{\text{PS}}/M_{\text{V}}$ are a measure of the simulated quark mass, respectively.[2] At $(\beta, \kappa) = (5.32144, 0.1665)$ we attain our lightest quark mass, with $M_{\text{PS}}/M_{\text{V}}$ being close to the vector meson decay threshold of $M_{\text{PS}}/M_{\text{V}} = 0.5$. Using $r_0 = 0.5\,\text{fm}$ to set the scale the hadron masses of Table 4.3 translate into the physical values listed in Table 4.4.[3] It shows also the physical box sizes La, where the lattice spacings a have been determined on the largest available lattice, respectively (see also Table 4.1). The dimensionless quantity

$$M_r = (r_0 m_{\text{PS}})^2 \tag{4.8}$$

[2]The physical value is $m_\pi/m_\rho = 0.178$.

[3]Although the Sommer scale is in general quark mass dependent we neglect this dependence here because we have only one quark mass at $\beta = 5.32144$ (and because we assume that the dependence is weak). The dimensionful quantities in Table 4.4 have been calculated using r_0 as obtained on the largest lattice for the respective quark mass, *i.e.* without chiral extrapolation. A chiral extrapolation might yield slightly larger values for r_0 than those given in Table 4.1. This would mean that quantities with the dimension of a length (a, La) are somewhat overestimated, whereas those with dimension of a mass (m_{PS}, m_{V}, m_N) are rather underestimated. See Ref. [98] for a recent discussion of the quark mass dependence of r_0.

β	κ_{sea}	L^3T	$F_{\text{PS}}^{(1)}/Z_A$	$F_{\text{PS}}^{(2)}/Z_A$	Z_qM_q
5.32144	0.1665	$12^3 32$	0.062(10)	0.058(15)	0.0106(33)
		$14^3 32$	0.0757(56)	0.0774(73)	0.0152(18)
		$16^3 32$	0.0843(62)	0.0771(44)	0.0155(12)
5.5	0.1580	$16^3 32$	0.1073(42)	0.1062(49)	0.0821(35)
	0.1590	$16^3 32$	0.0945(23)	0.0930(27)	0.0544(12)
	0.1596	$16^3 32$	0.0815(16)	0.0766(14)	0.03724(81)
	0.1600	$16^3 32$	0.0750(23)	0.0746(39)	0.0279(15)
5.6	0.1560	$16^3 32$	0.0843(19)	0.0823(21)	0.0620(11)
	0.1565	$16^3 32$	0.0805(18)	0.0757(20)	0.0467(15)
	0.1570	$16^3 32$	0.0726(16)	0.0704(18)	0.0391(15)
	0.1575	$10^3 32$	0.0284(30)	0.0256(37)	0.0209(32)
		$12^3 32$	0.0429(34)	0.0425(31)	0.0249(19)
		$14^3 32$	0.0566(30)	0.0559(44)	0.0261(22)
		$16^3 32$	0.0626(26)	0.0640(34)	0.0275(16)
		$24^3 40$	0.0646(18)	0.0623(19)	0.02680(68)
	0.1580	$12^3 32$	0.022(12)	0.016(10)	0.0113(88)
		$14^3 32$	0.0233(32)	0.0216(34)	0.0099(17)
		$16^3 32$	0.0469(26)	0.0456(34)	0.0141(11)
		$24^3 40$	0.0602(39)	0.0578(34)	0.0157(11)

Table 4.5: The pseudoscalar decay constant and the PCAC quark mass. $F_{\text{PS}}^{(1)}/Z_A$ has been obtained according to Eq. (3.29), $F_{\text{PS}}^{(2)}/Z_A$ according to Eq. (3.28).

is another measure of the quark mass, since for $m_q \to 0$ the pion mass behaves like $m_\pi \propto \sqrt{m_q}$ [78]. At the physical strange quark mass it gives $M_r \approx 3.1$. For those of our parameter sets where we have simulated several lattice volumes the value of M_r ranges between $M_r \approx 2.65$ and $M_r \approx 1.13$, corresponding to about 85 and 36% of the value for the strange quark mass.

Table 4.5 shows our lattice results for the unrenormalized pseudoscalar decay constant F_{PS}/Z_A as obtained in the two different ways introduced in Section 3.6. Within the statistical errors (of comparable size) the two methods yield consistent results. The normalization of the pseudoscalar decay constant is such that the physical value is $f_\pi = 92.4\,\text{MeV}$. The bare PCAC quark mass Z_qM_q, where $Z_q = Z_P/Z_A$ is the multiplicative renormalization factor, is given in the last column of Table 4.5.

4.3 Polyakov Loops

An investigation into finite-size effects requires data from a number of simulations with different lattice volumes, and with respect to the computational cost it is of course preferable to use rather small lattices. However, since we want do do spectroscopy in the hadronic zero-temperature phase of QCD, we should make sure that the lattices we investigate are not too small, because in

β	κ_{sea}	L^3T	$\langle \text{Re}\, P_z \rangle$	$\langle \text{Im}\, P_z \rangle$
5.32144	0.1665	$12^3 32$	-0.00056433(3)	-0.0003573(2)
		$14^3 32$	-0.0000179(2)	-0.00003209(4)
		$16^3 32$	0.00012251(3)	-0.00021856(4)
5.6	0.1575	$10^3 32$	-0.0131032(3)	-0.006341(8)
		$12^3 32$	-0.0029148(3)	0.0012405(6)
		$14^3 32$	-0.00083854(3)	0.00008748(3)
		$16^3 32$	0.00020948(3)	0.00004254(5)
		$24^3 40$	-0.000078415(8)	-0.00009462(1)
	0.1580	$12^3 32$	-0.003798(2)	0.005014(3)
		$14^3 32$	-0.00135725(6)	0.0003214(3)
		$16^3 32$	-0.00037040(4)	-0.00022400(4)
		$24^3 40$	-0.00010810(2)	0.00012503(1)

Table 4.6: Ensemble averages of the mean Wilson line in z-direction.

this case we would expect the generated gauge fields to resemble more those at finite temperature. In the absence of dynamical quarks, *i.e.* in quenched QCD, the expectation value of the Polyakov loop, which is defined as

$$\langle P \rangle = \left\langle \frac{1}{L^3} \sum_{\mathbf{x}} \text{Tr} \prod_{\tau=1}^{T} U_4(\mathbf{x}, \tau) \right\rangle, \tag{4.9}$$

is zero in the confined phase, while in the deconfined phase $\langle P \rangle \neq 0$. Therefore in pure gauge theory $\langle P \rangle$ is an order parameter for the deconfining phase transition. This is due to the global $Z(3)$ symmetry of the pure $SU(3)$ gauge theory which is spontaneously broken at the phase transition.[4] In full QCD the Polyakov loop is not an order parameter because the $Z(3)$ symmetry of the gluonic action is explicitly broken by the quark action, so that $\langle P \rangle$ is not exactly zero in the hadronic phase. In our simulations it is not the time extent T which is varied, but the spatial lattice size L. Due to the space-time symmetry of the Euclidean metric, however, similar considerations also apply to Polyakov-type loops in the spatial directions (which we also call *Wilson lines*). Let us, for definiteness, consider the mean Wilson line in z-direction, which is defined configuration-wise as

$$P_z = \frac{1}{L^2 T} \sum_{x_1, x_2, \tau} \text{Tr} \prod_{x_3=1}^{L} U_3(x_1, x_2, x_3, \tau). \tag{4.10}$$

As can be seen from Table 4.6, the expectation values $\langle P_z \rangle$ for all GRAL simulations are indeed significantly different from zero, even on the largest lattices. While for the larger lattices the

[4] A $Z(3)$ transformation is applied by multiplying all links originating from a given $x_\mu = \text{const.}$ hyperplane in direction μ by an element $z \in Z(3)$. The group $Z(3)$ is the center of $SU(3)$, *i.e.* it contains those elements of $SU(3)$ that commute with every $U \in SU(3)$. These elements are explicitly given by the complex numbers $z = e^{2\pi\nu i/3}$, $\nu = 0, 1, 2$. The pure gauge action S_g is left invariant by a $Z(3)$ transformation, similarly any closed (Wilson-type) loop that crosses the $x_\mu = \text{const.}$ plane the same number of times in the positive and in the negative μ-direction. Under a $Z(3)$ transformation of the time-like links on a $\tau = \text{const.}$ hyperplane, Polyakov loops transform according to $P \mapsto zP$.

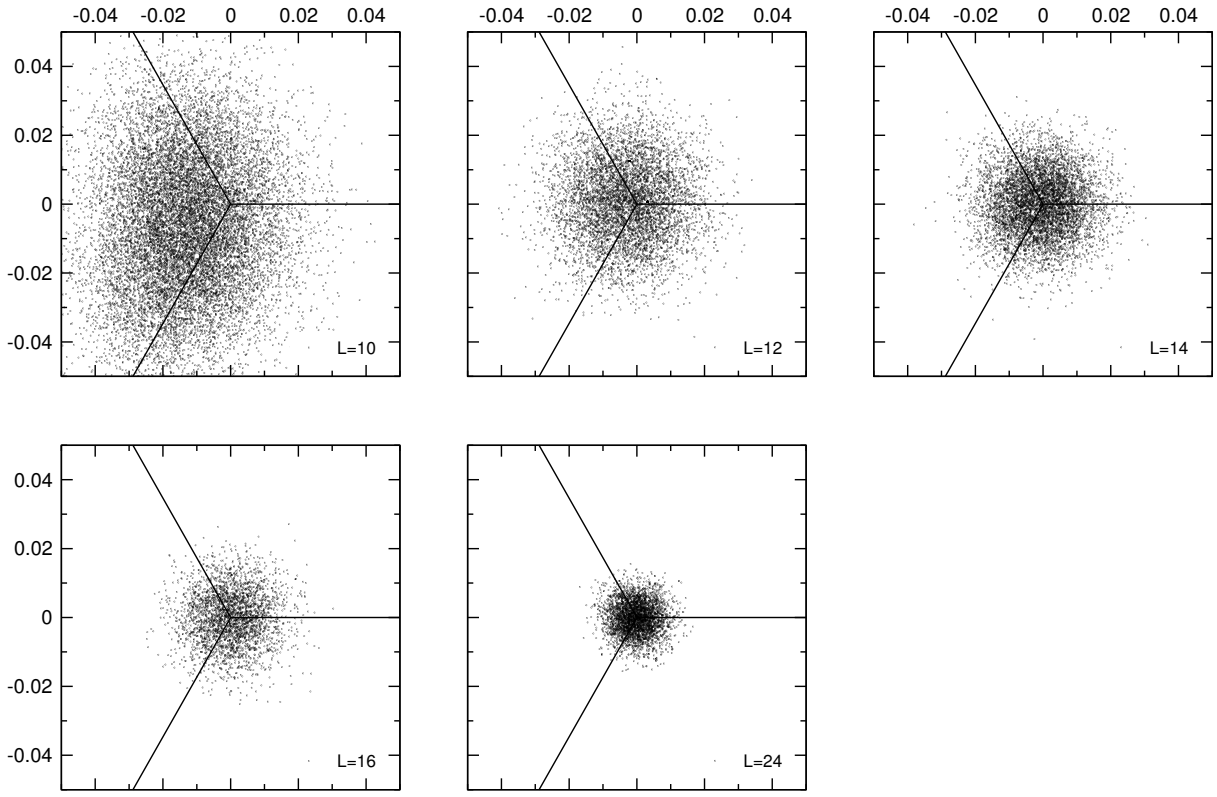

Figure 4.4: Distribution in the complex plane of the Wilson line P_z for the different lattices simulated at $(\beta, \kappa) = (5.6, 0.1575)$. The lines indicate the three $Z(3)$ directions 1, $e^{2\pi i/3}$ and $e^{4\pi i/3}$.

deviation from zero is relatively small it becomes more pronounced as the box size shrinks. $\langle \mathrm{Re}\, P_z \rangle$ in particular takes increasingly negative values towards the smaller lattice sizes. This can be understood by looking at the distribution of P_z.

Figure 4.4 shows the distribution in the complex plane of P_z for the lattice volumes simulated at $(\beta, \kappa) = (5.6, 0.1575)$. The lines in the plots indicate the three $Z(3)$ directions 1, $e^{2\pi i/3}$ and $e^{4\pi i/3}$. Apart from the L-dependent fluctuations we observe for the larger lattices an approximately point-symmetric accumulation of the Wilson line around zero. This is reflected in the smallness of $|\langle P_z \rangle|$ and the corresponding statistical errors at large L (see Table 4.6). The situation is somewhat different for the smallest, 10^3 lattice, where the distribution of Wilson lines is shifted towards the $Z(3)$ directions $e^{2\pi i/3}$ and $e^{4\pi i/3}$, which leads to the relatively large negative value of $\langle \mathrm{Re}\, P_z \rangle$.

The observed behavior of the Wilson line distribution as well as its implications for finite-size effects in hadron masses have been explained at length by S. Aoki *et al.* in the context of their comparative study of finite-size effects in quenched and full QCD simulations [60]. Here we briefly recapitulate their arguments for our choice of boundary conditions. Let us consider a meson propagator $\Gamma(\tau)$ on a lattice of size L^3 with a sufficiently large time extent T. A hopping parameter expansion of $\Gamma(\tau)$ yields a representation of the meson propagator in terms of closed valence quark loops C going through the meson source and sink. If we denote the corresponding link factors $\mathrm{Tr} \prod_{l \in C} U_l$ by $P(C)$ for Polyakov-type loops that wind around the lattice in a spatial

direction, and $W(C)$ for ordinary Wilson-type loops, the meson propagator can be written as

$$-\big\langle\Gamma(\tau)\big\rangle = \sum_C \kappa_{\rm val}^{L(C)} \big\langle W(C)\big\rangle + \sum_C \kappa_{\rm val}^{L(C)} \sigma_{\rm val} \big\langle P(C)\big\rangle, \tag{4.11}$$

where $L(C)$ is the length of the respective loop and the sign factor $\sigma_{\rm val}$ is equal to $+1$ for the periodic spatial boundary conditions used for valence quarks in our simulations. Our observed distribution of Wilson lines (spatial Polyakov loops) can be understood with the help of the 3-d Potts model with magnetic field that we recover when we expand the full QCD action first in the gauge coupling β and then in inverse powers of the sea quark mass [130]. Introducing the quark action in QCD is then equivalent to switching on a magnetic field h in the Potts model that breaks the $Z(3)$ symmetry of the system. Considering the phase of the spatial Polyakov loop as a spin that can take one of the three possible values 1, $e^{2\pi i/3}$ and $e^{4\pi i/3}$, the magnetic field aligns the spins to preferred directions depending on the sign of h: for $h = -|h|$ (corresponding to antiperiodic spatial boundary conditions for sea quarks) the positive real axis is favored, whereas for $h = +|h|$ (periodic spatial boundary conditions for sea quarks) the two directions $e^{2\pi i/3}$ and $e^{4\pi i/3}$ (pointing towards negative values) are preferred. If we recall that we have used periodic boundary conditions for sea quarks this explains the plot for $L = 10$ in figure 4.4. The discussion above shows, moreover, that in the case of periodic spatial boundary conditions for both sea and valence quarks the contribution of Polyakov-type loops to the meson propagator (4.11) is negative. Since mean values of Wilson-type loops are always positive, the two contributions in (4.11) have opposite sign, which leads to a faster decrease of the correlator and thus to a larger meson mass.

For fixed sea and valence quark mass this effect grows weaker for increasing lattice size because the contribution of the Polyakov-type loops decreases on the average. On the other hand, in a fixed lattice volume with periodic boundary conditions finite-size effects in hadron masses get increasingly significant both for decreasing sea and valence quark mass. This has indeed been observed *e.g.* in Ref. [124], where partially quenched chiral extrapolations of the pseudoscalar and vector masses were studied for the different $\kappa_{\rm sea}$-values at $\beta = 5.5$ and 5.6 (see Table 3.6). The sea quark mass dependence of the expectation value of the Wilson line can also be seen in Table 4.6 if one compares at $\beta = 5.6$ the value for a given lattice size at $\kappa_{\rm sea} = 0.1575$ with the corresponding value at $\kappa_{\rm sea} = 0.158$. We find that in the same volume $\langle \mathrm{Re}\, P_z\rangle$ is more negative for the larger $\kappa_{\rm sea}$, corresponding to a smaller quark mass. This leads to a stronger cancellation of the two terms in (4.11) and hence to a larger finite-size effect in the hadron masses.

For completeness, Figures 4.5 and 4.6 show the distribution of the Wilson line for the simulated volumes at $(\beta, \kappa) = (5.6, 0.158)$ and $(5.32144, 0.1665)$. For the smallest, 12^3 lattice at $(\beta, \kappa) = (5.6, 0.158)$ one might suspect a slight deviation from the rotation-symmetric pattern centered approximately around zero, as it is displayed by the other distributions. For a definite statement the statistical basis is probably too small, however.

4.4 Volume Dependence of the Light Hadron Masses

Let us now take a closer look at the actual lattice size dependence of our measured hadron masses. The three parameter sets for which we have simulated several lattice volumes, namely $(\beta, \kappa) = (5.6, 0.1575)$, $(5.6, 0.158)$ and $(5.32144, 0.1665)$, are characterized by the quark mass, which in turn can be expressed in terms of the pion mass via the GMOR relation. Therefore we sometimes quote the pion mass measured on the largest lattice, respectively, when we refer to a particular

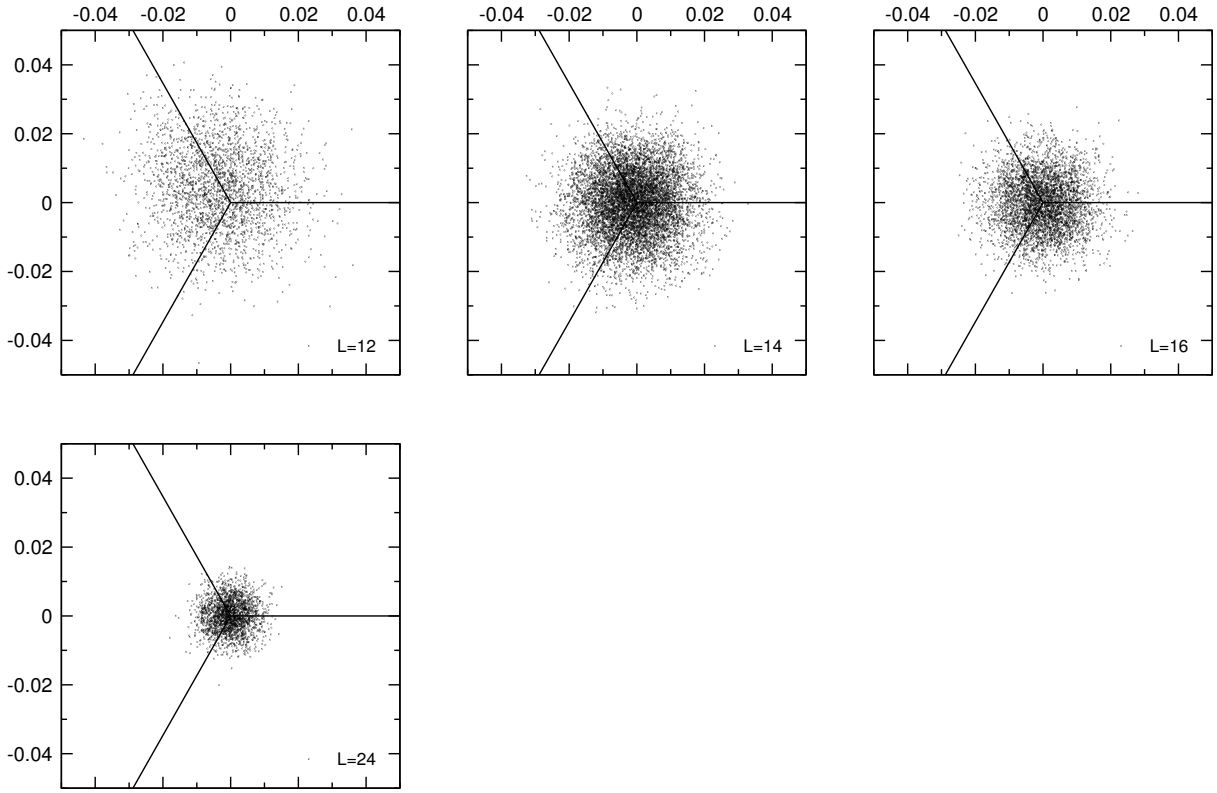

Figure 4.5: Same as Figure 4.4 for $(\beta, \kappa) = (5.6, 0.158)$.

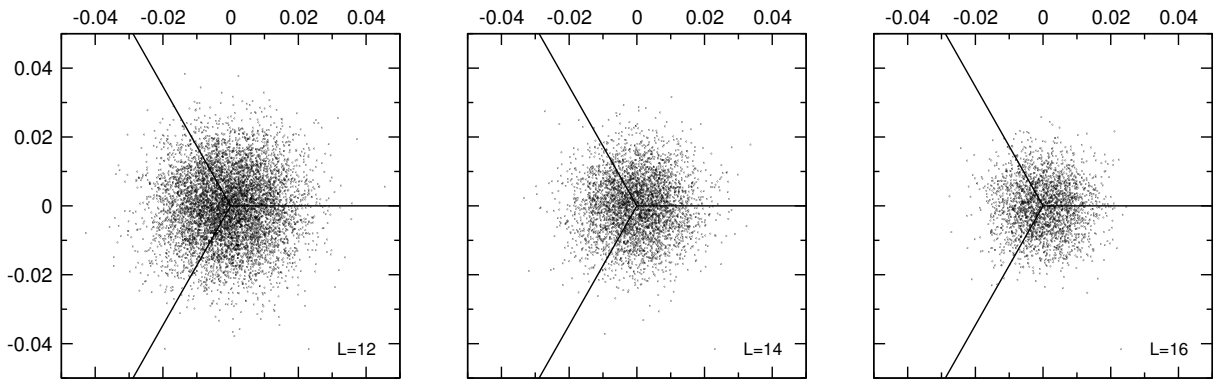

Figure 4.6: Same as Figure 4.4 for $(\beta, \kappa) = (5.32144, 0.1665)$.

β	κ_{sea}	L^3T	$\frac{M_{\text{PS}}}{4\pi F_{\text{PS}}/Z_A}$	R_{PS}	R_{V}	R_N
5.32144	0.1665	$12^3 32$	0.34(6)	-0.04(3)	0.02(5)	0.08(4)
		$14^3 32$	0.27(2)	-0.07(3)	0.04(3)	0.07(3)
		$16^3 32$	0.26(2)	0	0	0
5.6	0.1575	$10^3 32$	1.4(1)	0.78(3)	0.49(5)	0.76(4)
		$12^3 32$	0.66(6)	0.29(3)	0.25(3)	0.38(3)
		$14^3 32$	0.43(2)	0.10(2)	0.12(2)	0.21(3)
		$16^3 32$	0.36(2)	0.01(2)	0.02(2)	0.06(2)
		$24^3 40$	0.341(10)	0	0	0
	0.1580	$12^3 32$	1.4(8)	0.94(7)	0.52(6)	0.76(7)
		$14^3 32$	1.0(1)	0.48(4)	0.33(4)	0.44(5)
		$16^3 32$	0.39(2)	0.17(3)	0.05(5)	0.25(4)
		$24^3 40$	0.26(2)	0	0	0

Table 4.7: Ratios of the pseudoscalar mass to the chiral symmetry breaking scale, and the relative finite-size effects according to Eq. (4.12).

simulation point (β, κ) (bearing in mind that it is only a—sufficiently good—approximation to the true infinite volume pion mass). Hence we investigate the volume dependence of the pion, rho and nucleon for pion masses of approximately 643 MeV, 490 MeV and 419 MeV in the ranges 0.85 fm–2.04 fm, 0.96 fm–1.93 fm and 1.56 fm–2.08 fm, respectively. Although to our knowledge there is no theoretical prediction of the finite-size effect of the rho resonance we include it in our empirical analysis.[5]

Figures 4.7–4.9 show, for the three different quark masses, the pion, rho and nucleon masses in physical units as functions of the box-size.[6] Before we go into the details of the fits that are also shown in the plots, let us first discuss the general features of the data. In Table 4.7 we list the relative differences of the masses measured at L and L_{max},

$$R_H(L) = \frac{M_H(L) - M_H(L_{\text{max}})}{M_H(L_{\text{max}})}, \tag{4.12}$$

where $H = \text{PS}, \text{V}, \text{N}$ and $L_{\text{max}} = 24$ ($L_{\text{max}} = 16$) for $\beta = 5.6$ ($\beta = 5.32144$). In the plots and the table we find for both quark masses at $\beta = 5.6$ a large variation of the hadron masses over the considered range of lattice sizes. While the finite-size effects in the pion, rho and nucleon masses are relatively small if one compares only the two largest lattices at $\kappa = 0.1575$ (of the order of a few percent, in case of the pion it is not even significant), they rapidly grow on the smaller volumes ($\sim$ 50–80% at $L = 10$). The rate of the increase is hadron dependent: While at large L the pion has the smallest relative finite-size effect, the relative shift in the pion mass grows strongest with decreasing L, until it exceeds the effect in the rho mass from

[5] Due to angular momentum conservation the decay $\rho \to \pi\pi$ is suppressed on small lattices where the minimum non-zero momentum $2\pi/L$ is large.

[6] As we use the same scale r_0/a for all lattices at a given (β, κ) the conversion to physical units using $r_0 = 0.5\,\text{fm}$ simply amounts to a rescaling of the lattice sizes L by the same constant factor $(0.5\,\text{fm})/(r_0/a)$, while the raw lattice masses $M = am$ are multiplied by the inverse of this factor.

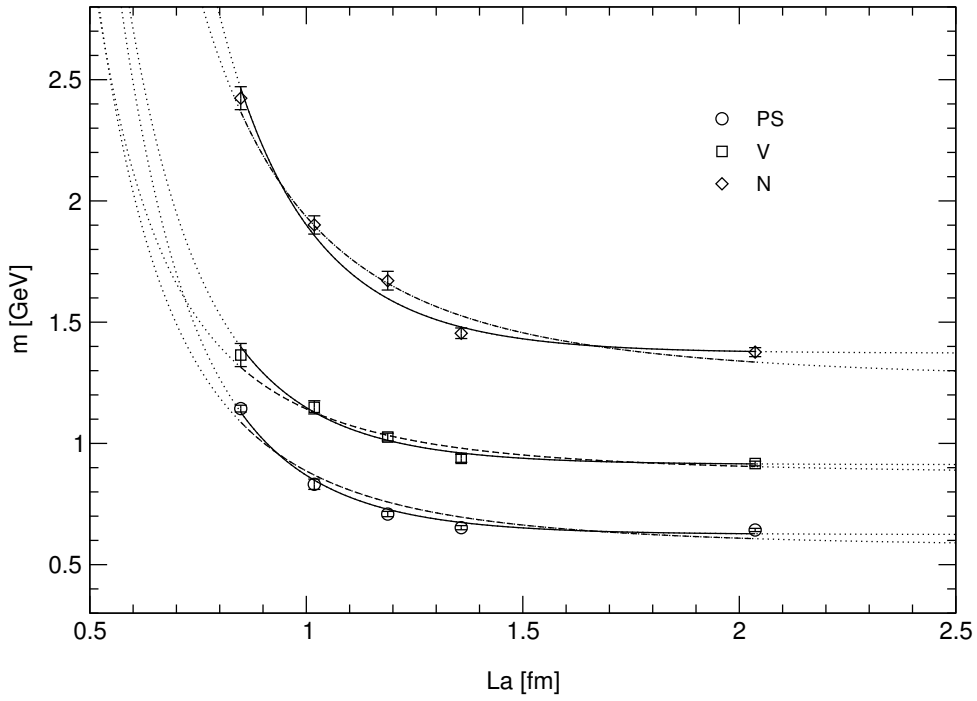

Figure 4.7: Box-size dependence of the pseudoscalar and vector meson masses and of the nucleon mass at $(\beta, \kappa) = (5.6, 0.1575)$. The solid lines correspond to exponential fits to (4.15) with $c_2 = m_{\rm PS}$, while the dashed lines represent fits to the power law (4.13) with $c_2 = 3$. Outside the fitted interval the curves are dotted.

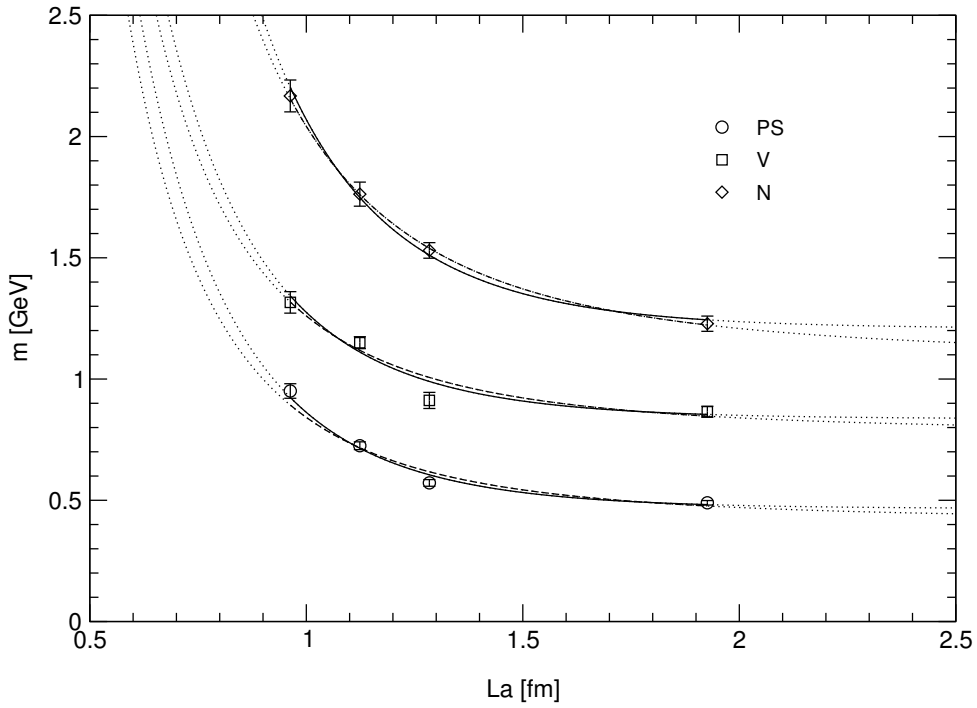

Figure 4.8: Same as Figure 4.7 for $(\beta, \kappa) = (5.6, 0.158)$.

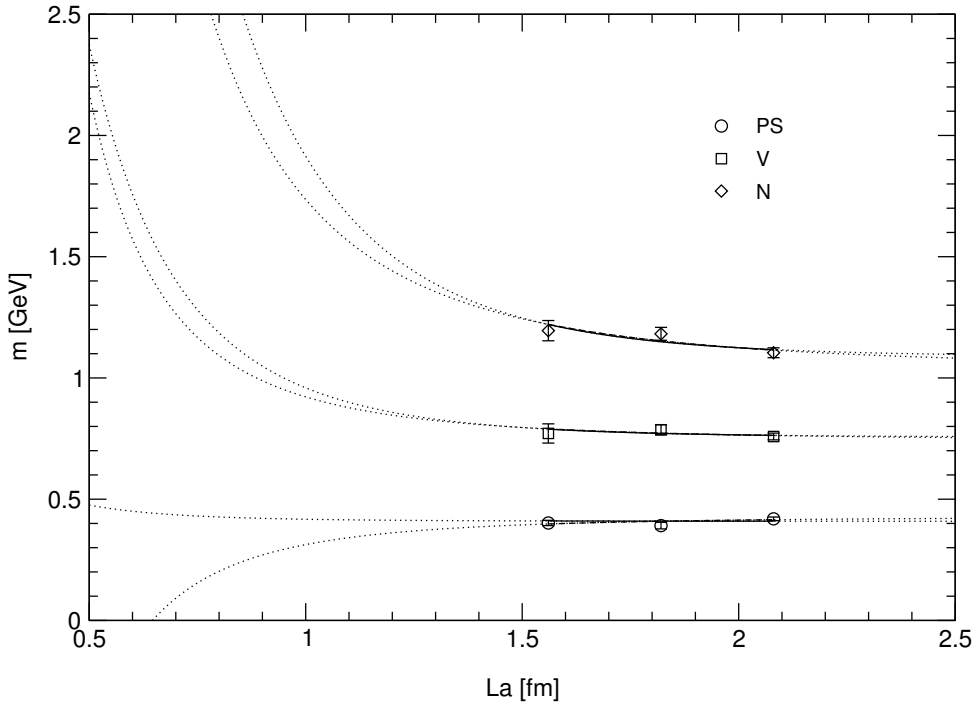

Figure 4.9: Same as Figure 4.7 for $(\beta, \kappa) = (5.32144, 0.1665)$.

$L = 12$ and that in the nucleon mass from $L = 10$ downwards. Considering the finite-size effects at $\kappa = 0.158$ (corresponding to a lower quark mass) we notice that at a given value of L the finite-size effects are generally much larger at $\kappa = 0.158$ than at 0.1575. Again we observe that the pion is subject to the strongest relative effect in the regime of small volumes. Finally, at $(\beta, \kappa) = (5.32144, 0.1665)$ (corresponding to the lightest of our quark masses), we find rather small finite-size effects of only a few percent in the simulated L-range, for all considered hadrons. In view of the small $M_{\rm PS}L$ values (see Table 4.4) this is rather striking: if the finite-size effects were a function of $M_{\rm PS}L$ only we would expect the effects at $\beta = 5.32144$ to match those on the smaller volumes at $\beta = 5.6$. On the other hand, due to the large lattice spacing at $\beta = 5.32144$, the simulated boxes are, in physical units, also quite large. Both the pion and the rho show no clear increase of the finite-size effect towards decreasing box-size, which we attribute to the smallness of the effect and statistical fluctuations (recall that the simulations with the smaller lattices at $\beta = 5.32144$ were affected by sizeable fluctuations). In case of the nucleon the finite-size effect is more significant. In view of these peculiarities we concentrate in the following investigations on $\beta = 5.6$ and defer a more detailed discussion of the data at $(\beta, \kappa) = (5.32144, 0.1665)$ to Section 4.4.2.

4.4.1 Simple Parameterizations of the Volume Dependence

In order to investigate empirically the functional form of the box-size dependence of our hadron mass data we first examine two "naive" parameterizations motivated by the formulae introduced in Chapter 2. It is important to realize that the formulae of Chapter 2 have their limited range of validity, respectively, which probably does not coincide with the entire parameter regime spanned by our simulations. In particular those formulae involving results from chiral perturbation theory

require rather small quark masses, and Lüscher's asymptotic formula moreover requires large volumes. As we are first of all interested in the question whether we can find a parameterization of the finite-size effects that connects small and medium-sized volumes to the asymptotic regime we defer a more detailed discussion of the applicability of the ChPT-related formulae until we have seen how well the volume dependence of our data can be described by simpler functions. In the following we focus on the data sets at $(\beta, \kappa) = (5.6, 0.1575)$ and $(5.6, 0.158)$. While on the basis of the Polyakov loop distributions considered in Section 4.3 one might suspect that the smallest lattices at these parameters are already too small, an unbiased look at the measured hadron masses does not immediately confirm this suspicion. We therefore do not exclude these data points *a priori* from the following fits.

Power Law

The first ansatz that we study is a power law of the form

$$\text{pow:} \qquad m_H(La) = m_H + c_1(La)^{-c_2}. \tag{4.13}$$

We first keep the parameter c_2 fixed at 3. The parameters m_H and c_1 as determined by fitting the pion (PS), rho (V) and nucleon (N) data to (4.13) are listed in Tables D.1–D.3 in the appendix. For each of the 2-parameter fits we use at least three data points. The last two columns of the tables show the relative deviations of $m_H(L_{\max}a)$ and $m_H \equiv m_H(La = \infty)$ (as obtained from the fits) from the hadron mass measured on the largest available lattice, respectively.[7] We examine the effect of the fit range $[L_1, L_2]$ on the quality of the fits by first keeping L_1 fixed and increasing L_2 up to its maximal value, and then varying L_1 for fixed L_2. On inspection of the fit results for $(\beta, \kappa) = (5.6, 0.1575)$ we observe that for the same number of degrees of freedom χ^2 is in general smaller in the region of small L than in the asymptotic regime. The same is true for the pion and the nucleon at $(\beta, \kappa) = (5.6, 0.158)$ (where the rho data cannot be fitted very well in general). The fit results for the maximal fit ranges, $[L_{\min}, L_{\max}]$, are displayed for all our β, κ combinations in Figures 4.7–4.9 (dashed curves). On the whole we find that the power law with fixed $c_2 = 3$ provides an acceptable description of the data at our two larger quark masses as long as the box-size is small ($\lesssim 1.5\,\text{fm}$) and the relative finite-size effects are of the order of at least several percent. From our results at $(\beta, \kappa) = (5.6, 0.1575)$ and $(5.6, 0.158)$ we infer that in terms of $M_{\text{PS}}L$ the L^{-3} behavior holds within the regime of

$$M_{\text{PS}}L \lesssim 4.5..4.8. \tag{4.14}$$

In view of this result it is clear that the power law cannot correctly predict the asymptotic finite-size effect. As we assume the largest, 24^3 volume at $(\beta, \kappa) = (5.6, 0.1575)$ to be—for all practical purposes—free of finite-size effects, it is obvious from Table D.1 that an extrapolation of the power law from its validity domain at small volumes to the infinite volume grossly overestimates the true finite-size effect.

The next ansatz we consider is the power law (4.13) with c_2 as a free parameter. The parameter values resulting from different fits of the data are listed in Tables D.4–D.6 in the appendix. We find acceptable descriptions of the data with χ^2/dof ranging between 2.24 (pion) and 3.82 (nucleon) at $(\beta, \kappa) = (5.6, 0.1575)$, while at $(\beta, \kappa) = (5.6, 0.158)$ the fit quality is somewhat

[7] By $L_{\max} = L_{\max}(\beta, \kappa)$ we denote the largest linear lattice size we have simulated for a given β, κ combination: $L_{\max} = 24$ for the two κ-values at $\beta = 5.6$, and $L_{\max} = 16$ for $\beta = 5.32144$. Similarly, $L_{\min}(5.6, 0.1575) = 10$ and $L_{\min}(5.6, 0.158) = L_{\min}(5.32144, 0.1665) = 12$.

worse ($\chi^2/\mathrm{dof} = 4.18$ for the pion and 9.23 for the rho). On the other hand, just as it was the case with our previous ansatz, the nucleon data at $(\beta, \kappa) = (5.6, 0.158)$ fit the power law particularly well ($\chi^2/\mathrm{dof} = 0.02$). The general improvement in the fit quality as compared to the parameterization with fixed c_2 is of course due to the increased number of degrees of freedom. At the larger quark mass the values for c_2 obtained from the fits are significantly larger than 3; they range from approximately 4 (nucleon) to 6 (pion). This is an effect of the 24^3 lattice with $M_\pi L = 6.6$. In contrast, $M_\pi L = 4.8$ at $L = 24$ for the lower quark mass, and so the exponents are close to or even compatible with 3.

Single Exponential

Let us now, for comparison, consider the exponential formula

$$\text{exp:} \qquad m_H(La) = m_H + c_1 \frac{e^{-c_2 La}}{(La)^{3/2}} \tag{4.15}$$

with three fit parameters: m_H, c_1 and c_2. The values obtained from the fits of our data are again summarized in the appendix (Tables D.7–D.9). The overall quality of the fits is better than that of the 3-parameter power law fits, and the relative deviations of the exponential fit functions at $L = L_{\max}$ and $L = \infty$ from the data at $L_{\max}$ are substantially reduced compared to the power law.

Since for $(\beta, \kappa) = (5.6, 0.1575)$ as well as for $(5.6, 0.158)$ the obtained values for c_2 are close to or even consistent with the respective infinite-volume pseudoscalar mass m_{PS} we are encouraged to try out the parameterization (4.15) with the constraint $c_2 = m_{\mathrm{PS}}$. [8] The parameters obtained from these fits are displayed in Tables 4.8–4.10, complemented for comparison by the parameters from the power law fits with $c_2 = 3$. The corresponding fit functions are plotted in Figures 4.7–4.9 (solid: exponential with $c_2 = m_{\mathrm{PS}}$; dashed: power law with $c_2 = 3$). We clearly observe that over the entire range of simulated lattice sizes the exponential ansatz is superior to the cubic power law. (Note that the number of free parameters is the same in both cases.) Moreover, except for the case of the pion mass at $(\beta, \kappa) = (5.6, 0.1575)$ the quality of the exponential fits with $c_2 = m_{\mathrm{PS}}$ is comparable to or even better than that of the previous fits without this constraint. We find that with this ansatz all predicted asymptotic masses at $(\beta, \kappa) = (5.6, 0.1575)$ are compatible with the measured masses from the 24^3 lattice (see Table 4.4), in accordance with our presumption that this rather large lattice should bear no significant finite-size effects. For the masses at $(\beta, \kappa) = (5.6, 0.158)$ small effects between 1.6% for the nucleon and 4.9% in case of the pion are predicted for the 24^3 lattice. In order to study the stability of these results with regard to the fitted L-range we varied the lower boundary L_1 for fixed $L_2 = L_{\max}$; the results are summarized in Tables D.10–D.12 in the appendix.

Extrapolation

In order to check whether we can use this ansatz for an extrapolation from the small lattices to the infinite volume we again focus on our data sets at $(\beta, \kappa) = (5.6, 0.1575)$ and $(5.6, 0.158)$. Figures 4.10 and 4.11 show fits of the measured masses to the exponential (4.15) with $c_2 = m_{\mathrm{PS}}$. The different curves correspond to different lower boundaries L_1 of the fitted range $[L_1, L_2]$, with

[8] At $(\beta, \kappa) = (5.32144, 0.1665)$, corresponding to our smallest quark mass, the finite-size effect in the pseudoscalar mass is small. We can therefore fit the three available data points with the two constraints $c_1 = C$ and $c_2 = m_{\mathrm{PS}}$, so that the infinite-volume pion mass m_{PS} remains the only free parameter.

Fit type	H	$[L_1,L_2]$	$m_H\,[\mathrm{GeV}]$	$c_1\,[\mathrm{GeV}^{-d}]$	χ^2/df	$\Delta(L_{\max})$	$\Delta(L=\infty)$
pow ($c_2=3$)	PS	10,24	0.570(35)	41.2(7.1)	31.65	-5.57%	-11.40%
pow ($c_2=3$)	V	10,24	0.872(19)	35.1(5.3)	3.34	-1.38%	-4.87%
pow ($c_2=3$)	N	10,24	1.255(43)	88.5(9.3)	5.83	-2.99%	-8.84%
exp ($c_2=m_{\mathrm{PS}}$)	PS	10,24	0.624(13)	65.9(4.2)	5.59	-2.41%	-2.91%
exp ($c_2=m_{\mathrm{PS}}$)	V	10,24	0.9125(92)	63.5(5.6)	1.19	-0.17%	-0.51%
exp ($c_2=m_{\mathrm{PS}}$)	N	10,24	1.372(22)	142.7(9.5)	2.37	0.18%	-0.32%

Table 4.8: Fit parameters for $(\beta,\kappa)=(5.6,0.1575)$. $d=2$ for "pow" (Eq. (4.13)) and $d=1/2$ for "exp" (Eq. (4.15)).

Fit type	H	$[L_1,L_2]$	$m_H\,[\mathrm{GeV}]$	$c_1\,[\mathrm{GeV}^{-d}]$	χ^2/df	$\Delta(L_{\max})$	$\Delta(L=\infty)$
pow ($c_2=3$)	PS	12,24	0.417(33)	55.3(9.2)	8.55	-2.67%	-14.81%
pow ($c_2=3$)	V	12,24	0.780(59)	62.5(13.1)	5.22	-2.10%	-9.86%
pow ($c_2=3$)	N	12,24	1.0894(92)	124.0(2.3)	0.07	-0.44%	-11.30%
exp ($c_2=m_{\mathrm{PS}}$)	PS	12,24	0.466(20)	47.9(4.2)	3.86	-1.50%	-4.91%
exp ($c_2=m_{\mathrm{PS}}$)	V	12,24	0.836(45)	53.1(10.0)	4.31	-1.27%	-3.41%
exp ($c_2=m_{\mathrm{PS}}$)	N	12,24	1.208(20)	104.1(5.1)	0.50	1.30%	-1.65%

Table 4.9: Same as Table 4.8 for $(\beta,\kappa)=(5.6,0.158)$.

Fit type	H	$[L_1,L_2]$	$m_H\,[\mathrm{GeV}]$	$c_1\,[\mathrm{GeV}^{-d}]$	χ^2/df	$\Delta(L_{\max})$	$\Delta(L=\infty)$
pow ($c_2=3$)	PS	12,16	0.428(22)	-15.0(16.3)	2.09	-0.83%	2.23%
pow ($c_2=3$)	V	12,16	0.743(32)	23.3(29.0)	0.77	0.54%	-2.08%
pow ($c_2=3$)	N	12,16	1.037(63)	90.9(52.8)	1.87	0.98%	-6.05%
exp ($c_1=C, c_2=m_{\mathrm{PS}}$)	PS	12,16	0.4089(81)		2.04	-2.36%	-2.36%
exp ($c_2=m_{\mathrm{PS}}$)	V	12,16	0.756(20)	18.4(26.7)	0.86	0.64%	-0.31%
exp ($c_2=m_{\mathrm{PS}}$)	N	12,16	1.088(42)	74.9(50.5)	2.32	1.19%	-1.46%

Table 4.10: Same as Table 4.8 for $(\beta,\kappa)=(5.32144,0.1665)$.

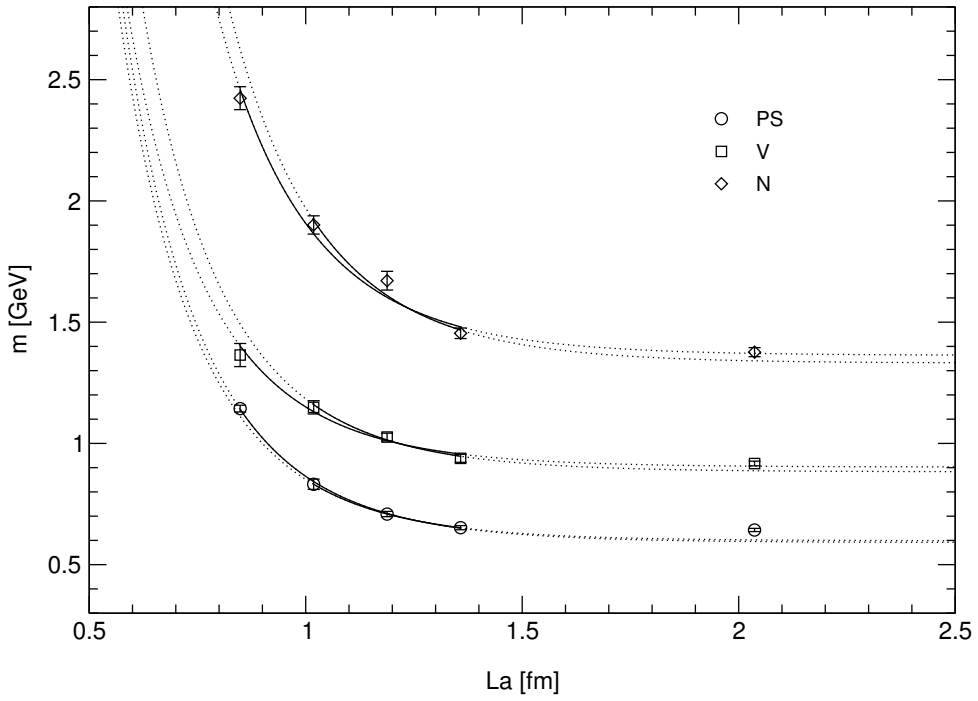

Figure 4.10: Infinite-volume extrapolation of the masses at $(\beta, \kappa) = (5.6, 0.1575)$. The solid lines correspond to exponential fits according to (4.15) with $c_2 = m_{\mathrm{PS}}$. Outside the fitted intervals the curves are dotted.

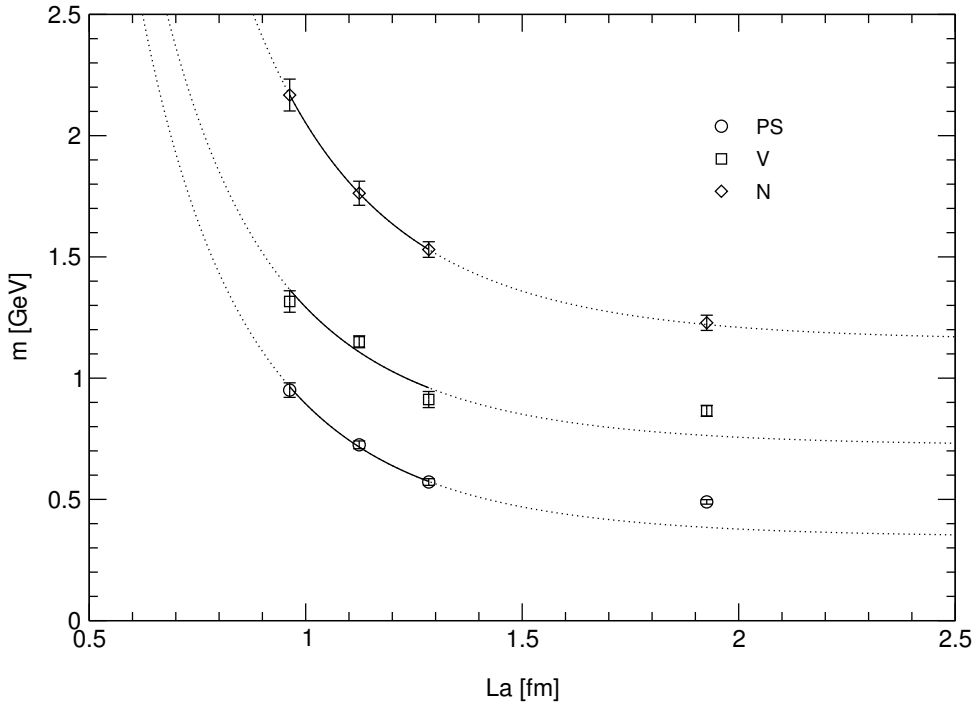

Figure 4.11: Same as Figure 4.10 for $(\beta, \kappa) = (5.6, 0.158)$.

L_2 kept fixed at 16 (see Tables D.13 and D.14 for numbers). All the fits (again except for the case of the vector meson at $\kappa = 0.158$) describe the data well within the fitted regime. Let us first take a closer look at Figure 4.10, where we take the deviation of the fit curves from the data points at $L_{\max} = 24$ as a measure of the quality of the extrapolation (Table D.13). We find that, while $m_{\mathrm{PS}}(L_{\max}a)$ is underestimated by 6.3–7.4%, the predictions for the rho and the nucleon are consistent with the data at $L_{\max}$, respectively, if the data are fitted from $L = 10$. On the other hand, the fit of the pseudoscalar mass is quite stable with regard to the left boundary of the fitted L-range, whereas in case of both the vector meson and the nucleon the deviation of the fitted function from the data at $L_{\max}$ increases significantly with larger L_1. At $\kappa = 0.1575$, corresponding to the smaller quark mass at $\beta = 5.6$, $m_{\mathrm{PS}}(L_{\max}a)$ is underestimated even more (by 21–28%). While the vector meson mass also comes out too low (by at least 12%), the prediction of the nucleon mass at $L_{\max}$ agrees remarkably well with the data.

Conclusion

Our findings suggest that we are in an intermediate, sub-asymptotic regime where we see a transition behavior in the volume dependence of the light hadron masses . "Naive" approaches like the cubic power law or the single exponential function provide satisfactory empirical descriptions of the finite-size dependence in limited ranges of L. We can confirm that the power law works well in the regime of small volumes, while it fails at larger L where the finite-size effects become small. There we clearly see an exponential behavior in our data for the light hadron masses. Unless we include data points with quite small finite-size effects (of the order of a few percent) into the fits, the asymptotic masses are generally underestimated considerably (more so for the pion, less for the nucleon). However, we can at least obtain lower bounds for the infinite-volume masses, the systematic errors of which may be estimated by varying the boundaries of the fitted L-intervals.

4.4.2 Discussion of the Applicability of ChPT Formulae

In order to understand why it is so problematic to extrapolate reliably from small volumes to the infinite volume on the basis of the simple formulae (4.13) and (4.15) (at the quark masses and lattice volumes considered so far), we need to appreciate their respective origin and scope. The power law (4.13) is, in fact, expected to hold only for *small* volumes, where it is supposed to originate from a distortion of the hadronic wave function (or, alternatively, from a modification of the effect of virtual particles traveling around the lattice by a model-dependent form factor that accounts for the finite hadron extent). Consequently, the L^{-3}-behavior cannot be expected to persist towards large volumes, and this is indeed borne out by our data. On the other hand, the formula (4.15) essentially corresponds to Lüscher's asymptotic formulae for the pion and the nucleon. Lüscher's general formula for the volume dependence of stable particles in a finite volume is designed to yield the *leading term* in a large L expansion, meaning that whenever the relative suppression factor

$$\frac{\text{subleading}}{\text{leading}} = O\left(e^{-(\bar{M}-M_\pi)L}\right) \tag{4.16}$$

is not small, subleading effects may be of practical relevance.

Pion

In the case of the pion we furthermore rely on chiral perturbation theory to provide us with an analytic expression for the $\pi\pi$ elastic forward scattering amplitude $F_{\pi\pi}$. At leading order in the chiral expansion this amplitude is given by the constant expression $F_{\pi\pi} = -m_\pi^2/f_\pi^2$. Inserted into the Lüscher formula this leads to (2.19), which then has the functional form of our exponential ansatz (4.15). We have seen that the data can be well described by the parameterization (4.15) with the constraint $c_2 = m_{\rm PS}$. It is therefore instructive to compare our results for the parameter c_1 to the constant

$$C = \frac{3}{4(2\pi)^{3/2}} \frac{m_{\rm PS}^{3/2}}{(f_{\rm PS}/Z_A)^2} \tag{4.17}$$

(see Eq. (2.19)), when for each (β, κ) we take $m_{\rm PS}$ and $f_{\rm PS}/Z_A$ from the largest available lattice, respectively (see Tables 4.3 and 4.5; for definiteness we use $f_{\rm PS}^{(1)}/Z_A$). For our simulation points $(\beta, \kappa) = (5.6, 0.1575)$, $(5.6, 0.158)$ and $(5.32144, 0.1665)$ we have $C/\mathrm{GeV}^{-1/2} = 1.089(61)$, $0.745(98)$ and $0.79(12)$, respectively.[9] Comparing the first two of these values to the results for c_1 in Tables 4.8 and 4.9 (PS) we see that the relative factor between c_1 and C is $O(10)$ provided that, as we expect, $Z_A = O(1)$. The discrepancy is generally larger for smaller L_1 and decreases for increasing values of the left fit boundary.

The large discrepancies between the coefficients c_1 from the fits to our pion data and C from the Lüscher formula (with LO ChPT input) reflect the fact that not all of our data sets for the different volumes at $(\beta, \kappa) = (5.6, 0.1575)$ and $(5.6, 0.158)$ comply with the conditions of applicability of this formula. Recall that these conditions are: (i) sufficiently large lattice volumes (because the the Lüscher formula corresponds to the leading term in a large L expansion), and (ii) small pion masses (because we take the pion scattering amplitude from chiral perturbation theory).

Quite recently, G. Colangelo and S. Dürr have determined the finite-size shift of the pion mass using Lüscher's formula with the $\pi\pi$ forward scattering amplitude taken from two-flavor chiral perturbation theory up to NNLO in the chiral expansion [65]. These results have then been compared to the leading order chiral expression for the pion mass in finite volume (including the large-L suppressed terms neglected by the Lüscher formula) in order to estimate the effect of subleading terms in the large L expansion.[10] Both aspects of their investigation rely on chiral perturbation theory as an expansion in the pion mass m_π and the particle momenta p, both of which have to be small compared to the chiral symmetry breaking scale that is usually identified with $4\pi f_\pi$. The conditions of applicability thus read [65]

$$\frac{m_\pi}{4\pi f_\pi} \ll 1 \tag{4.18}$$

and

$$\frac{p}{4\pi f_\pi} \ll 1. \tag{4.19}$$

In a finite box of size La (with periodic boundary conditions), where the particles' momenta can only take discrete values $p_k = 2\pi n_k/(La)$ with $n_k \in \mathbb{Z}$, the second condition directly translates

[9] Using $m_\pi = 137\,\mathrm{MeV}$ and $f_\pi = 92.4\,\mathrm{MeV}$ the natural value is $C = 0.283\,\mathrm{GeV}^{-1/2}$.

[10] A calculation of the next to leading term (in L) of the *general* Lüscher formula is a non-trivial task that has not been tackled yet (see also Lüscher's concluding remarks in Ref. [53]).

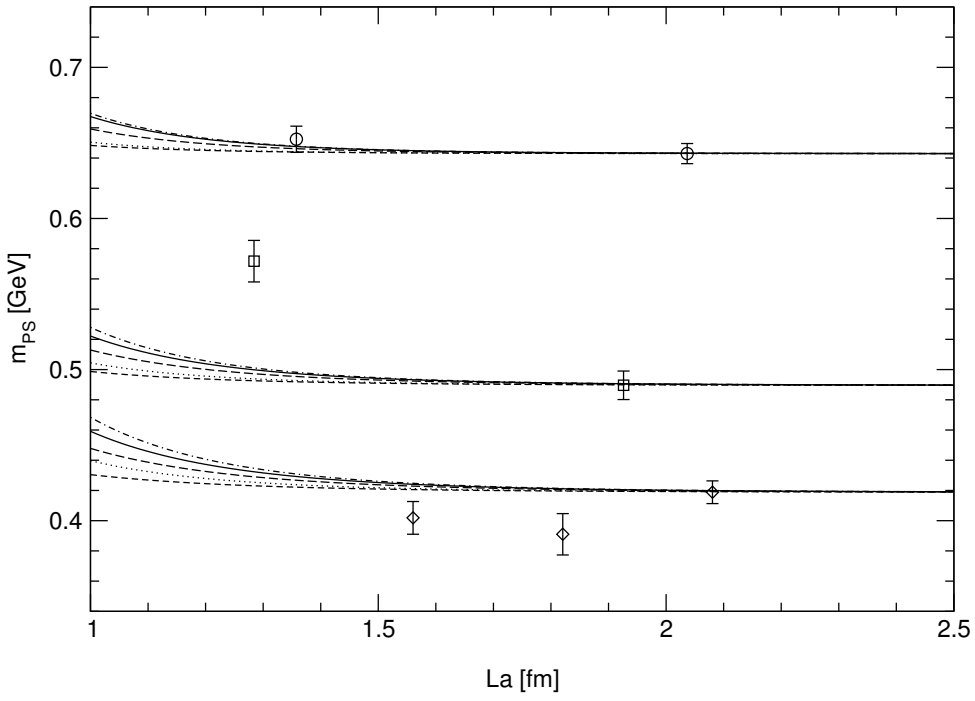

Figure 4.12: Volume dependence of our pion masses in the regime $La \gtrsim 1.3\,\mathrm{fm}$. The circles, squares and diamonds represent our data at $(\beta,\kappa) = (5.6, 0.1575)$ ($m_\pi = 643\,\mathrm{MeV}$), $(\beta,\kappa) = (5.6, 0.158)$ ($m_\pi = 490\,\mathrm{MeV}$) and $(\beta,\kappa) = (5.32144, 0.1665)$ ($m_\pi = 419\,\mathrm{MeV}$), respectively. The curves correspond to Lüscher's formula with input from ChPT at LO (dashed), NLO (long-dashed) and NNLO (solid). The dotted curves show the full LO chiral expression. The dash-dotted curve is the full LO result shifted by the difference between the NNLO and the LO Lüscher formula.

into a bound on the box size:[11]

$$La \gg \frac{1}{2f_\pi} \sim 1\,\mathrm{fm}. \tag{4.20}$$

Although *a priori* it is not clear what the practical significance of the relations (4.18) and (4.20) is, we can identify on the basis of the Tables 4.7 and 4.4 those data sets that stand the greatest chance of meeting these criterions. From Table 4.7 we see that the ratios $M_{\mathrm{PS}}(L)/(4\pi Z_A^{-1} F_{\mathrm{PS}}(L))$ for all simulated volumes at $(\beta,\kappa) = (5.32144, 0.1665)$ are relatively small and compatible with each other. The corresponding ratio at $(\beta,\kappa) = (5.6, 0.158)$ is also relatively small for $L = L_{\max}$ (and, moreover, comparable to the numbers at $(5.32144, 0.1665)$), but the value for the second largest lattice is already significantly larger. Considering only the largest lattice, respectively, $M_{\mathrm{PS}}/(4\pi Z_A^{-1} F_{\mathrm{PS}})$ is largest at $(\beta,\kappa) = (5.6, 0.1575)$, but here the value at $L = 16$ is still consistent with the one at $L_{\max} = 24$. In the light of these findings and recalling the relative finite-size mass shifts R (Table 4.7) we infer from Table 4.4 that for $m_\pi = 643\,\mathrm{MeV}$ and $m_\pi = 490\,\mathrm{MeV}$ we can trust ChPT only on the largest volumes with $La \approx 2\,\mathrm{fm}$ (and possibly the 16^3 lattice with $La \approx 1.4\,\mathrm{fm}$ at $m_\pi = 643\,\mathrm{MeV}$), while the lattices with $La < 1.4\,\mathrm{fm}$ are most probably too small. At $(\beta,\kappa) = (5.32144, 0.1665)$, on the other hand, where $m_\pi = 419\,\mathrm{MeV}$, all lattices are larger than 1.5 fm due to the relatively large lattice spacing, and hence appear large enough for ChPT to be applicable.

[11] As illustrated in Ref. [65], the pion mass dependence of f_π predicted by ChPT at NNLO is rather mild. We use the physical value here.

In order to corroborate these observations let us see how our simulated pion masses $m_{\mathrm{PS}}(La)$, for $La \gtrsim 1.3\,\mathrm{fm}$, relate to the results of Ref. [65]. There, the chiral expression for the elastic $\pi\pi$ forward scattering amplitude $F_{\pi\pi}$ is written as an expansion in powers of ξ,

$$F_{\pi\pi} = 16\pi^2 \left[\xi F_2 + \xi^2 F_4 + \xi^3 F_6 + O(\xi^4)\right], \tag{4.21}$$

where the parameter ξ is defined as

$$\xi = \left(\frac{m_\pi}{4\pi f_\pi}\right)^2. \tag{4.22}$$

Inserting the expansion (4.21) up to F_4 or F_6 into Lüscher's formula (2.10) for the pion and using the chiral expression for the isospin invariant amplitude A of Ref. [131], the leading term in the large-L expansion is obtained up to NLO and NNLO in the chiral expansion. (Correspondingly, inserting (4.21) into (2.10) only up to F_2 yields the LO expression (2.18).) In order to calculate the predicted finite size shift for the pion numerically for our three different pion masses we need to know the numerical value of the expansion parameter ξ, respectively. In order to avoid the difficulties associated with the renormalization of the pion decay constant one can use the analytic expression for the pion mass dependence of f_π which is known to NNLO in ChPT. If we take the pion mass from the largest lattice as a first approximation to the asymptotic pion mass m_π, respectively, we obtain the curves displayed in Figure 4.12. The dashed curves correspond to Lüscher's formula (2.18) with $F_{\pi\pi}$ from ChPT at leading order. The long-dashed and solid curves show the NLO and NNLO predictions, respectively. For comparison, the dotted curves show the full leading-order chiral expression ($N_f = 2$) for the pion mass in finite volume, given by [65]

$$m_\pi(La) = m_\pi \left[1 + \xi \sum_{n=1}^{\infty} m(n)\, \frac{K_1(\sqrt{n}\, m_\pi La)}{\sqrt{n}\, m_\pi La}\right], \tag{4.23}$$

where the multiplicity $m(n)$ counts the number of integer vectors $\mathbf{n}$ satisfying $n_1^2 + n_2^2 + n_3^2 = n$. Since the modified Bessel function $K_1(x)$ falls off exponentially for large x, the sum in (4.23) is rapidly converging. For $n = 1$ Eq. (4.23) corresponds precisely to the LO Lüscher formula (2.18). Finally, the dash-dotted curve in Figure 4.12 represents an estimate of the full finite-size effect obtained by adding to the Lüscher formula with $F_{\pi\pi}$ at NNLO the difference between equation (4.23) and the Lüscher formula with $F_{\pi\pi}$ at LO. This is the best theoretical estimate currently available.

The main conclusion we draw from the plot is that for all our three pion masses and for our lattices with $La \gtrsim 1.3\,\mathrm{fm}$ the finite-size effects predicted by ChPT are considerably smaller than our statistical errors. On the largest lattices with $La \simeq 2\,\mathrm{fm}$ the maximal predicted finite-size correction (corresponding to the dash-dotted curve in the plot) is about 0.3% for the lightest pion and 0.05% for the heaviest one. This is in accordance with our presumption that for all practical purposes the finite-size effects in the pion masses are negligible on our largest lattices. At $La \simeq 1.3\,\mathrm{fm}$ the finite-size shift ranges between 1% for the heaviest and about 3% for the lightest pion, which is of the order of the statistical uncertainties. For $La \gtrsim 1.3\,\mathrm{fm}$ the differences between the full one-loop ChPT result and Lüscher's formula with $F_{\pi\pi}$ at LO are comparably small, indicating that here the use of Lüscher's asymptotic formula is indeed justified; the maximal difference in the relative effects is about 50% at $La \simeq 1.3\,\mathrm{fm}$ for the smallest pion mass. By contrast, the difference between the relative effects predicted by Lüscher's formula with $F_{\pi\pi}$ at NNLO and LO amounts, for the same lattice size, to a factor of 3.2 for the lightest and 4.5 for the heaviest pion.

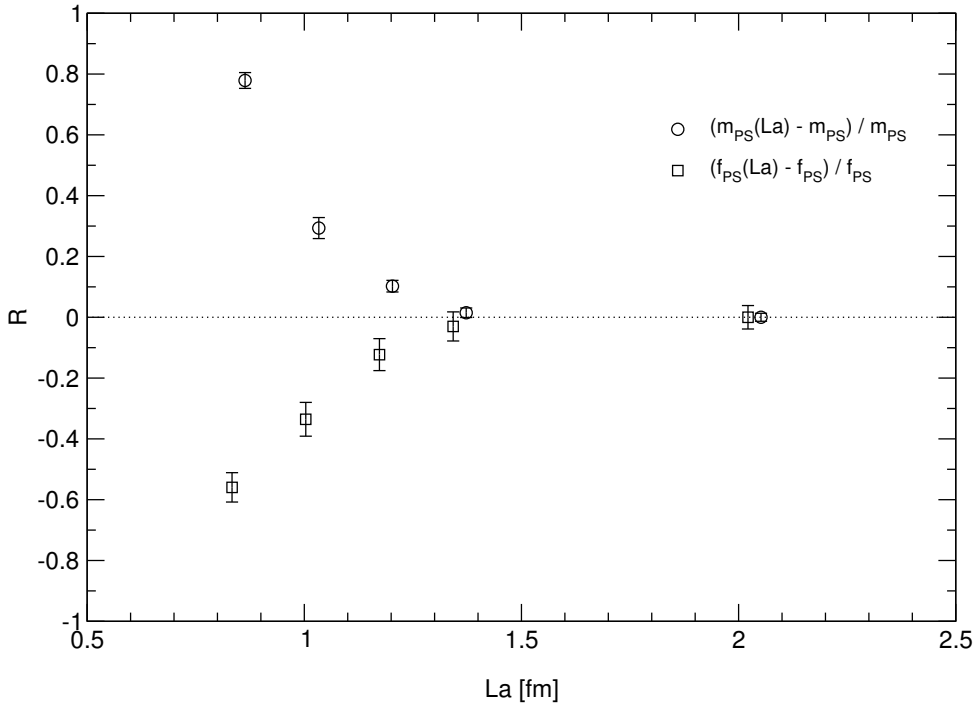

Figure 4.13: Relative box-size dependence of the pseudoscalar meson mass and decay constant at $(\beta, \kappa) = (5.6, 0.1575)$.

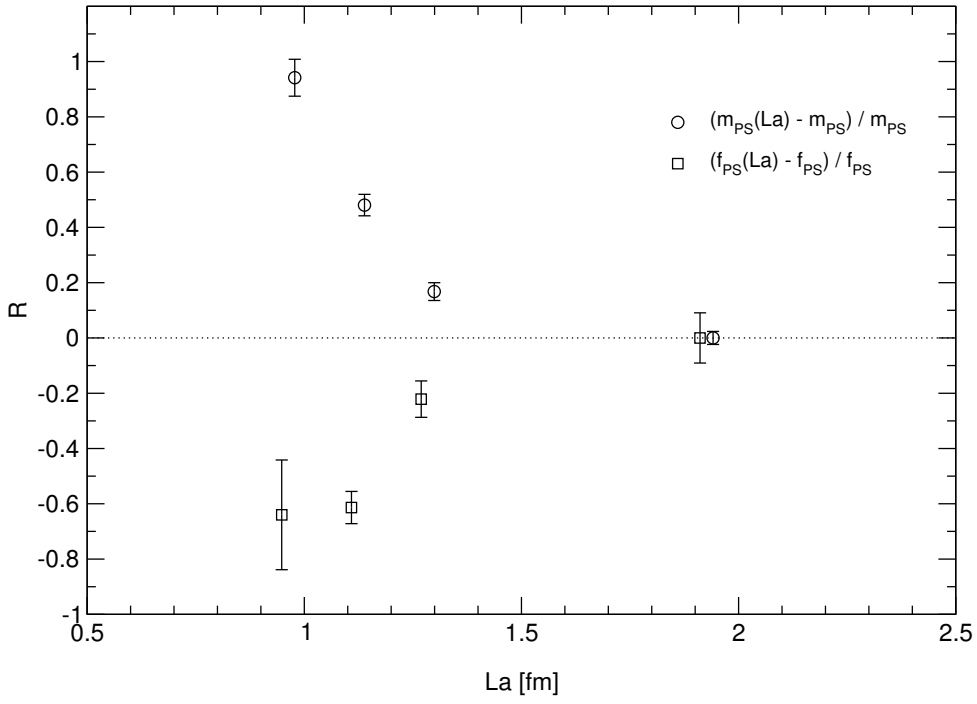

Figure 4.14: Same as Figure 4.13 for $(\beta, \kappa) = (5.6, 0.158)$.

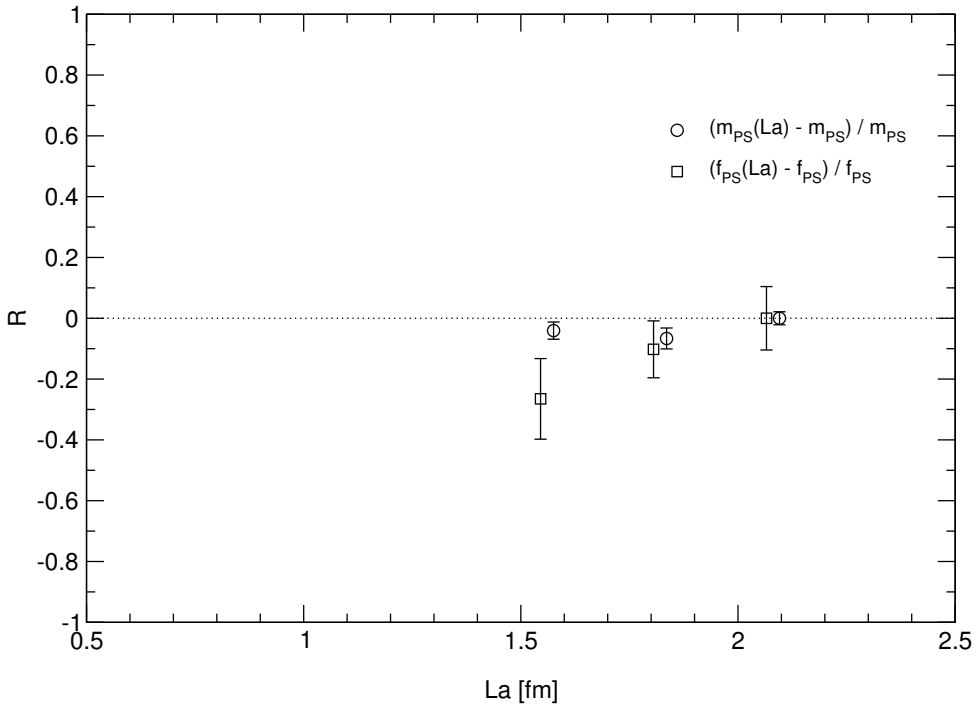

Figure 4.15: Same as Figure 4.13 for $(\beta, \kappa) = (5.32144, 0.1665)$.

Incidentally, a formula similar to (4.23) exists also for the pion decay constant f_π.[12] The only difference is that the relative finite size effect is negative and (for $N_f = 2$) four times as large as that of the pion mass:

$$f_\pi(La) = f_\pi \left[1 - 4\xi \sum_{n=1}^{\infty} m(n) \, \frac{K_1(\sqrt{n}\, m_\pi La)}{\sqrt{n}\, m_\pi La} \right]. \tag{4.24}$$

We have already seen that the volume dependence of our pion masses can be accounted for by chiral perturbation theory on the largest lattices at most, and there is no reason to believe that this should be different for the decay constant. We can check, however, whether the relative factor of minus four also holds on smaller lattices. Figures 4.13–4.15 show the volume dependence of the shifts in $f_\pi(La)$ and $m_\pi(La)$ relative to $f_\pi(L_{\max}a)$ and $m_\pi(L_{\max}a)$, respectively, for our three different quark masses. While the finite-size effect of the pion decay constant is indeed negative, its magnitude is, on the smaller lattices at $(\beta, \kappa) = (5.6, 0.1575)$ and $(5.6, 0.158)$, about the same as that of the pion mass shift; on the second largest volume at $(\beta, \kappa) = (5.6, 0.1575)$ the relative shift in $f_\pi(La)$ is about twice as big as the shift in $m_\pi(La)$. Unfortunately at $(\beta, \kappa) = (5.32144, 0.1665)$, corresponding to our smallest quark mass, the statistical basis is too poor to make a definite statement, but on the smallest lattice the relative factor is (at least in terms of magnitude) compatible with 4.

Nucleon

In case of the nucleon mass, replacing the single exponential motivated by the approximation (2.28) by an ansatz corresponding to the full formula (2.22) might be considered as the

[12] Only recently, also an asymptotic formula *à la* Lüscher has been derived for f_π [70].

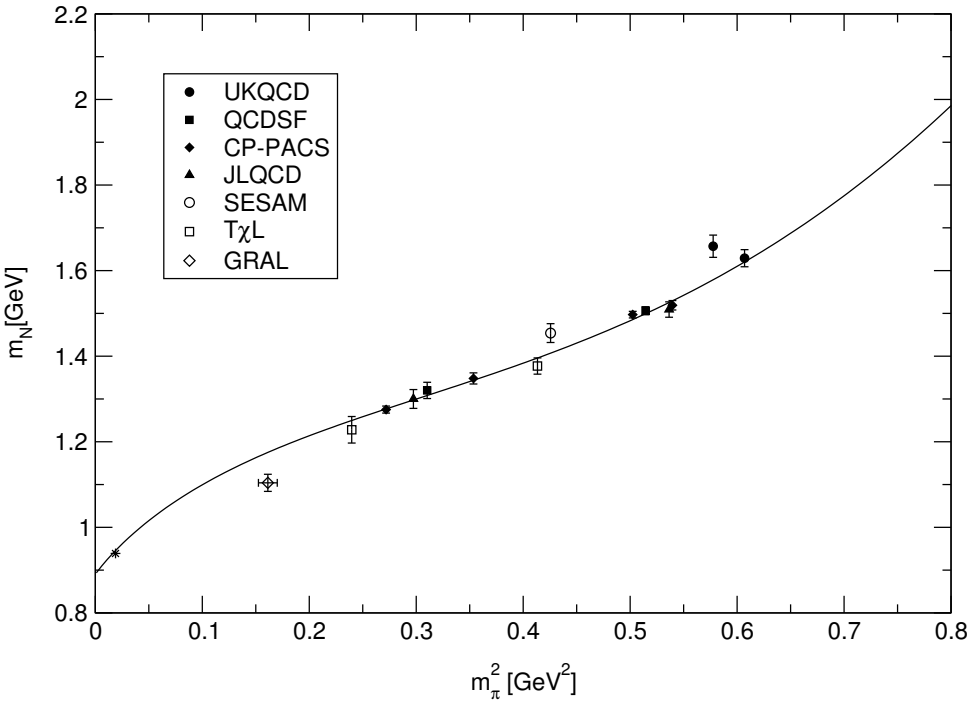

Figure 4.16: Nucleon mass data from various collaborations as a function of $m_\pi^2 \propto m_q$, including our data. All data points are from simulations on relatively large and fine lattices. The curve corresponds to a fit of the data represented by the solid symbols to equation (2.37). Note that the fit result is consistent with the physical pion and nucleon masses (indicated by the star).

next logical step towards a better description of the volume dependence. (Recall that our assumption that Eq. (2.28) is a good approximation of Eq. (2.22) is actually only justified for the physical value of m_π/m_N.) Alternatively one could use the formula (2.22) (or rather the decomposition (2.27)) directly, with the phenomenological value of $g_{\pi N}$ or g_A. However, since Eq. (2.22) is in fact only a special case of the formula (2.35), let us instead confront our data for the nucleon mass directly with the formulae (2.34) and (2.35) from baryon chiral perturbation theory. Following Ref. [66] we fix g_A and f_π to the physical values $g_A = 1.267$, $f_\pi = 92.4\,\mathrm{MeV}$, and set the couplings c_2 and c_3 to $c_2 = 3.2\,\mathrm{GeV}^{-1}$, $c_3 = -3.4\,\mathrm{GeV}^{-1}$. The remaining parameters m_0, c_1 and $e_1^r(\lambda)$ (where the renormalization scale λ is chosen to be 1 GeV) are taken from a fit of data from various unquenched simulations with

$$a < 0.15\,\mathrm{fm}, \quad M_\pi L > 5 \quad \text{and} \quad m_\pi < 800\,\mathrm{MeV} \tag{4.25}$$

to Eq. (2.37). In Ref. [66], data from the UKQCD [38], CP-PACS [39], JLQCD [40] and QCDSF [66] collaborations have been used. These data are plotted in Figure 4.16, complemented with the results from our largest lattices, namely the TχL results at $(5.6, 0.1575, 24)$, $(5.6, 0.158, 24)$ and the GRAL result at $(5.32144, 0.1665, 16)$. We also include the SESAM result at $(\beta, \kappa, L) = (5.6, 0.1575, 16)$. Although the conditions (4.25) are to some extent arbitrary we stick to them for definiteness. Consequently we refrain from repeating the fits of Ref. [66] with our data, because only the TχL point at $(\beta, \kappa, L) = (5.6, 0.1575, 24)$ meets all of the requirements in (4.25). Instead we quote the result of fit 1 in Ref. [66] yielding $m_0 = 0.89(6)\,\mathrm{GeV}$, $c_1 = -0.93(5)\,\mathrm{GeV}^{-1}$ and $e_1^r(\lambda = 1\,\mathrm{GeV}) = 2.8(4)\,\mathrm{GeV}^{-3}$, consistent with phenomenology. The corresponding fit curve is represented by the solid line in Figure 4.16.[13] The fact that the TχL point at $(\beta, \kappa, L) = (5.6, 0.1575, 24)$ lies close to the fit curve without including it into the fit hints to a small $O(a)$ effect at this point. We emphasize here that we use the standard Wilson plaquette and quark action with errors at $O(a)$, whereas the data from the other collaborations have all been generated with $O(a)$ improved actions: UKQCD, QCDSF and JLQCD employ the clover quark action with a non-perturbatively determined improvement parameter c_{SW}, and CP-PACS work with a mean-field improved clover quark action on top of the renormalization-group improved Iwasaki gauge action. The other TχL point at $(\beta, \kappa, L) = (5.6, 0.158, 24)$, corresponding to a smaller pion mass, lies somewhat below the curve. Correcting it for the presumed finite-size effects in the pion and the nucleon mass would shift it even slightly further away from the curve (recall that in this regime of larger L the finite-size effect is bigger for the nucleon than for the pion). The SESAM point at $(\beta, \kappa, L) = (5.6, 0.1575, 16)$ illustrates how finite-size effects show up in such a plot. Correcting it for the finite-size effects in the pion and the nucleon masses (see Table 4.7) would shift it to the lower left, towards the corresponding TχL point with $L = 24$. Our (finite-size corrected) data points generally tend to lie somewhat below the curve, and this is also true for the GRAL point with $(\beta, \kappa) = (5.32144, 0.1665)$. In view of the statistical fluctuations in $m_\pi(La)$ at this parameter set we plot in Figure 4.16 the mean of the respective pion masses at $L = 12, 14, 16$, with a corresponding error bar along the m_π^2 axis. Even with this uncertainty taken into account the deviation of the GRAL point from the fit curve is significant. In view of the relatively low cut-off of only about 1.5 GeV at this point (to be compared to a nucleon mass of 1.1 GeV) we assume that discretization errors are responsible for the deviation. In case of the TχL data cut-off effects are expected to be less important, due to the smaller lattice spacings in these simulations (see Table 4.1).

[13] Strictly speaking, in the fit to equation (2.37) the chiral-limit values of g_A and f_π should be used as input. However, replacing the physical values of g_A and f_π with $g_A^{(0)} = 1.2$ and $f_\pi^{(0)} = 88\,\mathrm{MeV}$ does not alter the fit result significantly. A more detailed error analysis has been attempted in Ref. [132].

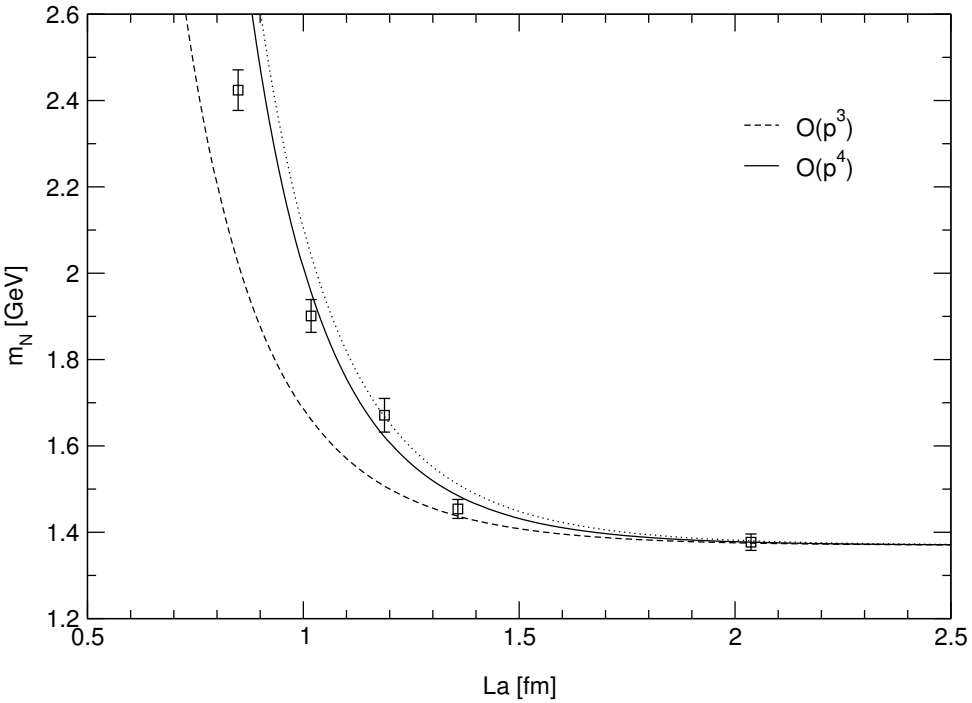

Figure 4.17: Volume dependence of the nucleon mass for $m_\pi = 643\,\mathrm{MeV}$. The dashed curve represents the $O(p^3)$ term only, while the solid curve also includes the $O(p^4)$ contribution. The dotted curve results if the pion mass is reduced by 10% in the $O(p^4)$ formula.

Using the parameters corresponding to the solid curve in Figure 4.16 we can evaluate the finite-size formulae (2.34) and (2.35) and compare the results to our data. Our three sets of simulations with different lattice sizes correspond to pion masses of approximately 643 MeV, 490 MeV and 419 MeV. Note that the latter two masses are even lighter than the lightest of the pion masses investigated in Ref. [66] (732 MeV, 717 MeV and 545 MeV). The curves in Figures 4.17–4.19 have been computed from equations (2.34) and (2.35) with no free parameters. Like in Ref. [66] the solid curves correspond to the $O(p^4)$ prediction

$$m_N(La) = m_N + \Delta_a(La) + \Delta_b(La), \tag{4.26}$$

where m_N has been determined such that the calculated value $m_N(L_{\max}a)$ equals the simulated mass from the largest lattice with $L = L_{\max}$, respectively. Similarly, for the pion masses m_π we also take the simulated value from the largest lattice. For the dotted curve, corresponding to the $O(p^3)$ prediction, the $O(p^4)$ contribution from Δ_b in (4.26) has been left out, while m_N has been left unchanged. For all our pion masses we find a remarkably good overall description of our data by the $O(p^4)$ prediction down to lattice sizes of about 1 fm. Replacing m_π from the largest, $L = 16$ lattice at $(\beta, \kappa) = (5.32144, 0.1665)$ by the mean of the pion masses from the $L = 12, 14, 16$ lattices (as we have done in the context of Figure 4.16) does not lead to a significant difference in the resulting curve. Since both the statistical and the theoretical error of the simulated $m_N(La)$ are smallest for the largest lattice, we consider the $O(p^4)$ finite-size corrected nucleon mass

$$\tilde{m}_N(La) = m_N(La) - \Delta_a(La) - \Delta_b(La), \tag{4.27}$$

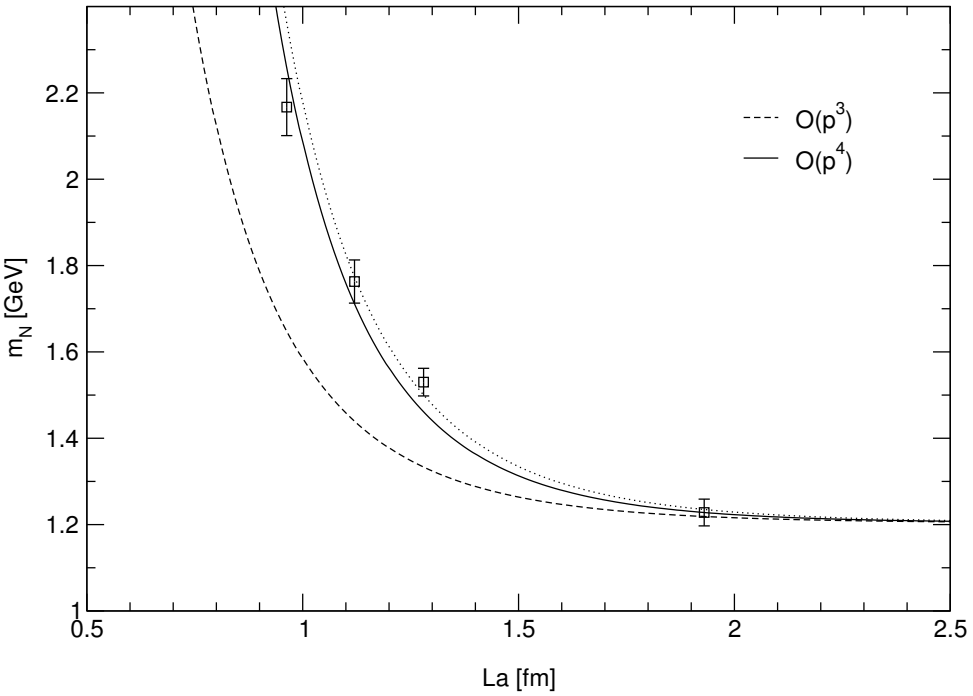

Figure 4.18: Same as Figure 4.17 for $m_\pi = 490\,\mathrm{MeV}$.

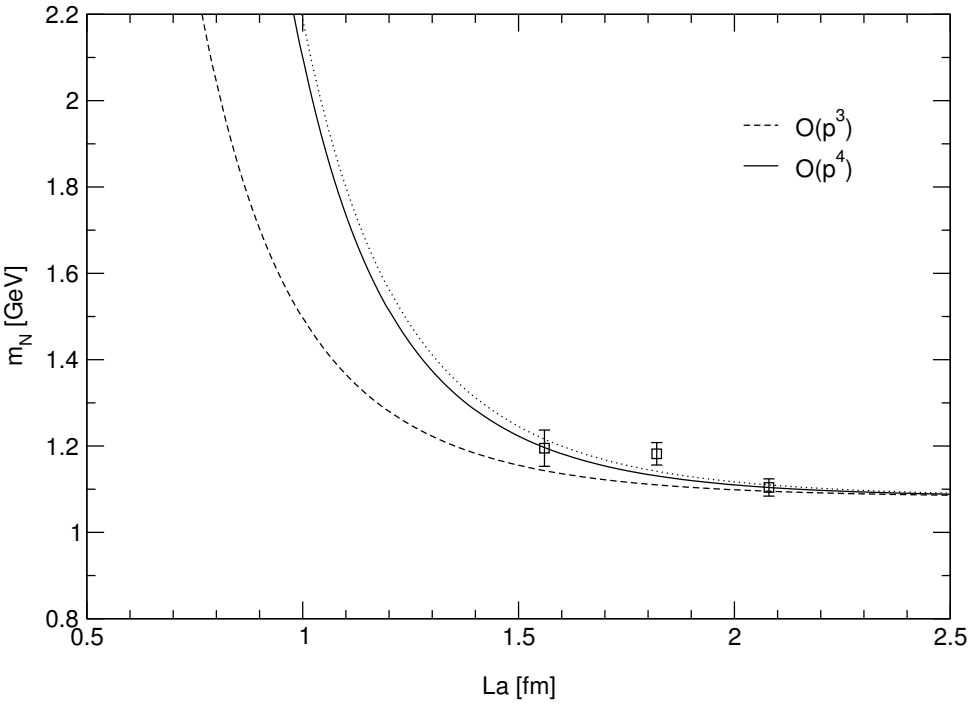

Figure 4.19: Same as Figure 4.17 for $m_\pi = 419\,\mathrm{MeV}$.

β	κ_{sea}	m_{PS} [GeV]	$\tilde{m}_N(L_{\max}a)$ [GeV]	$m_N(L_{\max}a)$ [GeV]	Δ
5.6	0.1575	0.6429(67)	1.370(19)	1.377(19)	0.53%
	0.1580	0.4896(94)	1.204(31)	1.228(31)	2.02%
5.32144	0.1665	0.4188(75)	1.081(20)	1.104(20)	2.08%

Table 4.11: Finite-size shift of the nucleon mass on the largest lattice, respectively, as inferred from Eq. (4.26). $\Delta = (m_N - \tilde{m}_N)/\tilde{m}_N$ is the relative deviation of the Monte Carlo value m_N from the shifted mass $\tilde{m}_N = m_N - \Delta_a - \Delta_b$ (all values to be taken at $L_{\max}a$). We believe $\tilde{m}_N(L_{\max}a)$ to be our best estimate of the true asymptotic mass.

taken at $L = L_{\max}$, as our best estimate of the asymptotic nucleon mass. Table 4.11 shows the predicted infinite-volume masses for our simulations. The last column gives the relative mass shift on the largest lattice, respectively. Just as it was the case for the pion, the finite size effect in the nucleon at $(\beta, \kappa, L) = (5.6, 0.1575, 24)$ is considerably smaller than the statistical uncertainty. On the other hand, at $(\beta, \kappa, L) = (5.6, 0.158, 24)$ and $(5.32144, 0.1665, 16)$ the finite-size effects amount to about 2% of the respective asymptotic mass, which is comparable to the statistical errors.

How can these findings be used in practice? We have seen previously that our nucleon data can be fitted quite well to a simple exponential ansatz, with the corresponding asymptotic pion mass as input. Moreover, in the case of our simulations at $(\beta, \kappa) = (5.6, 0.1575)$, where the finite-size effects in the masses from the second largest lattice are already of the order of a few percent only, it was even possible to reproduce the large-volume nucleon mass by an extrapolation. Although the asymptotic pion mass that we need as input for the fit of the nucleon mass generally comes out too small when it is estimated on the basis of the smaller volumes alone, the extrapolation of the nucleon mass is not so much affected by this, as even with this smaller value as input it works remarkably well. This is, however, a purely empirical result, the caveats being that we have no control over the error, and that we need data from several volumes (at least three) before we can have some confidence in the extrapolation. The fact that the $O(p^4)$ formula (4.26) describes our Monte Carlo data so well without any free parameters opens up a more direct way to estimate the asymptotic nucleon mass. Once we have convinced ourselves that we are in a parameter regime where the formula applies, we can directly calculate the amount by which we have to shift the nucleon mass in order to compensate for the finite-size effect associated with the given volume. Our simulations together with the results of Ref. [66] suggest that at least for asymptotic pion masses larger than 400 MeV the formula provides a good description of the nucleon mass data down to physical lattice sizes of approximately 1 fm. For a direct calculation of the finite-size shift in the nucleon mass one needs to know the pion mass in infinite volume, however. If one is already in a parameter regime where the finite-size effect in the pion mass is small (of the order of a few percent) one may apply the results of Ref. [65] to obtain an estimate of the asymptotic pion mass. If this is not the case one can still revert to a "naive" exponential fit (provided that the pion mass is known for more than two different volumes) and extrapolate. Since we have learned that a naive extrapolation systematically underestimates the true pion mass in infinite volume we illustrate, as an example, the impact of a 10% smaller pion mass by the dotted curves in Figures 4.17–4.19. Although in relation to the very shift the systematic error associated with the pion mass grows with L, its absolute value becomes less and less significant compared to the statistical uncertainties of the data. This means, on the one hand, that (assuming the formula to exactly reproduce the volume dependence of the data

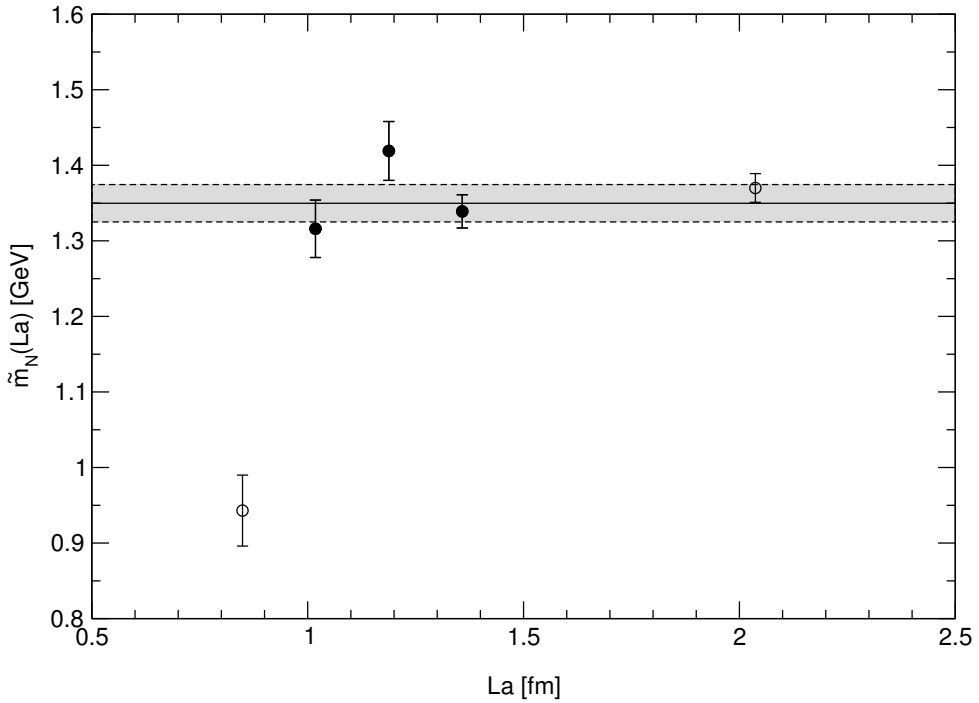

Figure 4.20: Finite-size corrected nucleon masses for $m_\pi = 643\,\mathrm{MeV}$. The solid line results from a fit of the data represented by the solid symbols. The gray band indicates the error associated with the fit.

and the statistical uncertainties to be all of comparable size) in order to predict the asymptotic nucleon mass correctly (within the statistical errors) one needs to know m_π the more accurately the smaller the physical size of the largest available lattice. On the other hand it means that if L is sufficiently large so that one can reliably extrapolate the pion mass, the asymptotic nucleon mass can also be determined quite accurately.

While the formula (4.26) can already be used to estimate the asymptotic nucleon mass on the basis of a single lattice, one can of course also combine data from several lattice volumes to obtain a more reliable prediction. Figures 4.20–4.22 show our finite-size corrected nucleon masses $\tilde{m}_N(La)$ for the simulated lattice volumes and pion masses. The solid lines correspond to fits of the corrected masses in the range $0.9\,\mathrm{fm} \lesssim La \lesssim 1.9\,\mathrm{fm}$ (solid symbols) to a constant, $\tilde{m}_N^{\mathrm{fit}}$, leaving out the largest available lattice, respectively.[14] The associated uncertainties (from the fit) are indicated by the gray error bands. Table 4.12 shows the values of $\tilde{m}_N^{\mathrm{fit}}$ resulting from these fits and their deviation from the corrected nucleon mass as obtained on the largest lattice, respectively. Both the plots and the table show that—within errors—the extrapolations are consistent with the corrected values from the largest lattices. The relative deviations Δ are comparable in size to the deviations we found for the "naive" extrapolations ($\Delta(L=\infty)$ in Tables D.13 and D.14), but using the formula (4.26) we have, in principle, a much better control over the involved uncertainties.

[14] Alternatively, one could directly fit the unshifted data to Eq. (4.26), with m_N as a free parameter.

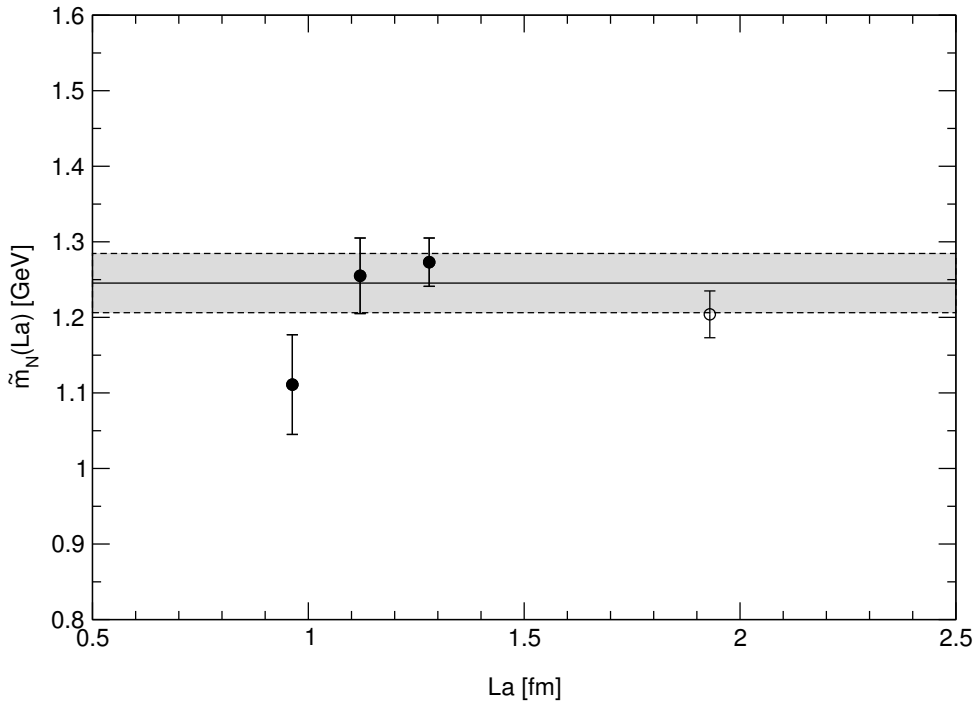

Figure 4.21: Same as Figure 4.20 for $m_\pi = 490\,\mathrm{MeV}$.

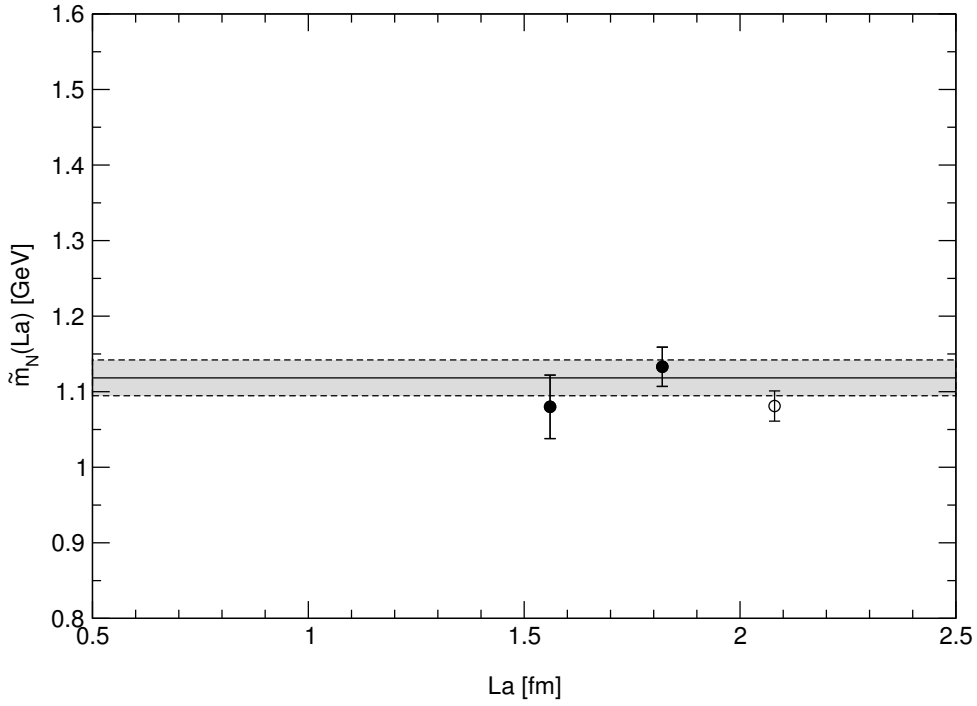

Figure 4.22: Same as Figure 4.20 for $m_\pi = 419\,\mathrm{MeV}$.

β	$\kappa_{\rm sea}$	$m_{\rm PS}$ [GeV]	$\tilde{m}_N(L_{\rm max}a)$ [GeV]	$\tilde{m}_N^{\rm fit}$ [GeV]	Δ
5.6	0.1575	0.6429(67)	1.370(19)	1.350(25)	-1.5%
	0.1580	0.4896(94)	1.204(31)	1.245(39)	4.1%
5.32144	0.1665	0.4188(75)	1.081(20)	1.118(24)	3.4%

Table 4.12: Estimates of the asymptotic nucleon masses without taking the largest lattice, respectively, into account. The $\tilde{m}_N^{\rm fit}$ values result from fits of the corrected nucleon masses $\tilde{m}_N(La)$ in the range $0.9\,{\rm fm} \lesssim La \lesssim 1.9\,{\rm fm}$ to a constant. $\Delta = (\tilde{m}_N^{\rm fit} - \tilde{m}_N(L_{\rm max}a))/\tilde{m}_N(L_{\rm max}a)$ gives the relative deviation of these estimates from the finite-size corrected values $\tilde{m}_N(L_{\rm max}a)$, which we believe to be the best estimates of the true asymptotic values.

4.5 Discretization Errors

One way to check on the importance of $O(a)$ lattice artefacts in our simulations is to consider the PCAC relation

$$\partial_\mu A_\mu^a(x) = 2mP^a(x) \tag{4.28}$$

between the isovector axial current

$$A_\mu^a(x) = \overline{q}(x)\gamma_\mu\gamma_5\frac{1}{2}\tau^a q(x) \tag{4.29}$$

and the associated density

$$P^a(x) = \overline{q}(x)\gamma_5\frac{1}{2}\tau^a q(x), \tag{4.30}$$

where τ^a denotes a Pauli matrix acting on the flavor indices of the quark fields q. On the lattice, the bare quark mass $Z_q a m_q$ can be extracted from ratios of correlation functions,

$$Z_q a m_q = \frac{1}{2}\frac{\left\langle \partial_\mu A_\mu^a(x) J^a \right\rangle}{\left\langle P^a(x) J^a \right\rangle} + O(a), \tag{4.31}$$

where the (smeared) source J^a is a suitable polynomial in the quark and gluon fields, and $Z_q = Z_P/Z_A$. The PCAC relation (4.28) is an operator identity that holds for the Wilson action up to $O(a)$ effects. Consequently, its lattice version holds—up to those effects—for any choice of boundary conditions, source operators and lattice sizes. This means in particular that at fixed β and κ any residual lattice size dependence of the PCAC quark mass (4.31) must be a lattice artefact. Figures 4.23–4.25 show the volume dependence of the relative deviation of the PCAC quark mass $m_q(La)$ from its value m_q on the largest lattices, for our three (β, κ) combinations.

We find that at $(\beta, \kappa) = (5.6, 0.1575)$ the discretization errors appear to be small for $La \gtrsim 1\,{\rm fm}$, while for $(\beta, \kappa) = (5.6, 0.158)$ and $(5.32144, 0.1665)$ they are small only for $La \gtrsim 1.3\,{\rm fm}$ and $La \gtrsim 1.8\,{\rm fm}$, respectively. On the smaller lattices the cut-off shows up in quark mass shifts of 20–40% (with large error bars on the smallest lattices). The fact that the cut-off effects are small for $(\beta, \kappa) = (5.6, 0.1575)$ and somewhat larger for $(\beta, \kappa) = (5.6, 0.158)$ and $(5.32144, 0.1665)$ is consistent with our observations in the previous section. In Figure 4.16 we saw no significant lattice artifacts in the nucleon mass for $m_\pi = 643\,{\rm MeV}$, while for $m_\pi = 490\,{\rm MeV}$ and $m_\pi = 419\,{\rm MeV}$ the nucleon mass displayed some deviation from the curve (which was obtained from a fit to $O(a)$ improved data).

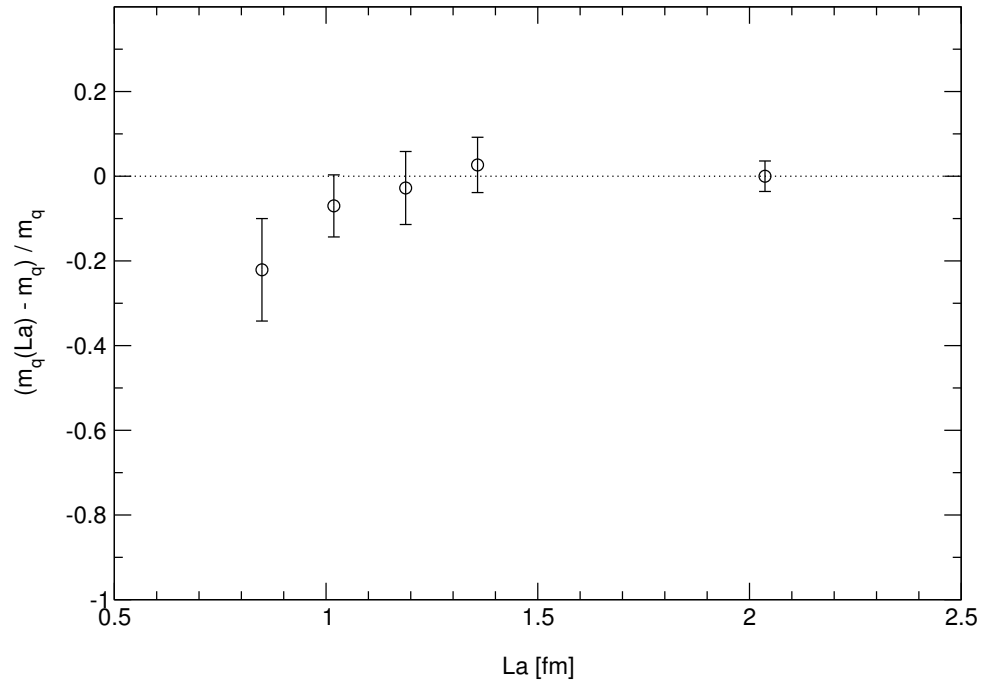

Figure 4.23: Box-size dependence of the relative shift in the PCAC quark mass at $(\beta, \kappa) = (5.6, 0.1575)$.

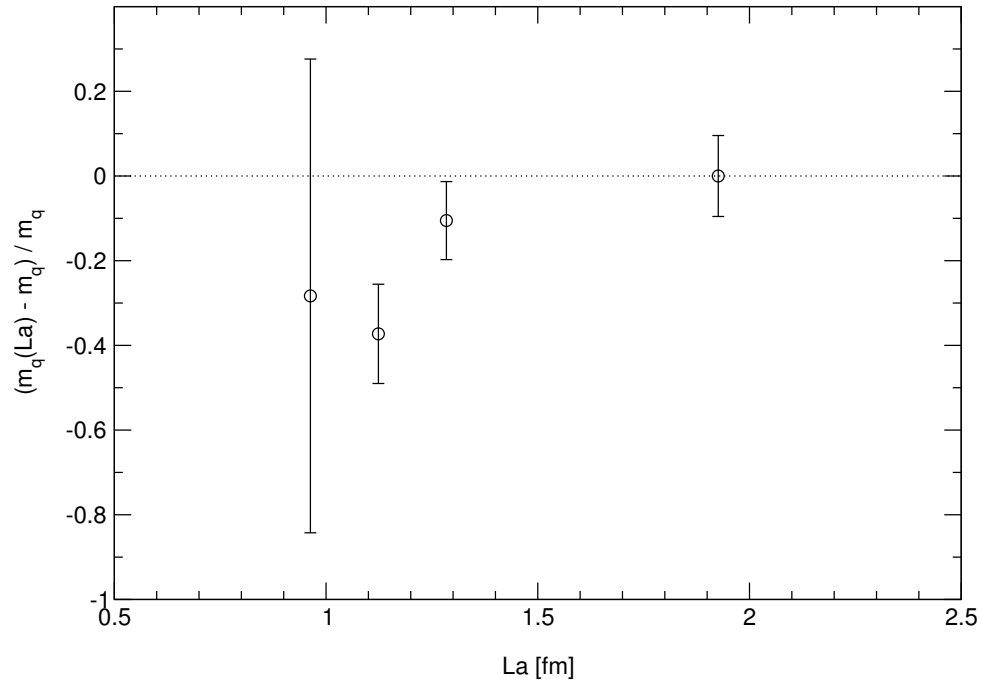

Figure 4.24: Same as Figure 4.23 for $(\beta, \kappa) = (5.6, 0.158)$.

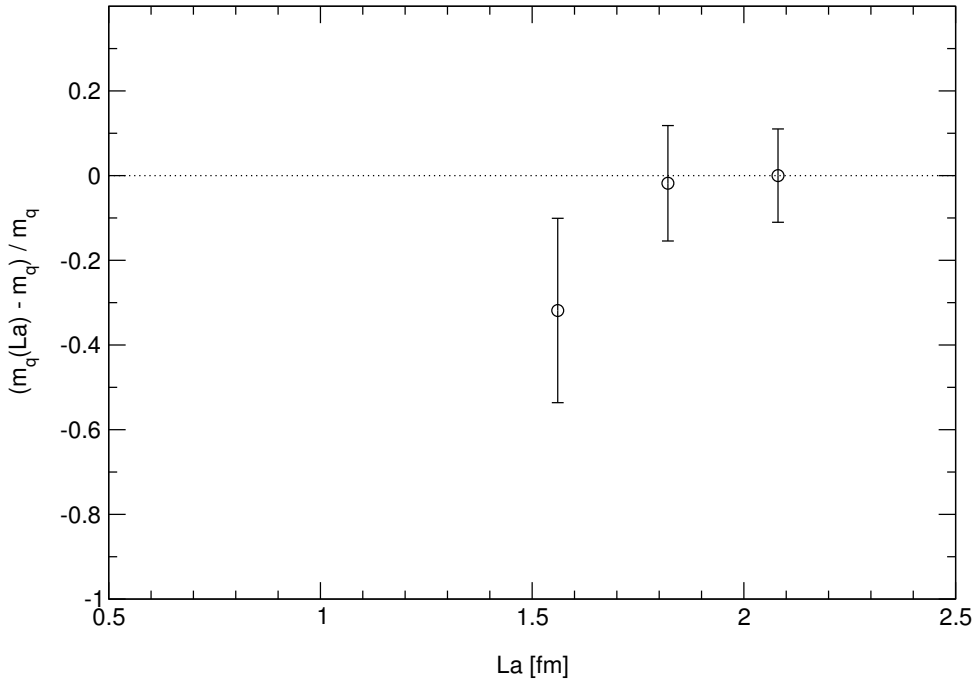

Figure 4.25: Same as Figure 4.23 for $(\beta, \kappa) = (5.32144, 0.1665)$.

Summary and Conclusions

In this work we have investigated finite-size effects in light hadron masses as obtained from lattice QCD simulations with two degenerate flavors of dynamical Wilson fermions. We have complemented previous SESAM/TχL simulations at quark masses corresponding roughly to 85 and 50% of the strange quark mass with several runs at the same values of β and κ, but on smaller lattices. In addition we have carried out exploratory simulations with three different lattice volumes at a stronger coupling of $\beta = 5.32144$ in order to push our analysis towards the regime of lighter quark masses. We have succeeded in simulating near $m_s/3$, which in terms of m_π/m_ρ is very close to the rho decay threshold of 0.5. The physical extent of the investigated lattices ranges between 0.85 fm and 2.04 fm.

The gauge field configurations investigated in this work were produced on APE machines at DESY Zeuthen and the cluster computer ALiCE at the University of Wuppertal. While on APE we have used the readily available Hybrid Monte Carlo code from the SESAM collaboration (with some modifications for APEmille), on ALiCE a new HMC code was employed. For all of the new production runs we have measured the computational cost and the autocorrelation times of the mean plaquette and average number of solver iterations. We have found that at $\beta = 5.32144$ statistical fluctuations are quite large and zero modes start playing a role on the smaller volumes (12^3 and 14^3). This is reflected in rather long autocorrelation times. The simulation on a 16^3 lattice, however, is less affected by such problems, and we have not observed any severe instabilities in the molecular dynamics part of the updating process at this lattice size.

While in this work we have focused on the symmetric case $\kappa_{\mathrm{val}} = \kappa_{\mathrm{sea}}$ we have calculated, for subsets of the new gauge field ensembles, quark propagators and hadronic correlation functions for up to six different valence quark masses per given sea quark mass. In a further step these can be used for partially quenched analyses. For source and sink smearing we have adapted the previously determined parameters for the Wuppertal smearing method to the smaller volumes used in this work. Hadron masses and amplitudes of correlation functions have been obtained by fits of the local-smeared and smeared-smeared correlators, with correlations between time-slices and among configurations taken into account.

We have determined the Sommer radius r_0 for the largest lattice at $\beta = 5.32144$ from a fit of our data for the static quark potential to a "Coulomb + linear" ansatz. Although our general conclusions do not depend on this, a possible improvement at this point could be to include a lattice correction to the Coulomb term in order to account for the violation of rotational invariance at small distances due to the relatively large lattice spacing. As a qualitative check on whether the simulated system remains in the zero-temperature phase of QCD as the lattice size is decreased we have monitored the distributions and means of the Polyakov loops for all investigated parameter sets. Only on the smallest lattice for the heavier quark mass at $\beta = 5.6$ is a deviation from the expected, approximately point-symmetric distribution around zero clearly

visible. Using the data from all simulated volumes we have addressed the question to what extent the volume dependence of the computed pion, rho and nucleon masses can be parameterized by simple functions, and if an extrapolation from small and intermediate lattices to the infinite volume is possible. To this end we have compared an exponential ansatz motivated by Lüscher's formula to the power law observed by Fukugita *et al.*. On the basis of various fits we conclude that while the power law may be used to describe the volume dependence of the masses at small volumes smaller than roughly 1.5 fm, over the full range of simulated lattices and in particular with respect to the asymptotic behavior the exponential ansatz is superior. The extrapolation of simple exponential fits to the infinite volume in general provides only a lower bound to the asymptotic mass, but this bound may be close to the true asymptotic value if the relative difference between the masses from the largest volumes incorporated in the fit is already quite small (of the order of a few percent). For small volumes alone, however, this is in general not the case.

The simple exponential parameterization corresponds in its functional form to the asymptotic Lüscher formula for the pion (with input from leading order ChPT in infinite volume). Although empirically we have found that the single exponential allows for a good description of our light hadron masses over a wide range of lattice volumes, a large coefficient multiplying the exponential attests to the fact that the data points from the small lattices lie outside the parameter regime in which the formula holds. We have illustrated this by a comparison of our pion mass data to Lüscher's formula with input from continuum ChPT up to NNLO and to the full LO ChPT result for the pion mass in finite volume. Of course, if a reliable analytic prediction with controllable errors is available it is always preferable to an extrapolation based on a fit with free parameters. We have shown, however, that in the parameter regime of our simulations even the best currently available estimate for the pion finite-size effect, based on a combination of the asymptotic Lüscher formula with NNLO ChPT input and the full (but LO) ChPT result, yields mass shifts of a few percent only. This is comparable in size to the typical statistical errors and therefore hard to detect in practice. Our simulations at $\beta = 5.32144$ probably are in a pion mass regime where the box-size dependence can be described by such a formula, but more statistics would be needed to corroborate this assumption. While Lüscher's formula with input at next-to-leading and next-to-next-to-leading order in ChPT can be used to control the convergence of the chiral expansion, a full higher order result from ChPT for the pion mass in finite volume would be useful to fully assess the role of the sub-leading terms in the large-L expansion.

For the nucleon, a full finite-size mass formula from relativistic baryon ChPT up to NNLO has recently become available. We have shown for three different pion masses (two of which are smaller than the ones considered in Ref. [66]) that it describes our simulated nucleon masses remarkably well even down to box-sizes of about 1 fm. We have also seen that above this size it can, in principle, be used to estimate the infinite-volume mass already on the basis of a single measurement, provided that the asymptotic pion mass is known. If, as in our case, data from several lattice volumes are available, they can be combined to obtain a reliable estimate with controllable errors. We could thus corroborate and extend the findings of Ali Khan *et al.*.

Perspectives

In view of our original goal, "Going Realistic And Light", an important result of this work is that simulations with Wilson quarks at a relatively light quark mass are feasible. Statistical fluctuations and autocorrelation times are under control if the chosen lattice size is not chosen

too small. The same holds true for the performance of the HMC algorithm if the integration step size in the molecular dynamics updates is adequately small. Since with currently available formulae reliable extrapolations from small volumes to the infinite volume are problematic at least in the case of the pion, we suggest to simulate on lattices so large that the pion masses computed on two different volumes differ only by a few percent and the results of Ref. [65] can be applied. The finite-size corrected pion mass can then be used as input for an estimate of the asymptotic nucleon mass. As we have demonstrated with our simulations at $\beta = 5.32144$, even with a moderate number of lattice sites we can make the physical volume large enough to accommodate a relatively light pion by choosing the gauge coupling (and thus the lattice spacing) appropriately. Incidentally, such an approach has also been chosen by the qq+q collaboration. Using a large lattice spacing may of course lead to large discretization errors, which for our unimproved Wilson action are $O(a)$. While at our smallest pion mass we have observed an effect in the nucleon mass that might be due to the low lattice cut-off at this point, one generally expects the cut-off effect to be less severe for low-energy quantities like the pion mass and decay constant. This assumption is supported by results from the qq+q collaboration. Considering the volume-independent PCAC quark mass we observe potentially large lattice artefacts on the small lattices, but see no indication of significant $O(a)$ effects on the larger lattices.

As the GRAL project builds on and extends the previous SESAM and TχL projects we have concentrated in this work on the original, unimproved $N_f = 2$ Wilson action. We do believe, however, that our results may also be interesting for upcoming full QCD simulations with chiral fermions. Using the overlap formalism with dynamical quarks, for example, is computationally still extremely expensive and will for a foreseeable time be restricted to rather small volumes. A—possibly naive—extrapolation in the volume may in such simulations be the only way to extract approximate infinite-volume results.

In the light of our findings at $(\beta, \kappa) = (5.32144, 0.1665)$, the next steps towards the regime of lighter quark masses with the Wilson action could be the following (see also Ref. [51]): First, simulate at the same β, but with a larger hopping parameter of $\kappa = 0.1673$ (say). This particular value should yield a quark mass well below $m_\pi/m_\rho = 0.4$. A first run can be conducted with a lattice of size $L = 16$, corresponding to a physical lattice extent of approximately 2 fm. Although for $\kappa = 0.1665$ we have observed no significant finite-size effects at this size, we expect them to become more pronounced as the quark mass is decreased. As long as there is no sub-asymptotic formula for the pion mass-shift in finite volume that would allow for a reliable direct correction of the calculated pion mass (and, then, also of the nucleon mass), at least one other run with, for example, $L = 18$ ($La \approx 2.35\,\mathrm{fm}$) or $L = 20$ ($La \approx 2.6\,\mathrm{fm}$) is needed to learn about the actual magnitude of finite-size effects. (The alternative of simulating a smaller volume of $L = 14$, for example, appears less favorable due to the expected increase in fluctuations.) Depending on the outcome one may then deal with these effects as explained in this work. In a second step, further (intermediate or even smaller) quark masses at $\beta = 5.32144$ can be simulated to set the stage for a chiral extrapolation, preferably using WChPT to account for the finite lattice spacing. The UKQCD and JLQCD collaborations have pointed out ways of dealing with potential instabilities in the updating process with the HMC that are expected to occur along the road (64 bit arithmetic for field storage and matrix vector-multiplications, smaller integration step size, improvement of the BiCGStab solver). Finally, in view of the fact that we are using an unimproved action at a relatively large lattice spacing, as a third step one might attempt a scaling analysis by going to larger values of β and, thus, smaller values of a.

To give a rough estimate of the computational cost of such a program we refer to our simulation at $(\beta, \kappa) = (5.32144, 0.1665)$ with $L = 16$ and $m_\pi/m_\rho \approx 0.55$, where the cost for producing 6700

gauge field configurations in thermal equilibrium was approximately 75 Tflops-hrs. If we assume the cost to scale like $(m_\pi/m_\rho)^{-z}$ with $z = 6$ we arrive at an increase by a factor of 6.8 in going from $m_\pi/m_\rho = 0.55$ to 0.4. In addition, relative factors of 1.8 or 3 must be taken into account in switching from a $16^3 \times 32$ to a $18^3 \times 36$ or $20^3 \times 40$ lattice (assuming the cost to behave like L^5, and $T = 2L$). This increase in effort (a factor of 12–20) is matched by the current increase in available computing time. For example, the next-generation cluster computer ALiCEnext at the University of Wuppertal will very soon provide at least 20 times more compute power than its predecessor ALiCE (roughly a factor of two on a per-node basis, and with 1024 processors about ten times as many nodes), while the IBM p690 installation at FZ Jülich already delivers 50 times the performance of ALiCE (5.6 Tflops from the LINPACK benchmark). Although these numbers provide only hints as to the real performance of our HMC code on these machines, we conclude that the regime of lighter quark masses is within reach, even with the standard Wilson action.

Appendix A

Conventions

A.1 $SU(3)$ Generators

The Hermitian generators t^a, $a = 1, \ldots, 8$, of the Lie group $SU(3)$ satisfy the commutation relations

$$[t^a, t^b] = i f^{abc} t^c. \tag{A.1}$$

The numbers f^{abc} are called *structure constants*. Together with their commutation relations and the *Jacobi identity*,

$$[t^a, [t^b, t^c]] + [t^b, [t^c, t^a]] + [t^c, [t^a, t^b]] = 0, \tag{A.2}$$

the group generators t^a define a Lie algebra. They are conventionally written in terms of the Gell-Mann matrices:

$$\begin{aligned}
\lambda_1 &= \begin{pmatrix} 0 & 1 & 0 \\ 1 & 0 & 0 \\ 0 & 0 & 0 \end{pmatrix}, \quad \lambda_2 = \begin{pmatrix} 0 & -i & 0 \\ i & 0 & 0 \\ 0 & 0 & 0 \end{pmatrix}, \quad \lambda_3 = \begin{pmatrix} 1 & 0 & 0 \\ 0 & -1 & 0 \\ 0 & 0 & 0 \end{pmatrix}, \\
\lambda_4 &= \begin{pmatrix} 0 & 0 & 1 \\ 0 & 0 & 0 \\ 1 & 0 & 0 \end{pmatrix}, \quad \lambda_5 = \begin{pmatrix} 0 & 0 & -i \\ 0 & 0 & 0 \\ i & 0 & 0 \end{pmatrix}, \\
\lambda_6 &= \begin{pmatrix} 0 & 0 & 0 \\ 0 & 0 & 1 \\ 0 & 1 & 0 \end{pmatrix}, \quad \lambda_7 = \begin{pmatrix} 0 & 0 & 0 \\ 0 & 0 & -i \\ 0 & i & 0 \end{pmatrix}, \quad \lambda_8 = \frac{1}{\sqrt{3}} \begin{pmatrix} 1 & 0 & 0 \\ 0 & 1 & 0 \\ 0 & 0 & -2 \end{pmatrix}.
\end{aligned} \tag{A.3}$$

These matrices are normalized so that $\mathrm{Tr}\, \lambda_i \lambda_j = 2\delta_{ij}$.

A.2 Euclidean Gamma Matrices

We use the following representation of the Euclidean gamma matrices:

$$\gamma_1 = \begin{pmatrix} 0 & 0 & 0 & i \\ 0 & 0 & i & 0 \\ 0 & -i & 0 & 0 \\ -i & 0 & 0 & 0 \end{pmatrix}, \quad \gamma_2 = \begin{pmatrix} 0 & 0 & 0 & 1 \\ 0 & 0 & -1 & 0 \\ 0 & -1 & 0 & 0 \\ 1 & 0 & 0 & 0 \end{pmatrix},$$
$$\gamma_3 = \begin{pmatrix} 0 & 0 & i & 0 \\ 0 & 0 & 0 & -i \\ -i & 0 & 0 & 0 \\ 0 & i & 0 & 0 \end{pmatrix}, \quad \gamma_4 = \begin{pmatrix} 1 & 0 & 0 & 0 \\ 0 & 1 & 0 & 0 \\ 0 & 0 & -1 & 0 \\ 0 & 0 & 0 & -1 \end{pmatrix} \tag{A.4}$$

and

$$\gamma_5 \equiv \prod_\mu \gamma_\mu = \begin{pmatrix} 0 & 0 & 1 & 0 \\ 0 & 0 & 0 & 1 \\ 1 & 0 & 0 & 0 \\ 0 & 1 & 0 & 0 \end{pmatrix}. \tag{A.5}$$

Appendix B

Time Series and Autocorrelation Analysis

The plots on the following pages show (from top left to bottom right, respectively) the time series of the average plaquette value and number of solver iterations, the respective normalized autocorrelation functions and the corresponding integrated autocorrelation times as functions of T_{cut}. The inset graphs show, on a logarithmic scale, the exponential fits from which we have extracted the exponential autocorrelation time defined in Eq. (3.6). For all analyses in this work only configurations right from the vertical line in the upper two plots were used. The vertical lines in the upper two plots indicate the respective mean value and standard error. The results of the autocorrelation analysis are summarized and discussed in Section 3.2.

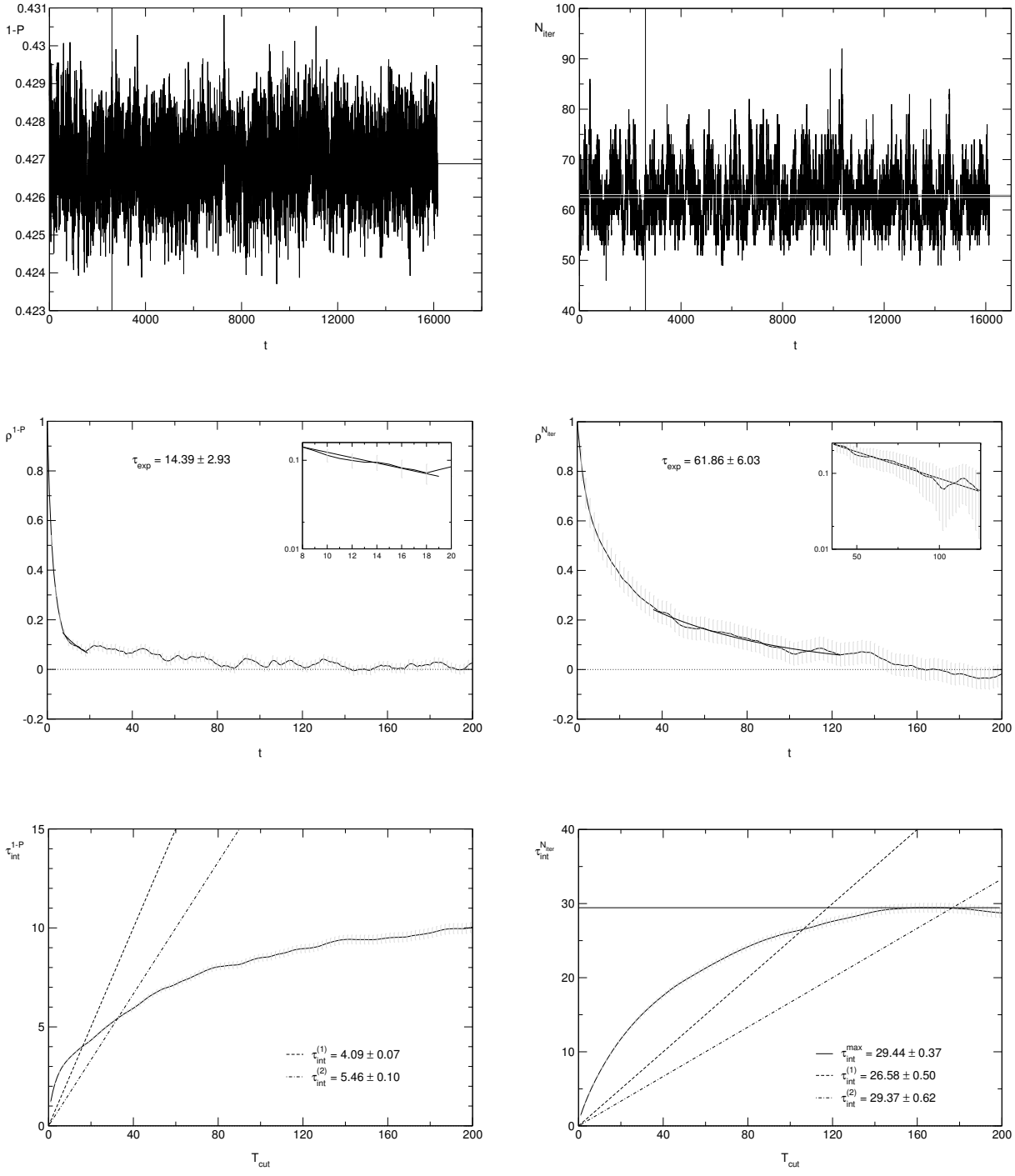

Figure B.1: $(\beta, \kappa, L) = (5.6, 0.1575, 10)$.

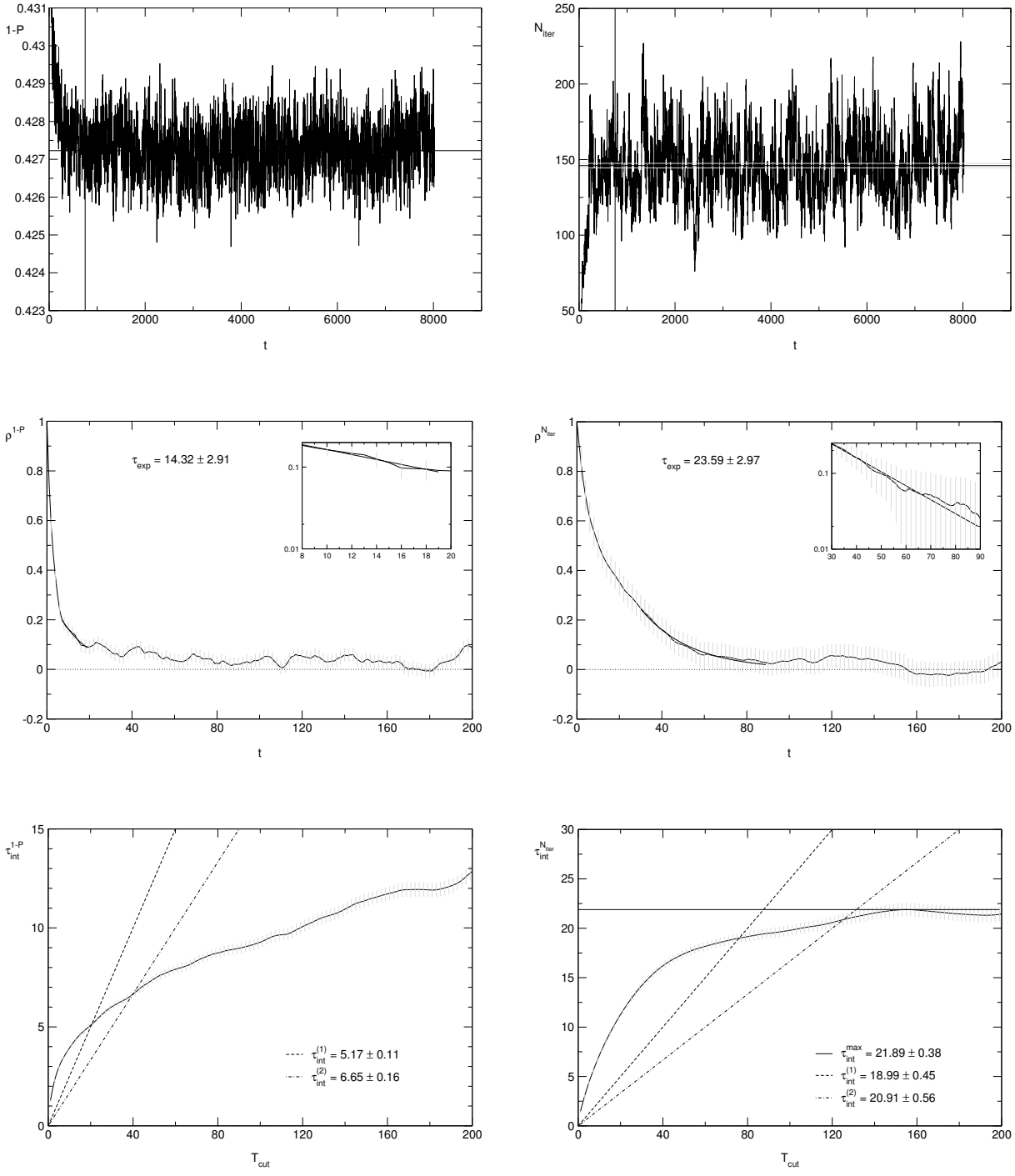

Figure B.2: $(\beta, \kappa, L) = (5.6, 0.1575, 12)$.

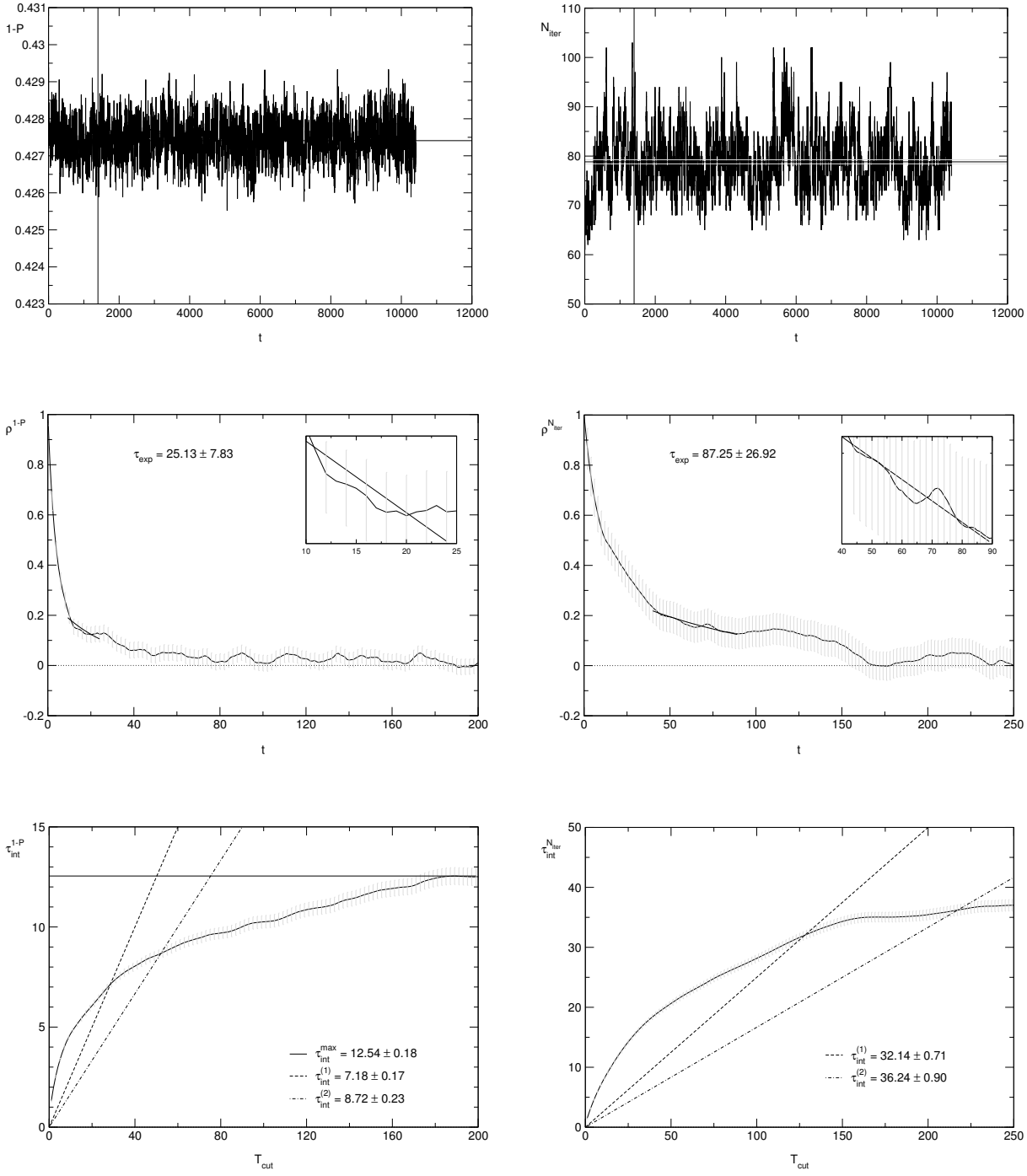

Figure B.3: $(\beta, \kappa, L) = (5.6, 0.1575, 14)$.

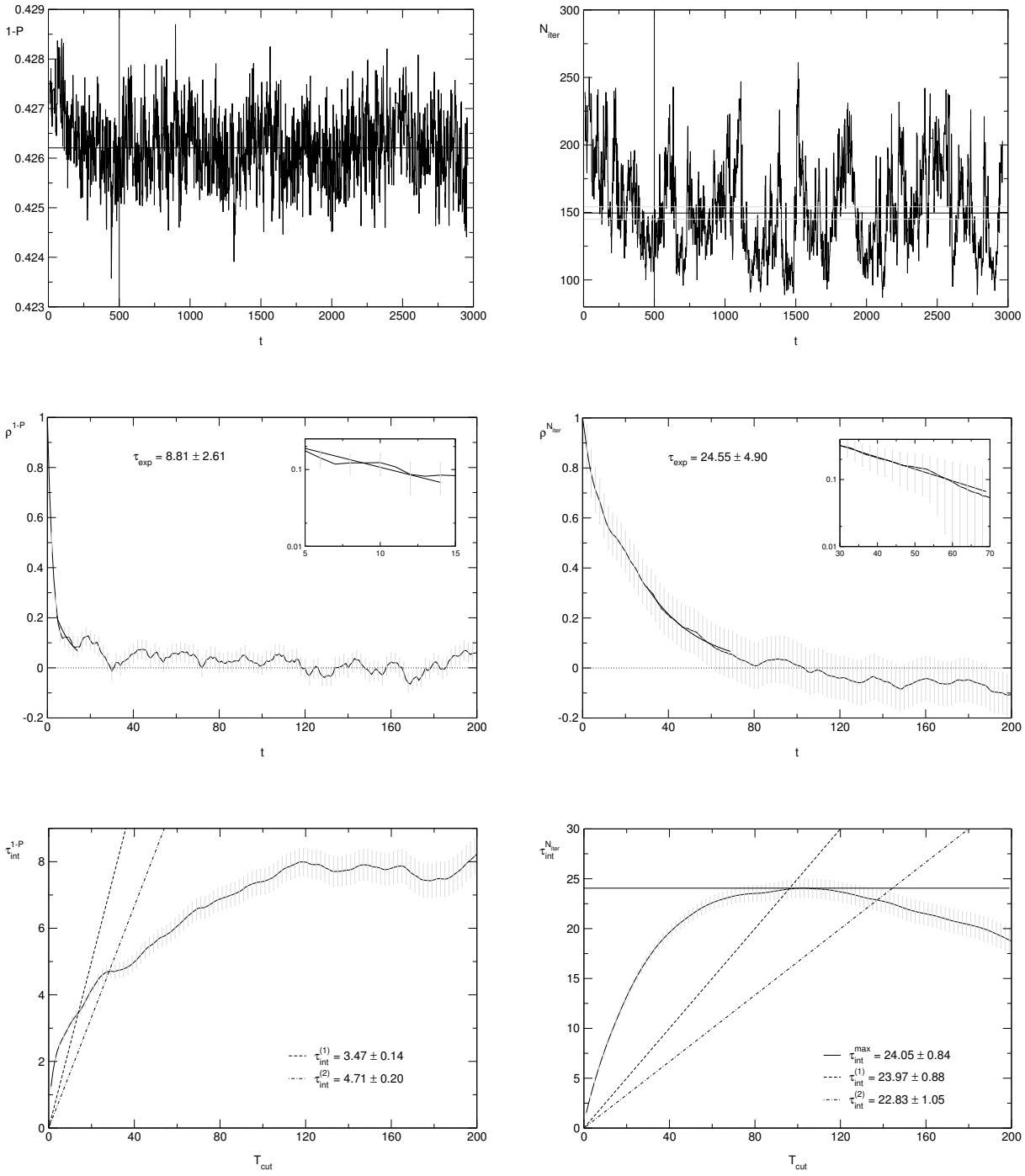

Figure B.4: $(\beta, \kappa, L) = (5.6, 0.158, 12)$.

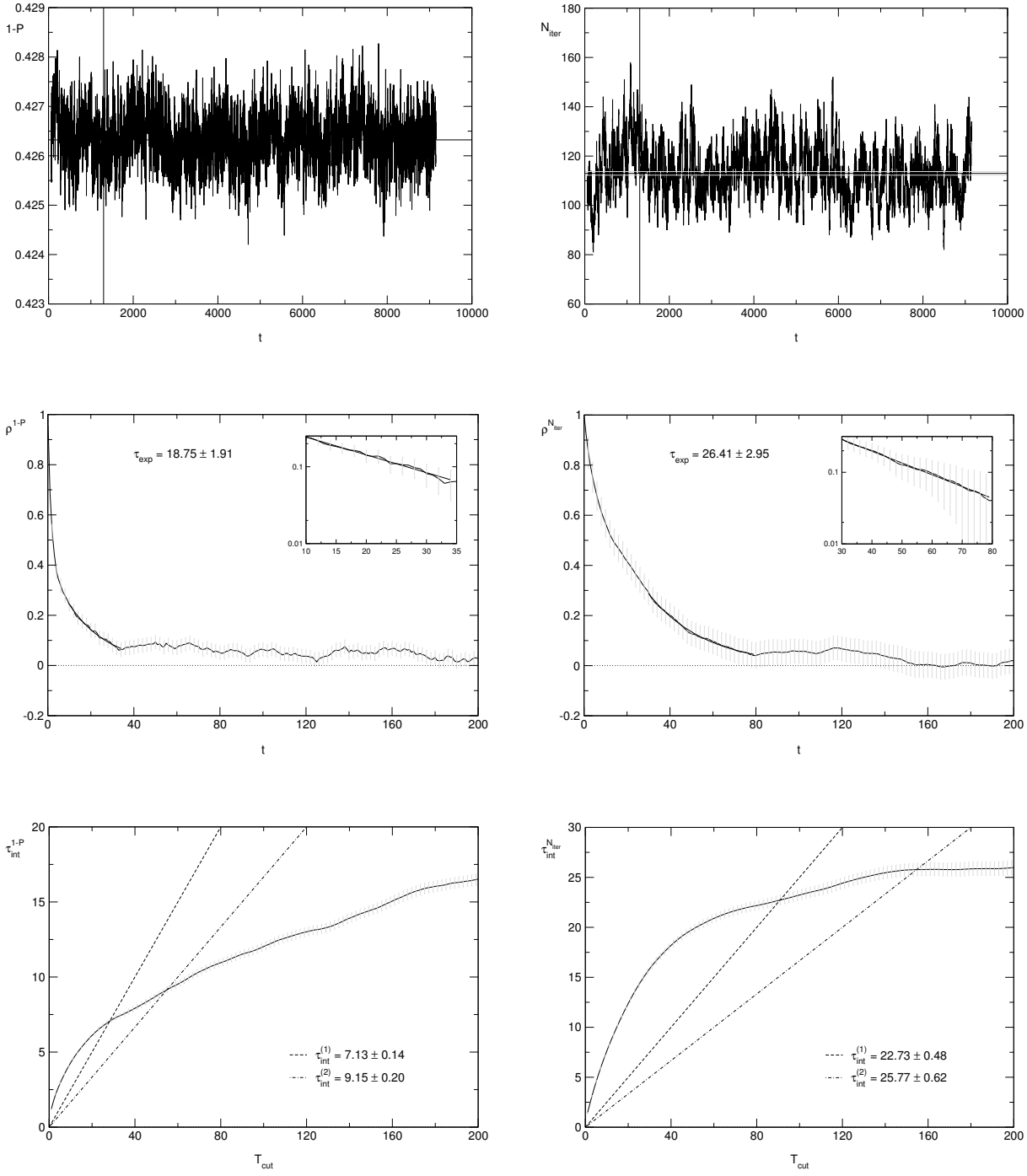

Figure B.5: $(\beta, \kappa, L) = (5.6, 0.158, 14)$.

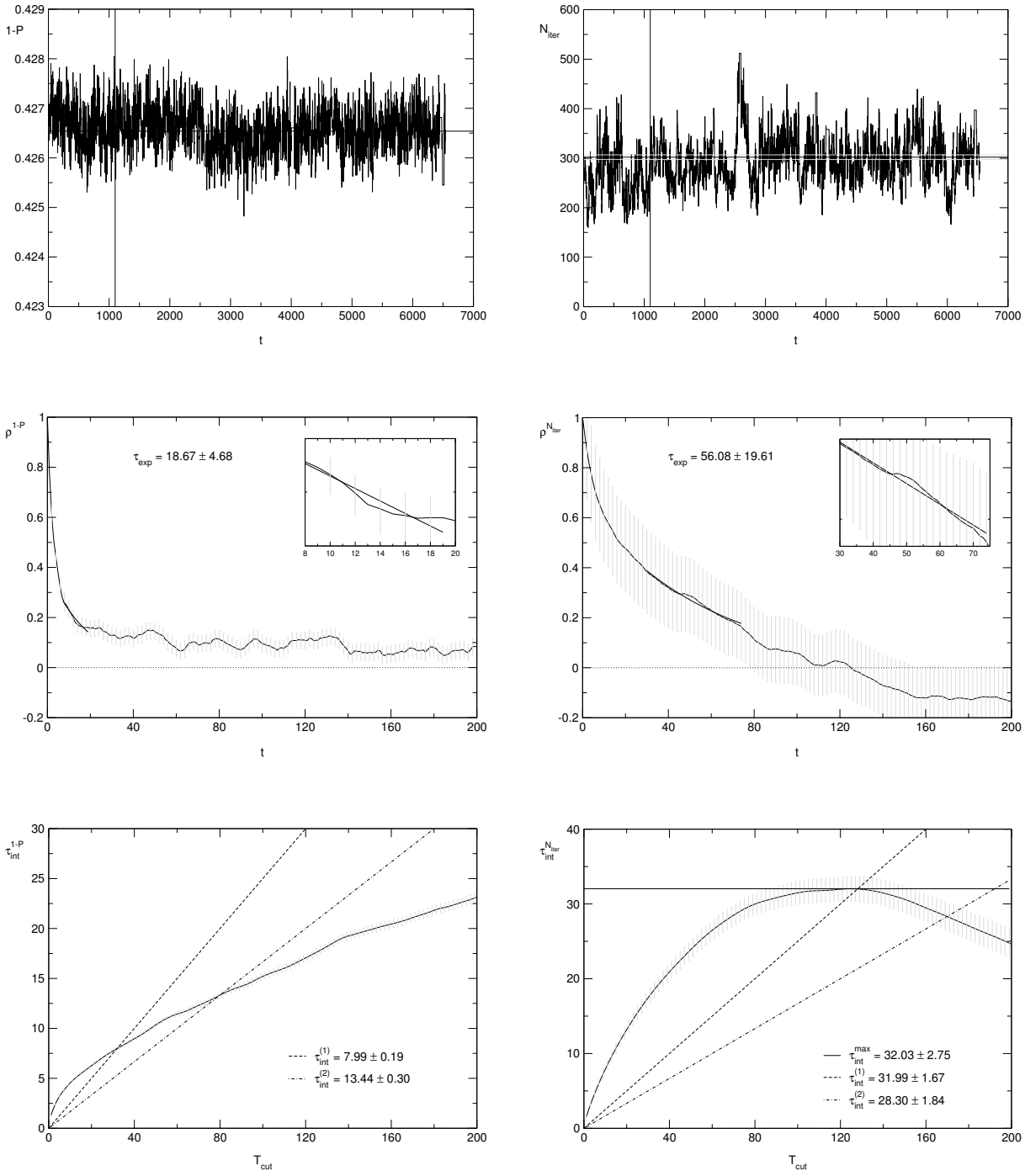

Figure B.6: $(\beta, \kappa, L) = (5.6, 0.158, 16)$.

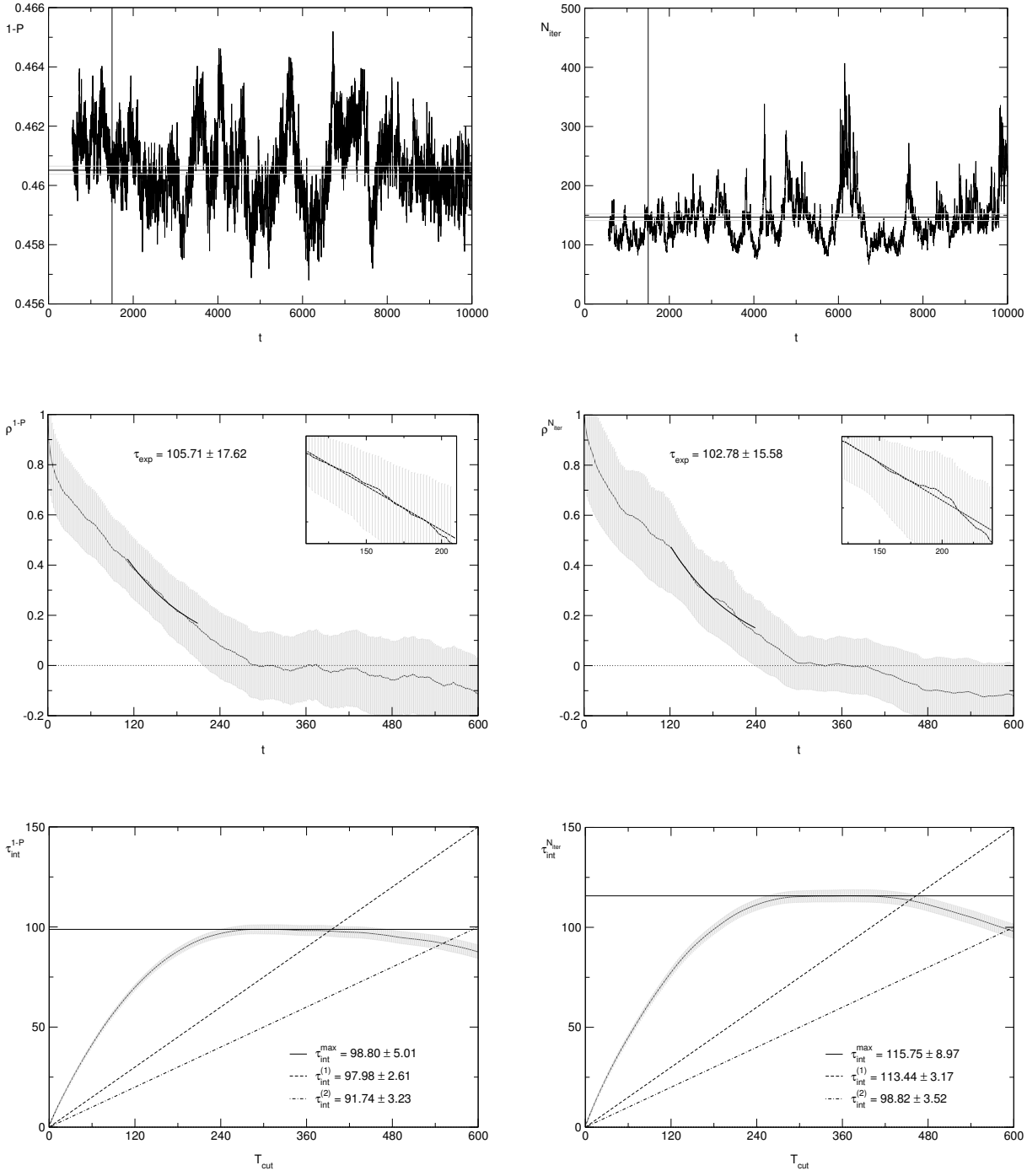

Figure B.7: $(\beta, \kappa, L) = (5.32144, 0.1665, 12)$.

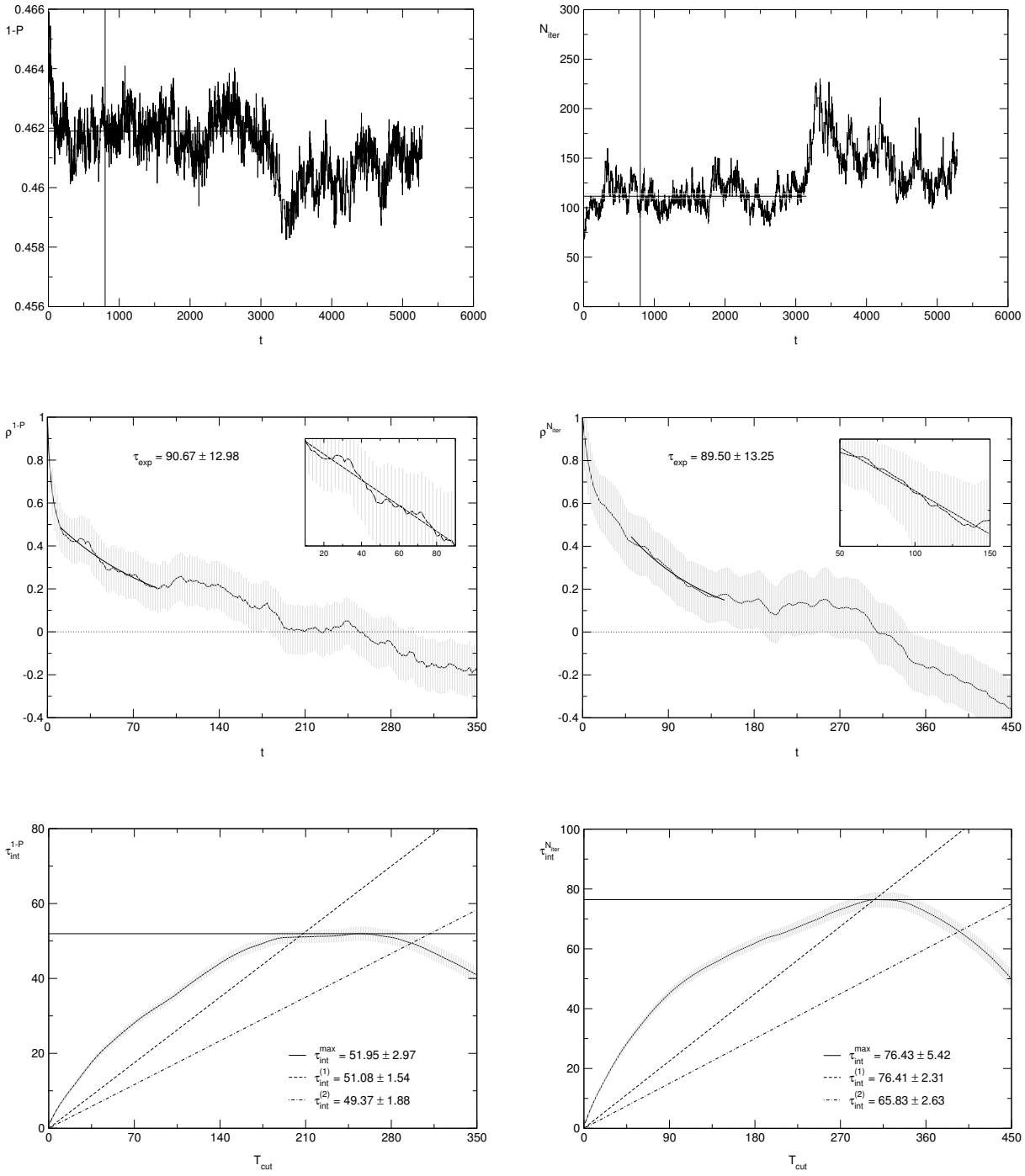

Figure B.8: $(\beta, \kappa, L) = (5.32144, 0.1665, 14)$.

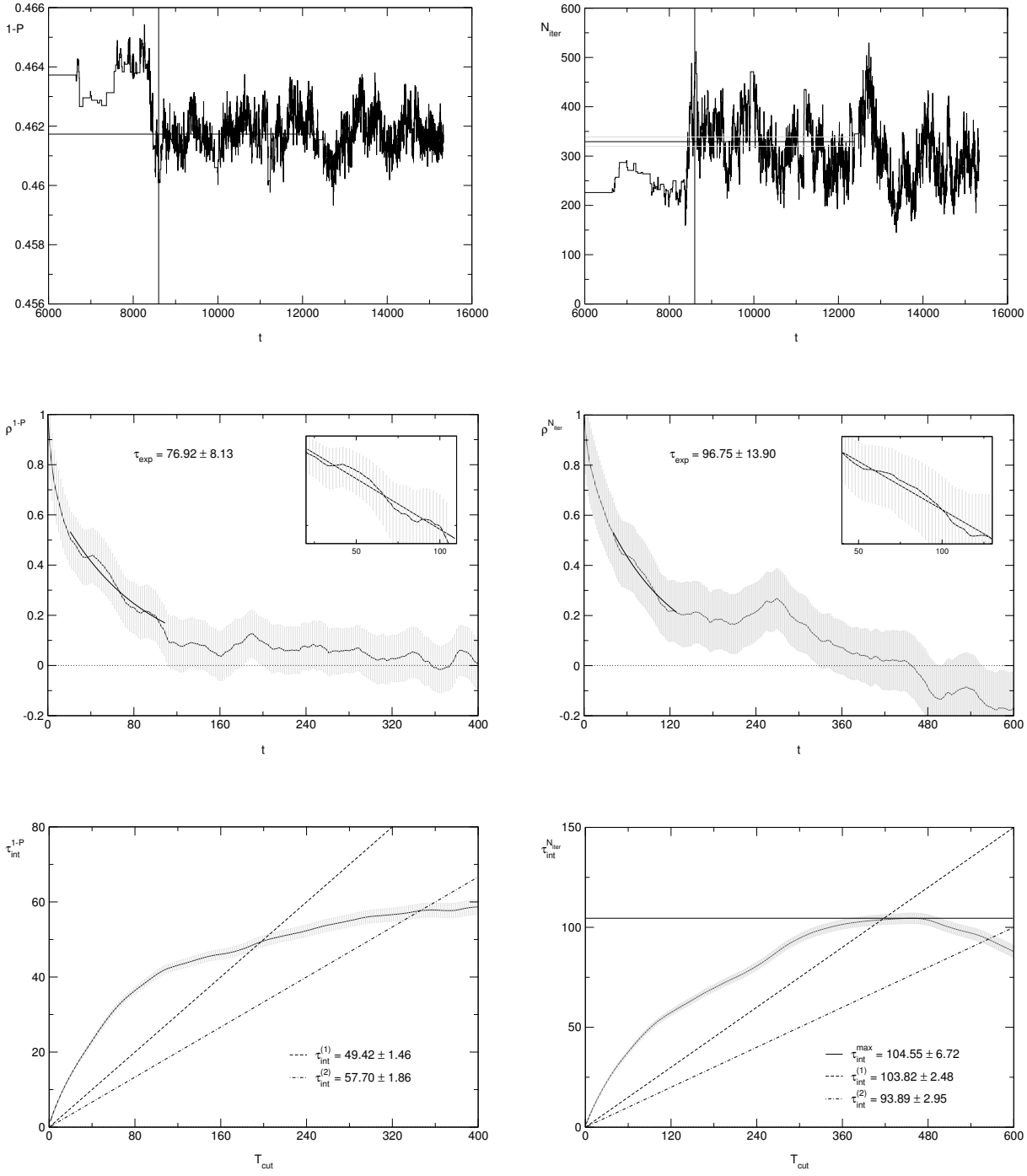

Figure B.9: $(\beta, \kappa, L) = (5.32144, 0.1665, 16)$ (larger integration step size).

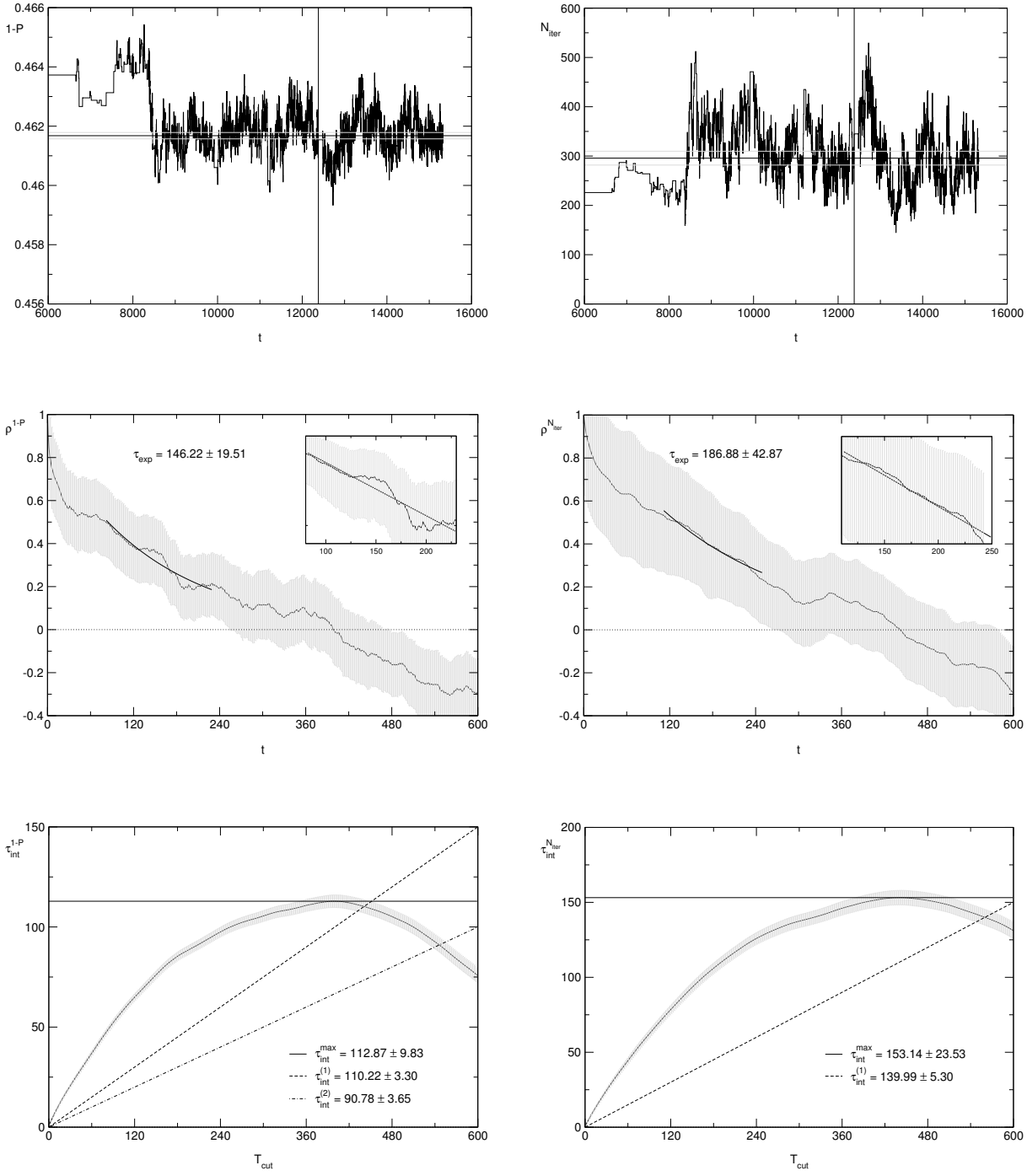

Figure B.10: $(\beta, \kappa, L) = (5.32144, 0.1665, 16)$ (smaller integration step size).

Appendix C

Parameters of the Correlator Fits

				$\left\langle P^\dagger(\tau)P(0)\right\rangle^{ls}$		$\left\langle V_k^\dagger(\tau)V_k(0)\right\rangle^{ls}$		$\left\langle N(\tau)\overline{N}(0)\right\rangle^{ls}$	
β	κ_{sea}	L^3T	b	$[\tau_{\min},\tau_{\max}]$	χ^2/df	$[\tau_{\min},\tau_{\max}]$	χ^2/df	$[\tau_{\min},\tau_{\max}]$	χ^2/df
5.32144	0.1665	$12^3 32$	7	5,14	0.48	5,14	2.25	5,12	0.82
		$14^3 32$	7	8,14	0.88	5,14	0.41	6,11	0.81
		$16^3 32$	7	5,15	1.12	6,15	1.74	5,14	0.75
5.5	0.1580	$16^3 32$	7	9,15	0.69	9,15	0.77	6,14	0.94
	0.1590	$16^3 32$	8	7,15	1.17	9,15	1.16	9,14	0.72
	0.1596	$16^3 32$	5	7,15	1.47	7,15	2.30	7,14	1.18
	0.1600	$16^3 32$	6	7,15	1.09	7,15	0.56	8,14	0.54
5.6	0.1560	$16^3 32$	5	7,15	2.33	11,15	0.90	7,14	1.31
	0.1565	$16^3 32$	7	10,15	1.58	8,15	1.66	9,14	0.81
	0.1570	$16^3 32$	7	10,15	0.34	8,15	1.51	8,14	2.49
	0.1575	$10^3 32$	9	7,15	1.24	10,15	0.95	7,14	0.82
		$12^3 32$	9	10,15	1.73	8,15	0.70	10,14	0.38
		$14^3 32$	6	7,15	0.42	10,15	0.32	7,14	0.45
		$16^3 32$	4	8,15	0.29	10,15	0.15	9,14	0.68
		$24^3 40$	7	10,19	1.50	10,19	1.72	10,18	0.76
	0.1580	$12^3 32$	3	6,15	1.17	9,15	2.18	9,14	0.69
		$14^3 32$	5	7,15	0.79	10,15	0.59	9,14	0.17
		$16^3 32$	8	7,15	0.54	11,15	1.66	7,14	0.74
		$24^3 40$	9	10,19	2.15	10,19	1.33	12,18	1.04

Table C.1: Fit parameters for the local-smeared pseudoscalar, vector and nucleon correlators. b denotes the blocksize for the jackknife, $[\tau_{\min}, \tau_{\max}]$ is the fitted interval and χ^2/df indicates the fit quality.

				$\langle A_4^\dagger(\tau)A_4(0)\rangle^{ss}$		$\langle A_4^\dagger(\tau)P(0)\rangle^{ss}$		$\langle P^\dagger(\tau)A_4(0)\rangle^{ss}$	
β	κ_{sea}	L^3T	b	$[\tau_{\min},\tau_{\max}]$	χ^2/df	$[\tau_{\min},\tau_{\max}]$	χ^2/df	$[\tau_{\min},\tau_{\max}]$	χ^2/df
5.32144	0.1665	$12^3 32$	7	4,14	0.65	6,14	0.44	5,12	0.88
		$14^3 32$	7	4,14	1.34	4,14	1.86	4,11	1.46
		$16^3 32$	7	7,15	1.42	7,15	0.81	5,14	1.00
5.5	0.1580	$16^3 32$	7	4,15	1.06	3,15	1.03	6,14	0.98
	0.1590	$16^3 32$	8	5,15	1.24	5,15	1.33	8,14	1.05
	0.1596	$16^3 32$	5	3,15	0.91	3,15	1.87	9,14	1.16
	0.1600	$16^3 32$	6	8,15	1.95	3,15	1.86	3,14	1.43
5.6	0.1560	$16^3 32$	5	4,15	0.67	3,15	0.70	3,14	0.58
	0.1565	$16^3 32$	7	3,15	0.69	3,15	0.83	3,14	1.02
	0.1570	$16^3 32$	7	3,15	0.59	3,15	0.41	8,14	0.11
	0.1575	$10^3 32$	9	4,15	1.52	3,15	0.79	5,14	1.36
		$12^3 32$	9	6,15	1.11	3,15	0.97	3,14	1.26
		$14^3 32$	6	5,15	0.45	6,15	0.86	5,14	1.41
		$16^3 32$	4	4,15	0.80	7,15	0.48	3,14	0.98
		$24^3 40$	7	7,19	1.31	7,19	1.16	4,18	0.98
	0.1580	$12^3 32$	3	5,15	1.04	3,15	0.92	4,14	1.27
		$14^3 32$	5	6,15	0.63	6,15	1.32	4,14	0.61
		$16^3 32$	8	4,15	0.84	4,15	1.21	6,14	1.03
		$24^3 40$	9	9,19	1.02	3,19	2.48	3,18	2.09

Table C.2: Fit parameters for the fully smeared pseudoscalar correlators involving A_4.

				$\left\langle A_4^\dagger(\tau)A_4(0)\right\rangle^{ls}$		$\left\langle A_4^\dagger(\tau)P(0)\right\rangle^{ls}$		$\left\langle P^\dagger(\tau)A_4(0)\right\rangle^{ls}$	
β	κ_{sea}	L^3T	b	$[\tau_{\min},\tau_{\max}]$	χ^2/df	$[\tau_{\min},\tau_{\max}]$	χ^2/df	$[\tau_{\min},\tau_{\max}]$	χ^2/df
5.32144	0.1665	$12^3 32$	7	5,14	1.81	6,14	1.53	6,12	0.39
		$14^3 32$	7	4,14	1.81	4,14	1.23	4,11	0.78
		$16^3 32$	7	7,15	1.12	8,15	0.95	8,14	1.09
5.5	0.1580	$16^3 32$	7	5,15	1.10	3,15	0.97	9,14	0.77
	0.1590	$16^3 32$	8	6,15	1.52	4,15	2.08	9,14	0.89
	0.1596	$16^3 32$	5	4,15	1.89	3,15	1.93	8,14	0.63
	0.1600	$16^3 32$	6	3,15	1.16	3,15	1.31	8,14	0.92
5.6	0.1560	$16^3 32$	5	6,15	1.62	3,15	1.60	8,14	1.74
	0.1565	$16^3 32$	7	3,15	1.19	3,15	1.04	6,14	0.45
	0.1570	$16^3 32$	7	3,15	1.17	8,15	0.58	9,14	0.05
	0.1575	$10^3 32$	9	5,15	1.42	3,15	1.21	5,14	1.09
		$12^3 32$	9	6,15	1.10	6,15	1.01	5,14	0.86
		$14^3 32$	6	6,15	0.74	6,15	0.91	10,14	1.20
		$16^3 32$	4	9,15	1.24	9,15	0.67	5,14	0.66
		$24^3 40$	7	8,19	1.13	7,19	1.25	7,18	0.93
	0.1580	$12^3 32$	3	5,15	1.66	3,15	1.03	5,14	1.25
		$14^3 32$	5	6,15	1.26	7,15	1.47	4,14	1.06
		$16^3 32$	8	3,15	0.94	4,15	1.26	5,14	1.25
		$24^3 40$	9	10,19	0.39	10,19	2.16	6,18	1.43

Table C.3: Fit parameters for the local-smeared pseudoscalar correlators involving A_4.

Appendix D

Fits of the Volume Dependence

The tables on the following pages show the parameters from fits of our data for the pseudoscalar meson (PS), the vector (V) meson and the nucleon masses to the power law (4.13) and the exponential (4.15) as discussed in Section 4.4.1.

D.1 Power Law

Fit type	H	$[L_1,L_2]$	m_H [GeV]	c_1 [GeV^{-2}]	χ^2/df	$\Delta(L_{\max})$	$\Delta(L=\infty)$
pow ($c_2=3$)	PS	10,14	0.455(19)	54.5(2.3)	1.09	-21.46%	-29.17%
pow ($c_2=3$)	PS	10,16	0.484(17)	51.7(2.6)	2.42	-17.38%	-24.70%
pow ($c_2=3$)	PS	10,24	0.570(35)	41.2(7.1)	31.65	-5.57%	-11.40%
pow ($c_2=3$)	PS	12,24	0.612(26)	21.8(8.3)	10.28	-1.70%	-4.78%
pow ($c_2=3$)	PS	14,24	0.625(23)	14.6(8.5)	6.94	-0.68%	-2.75%
pow ($c_2=3$)	V	10,14	0.8310(94)	42.9(1.5)	0.06	-5.14%	-9.39%
pow ($c_2=3$)	V	10,16	0.806(16)	46.2(3.1)	0.44	-7.54%	-12.12%
pow ($c_2=3$)	V	10,24	0.872(19)	35.1(5.3)	3.34	-1.38%	-4.87%
pow ($c_2=3$)	V	12,24	0.879(24)	32.1(7.4)	4.11	-0.99%	-4.18%
pow ($c_2=3$)	V	14,24	0.889(28)	26.3(10.8)	4.88	-0.49%	-3.10%
pow ($c_2=3$)	N	10,14	1.228(31)	94.5(3.8)	0.25	-4.56%	-10.80%
pow ($c_2=3$)	N	10,16	1.155(32)	102.1(5.3)	1.05	-9.38%	-16.12%
pow ($c_2=3$)	N	10,24	1.255(43)	88.5(9.3)	5.83	-2.99%	-8.84%
pow ($c_2=3$)	N	12,24	1.276(54)	79.2(16.0)	6.83	-2.06%	-7.29%
pow ($c_2=3$)	N	14,24	1.307(74)	62.0(29.2)	8.74	-0.95%	-5.04%

Table D.1: Parameters of L^{-3}-fits in various L-intervals at $(\beta,\kappa) = (5.6, 0.1575)$.

Fit type	H	$[L_1,L_2]$	m_H [GeV]	c_1 [GeV^{-2}]	χ^2/df	$\Delta(L_{\max})$	$\Delta(L=\infty)$
pow ($c_2=3$)	PS	12,16	0.294(26)	77.7(5.1)	0.63	-22.84%	-39.91%
pow ($c_2=3$)	PS	12,24	0.417(33)	55.3(9.2)	8.55	-2.67%	-14.81%
pow ($c_2=3$)	PS	14,24	0.430(41)	49.0(13.2)	10.75	-1.43%	-12.19%
pow ($c_2=3$)	V	12,16	0.67(16)	81.3(28.5)	6.55	-12.85%	-22.95%
pow ($c_2=3$)	V	12,24	0.780(59)	62.5(13.1)	5.22	-2.10%	-9.86%
pow ($c_2=3$)	V	14,24	0.779(93)	62.7(24.8)	10.44	-2.13%	-9.93%
pow ($c_2=3$)	N	12,16	1.0655(38)	128.28(75)	<0.01	-2.02%	-13.25%
pow ($c_2=3$)	N	12,24	1.0894(92)	124.0(2.3)	0.07	-0.44%	-11.30%
pow ($c_2=3$)	N	14,24	1.095(11)	121.6(3.3)	0.07	-0.19%	-10.84%

Table D.2: Parameters of L^{-3}-fits in various L-intervals at $(\beta,\kappa) = (5.6, 0.158)$.

Fit type	H	$[L_1,L_2]$	m_H [GeV]	c_1 [GeV^{-2}]	χ^2/df	$\Delta(L_{\max})$	$\Delta(L=\infty)$
pow ($c_2=3$)	PS	12,16	0.428(22)	-15.0(16.3)	2.09	-0.83%	2.23%
pow ($c_2=3$)	V	12,16	0.743(32)	23.3(29.0)	0.77	0.54%	-2.08%
pow ($c_2=3$)	N	12,16	1.037(63)	90.9(52.8)	1.87	0.98%	-6.05%

Table D.3: Parameters of L^{-3}-fits in various L-intervals at $(\beta,\kappa) = (5.32144, 0.1665)$.

Fit type	H	$[L_1,L_2]$	m_H [GeV]	c_1 [GeV^{-d}]	c_2	χ^2/df	$\Delta(L_{\max})$	$\Delta(L=\infty)$
pow	PS	10,24	0.635(11)	2954(3063)	5.94(72)	2.31	-0.77%	-1.21%
pow	V	10,24	0.901(20)	248(335)	4.27(88)	2.24	-0.48%	-1.74%
pow	N	10,24	1.331(51)	408(444)	4.05(75)	3.82	-0.95%	-3.29%

Table D.4: Parameters of general power-law fits at $(\beta,\kappa) = (5.6, 0.1575)$ (full L-range). $d = c_2 - 1$.

Fit type	H	$[L_1,L_2]$	m_H [GeV]	c_1 [GeV^{-d}]	c_2	χ^2/df	$\Delta(L_{\max})$	$\Delta(L=\infty)$
pow	PS	12,24	0.471(28)	1241(2338)	4.9(1.2)	4.18	-0.55%	-3.86%
pow	V	12,24	0.82(12)	270(1222)	3.9(2.9)	9.23	-1.10%	-5.06%
pow	N	12,24	1.114(10)	173(23)	3.218(85)	0.02	-0.04%	-9.28%

Table D.5: Parameters of general power-law fits at $(\beta,\kappa) = (5.6, 0.158)$ (full L-range). $d = c_2 - 1$.

Fit type	H	$[L_1,L_2]$	m_H [GeV]	c_1 [GeV^{-d}]	c_2	χ^2/df	$\Delta(L_{\max})$	$\Delta(L=\infty)$
pow	PS	12,16	0.410	100.1	27.4		-2.22%	-2.22%
pow	V	12,16	-26.3	27.3	0.004		0.36%	-3564.89%
pow	N	12,16	-84.4	86.4	0.004		0.59%	-7746.92%

Table D.6: Parameters of general power-law fits at $(\beta,\kappa) = (5.32144, 0.1665)$ (full L-range). $d = c_2 - 1$.

D.2 Exponential

Fit type	H	$[L_1,L_2]$	$m_H\,[\mathrm{GeV}]$	$c_1\,[\mathrm{GeV}^{-1/2}]$	c_2	χ^2/df	$\Delta(L_{\max})$	$\Delta(L=\infty)$
exp	PS	10,24	0.6385(73)	210.7(94.5)	0.89(10)	1.30	-0.60%	-0.70%
exp	V	10,24	0.909(14)	50.5(34.4)	0.58(14)	1.68	-0.40%	-0.84%
exp	N	10,24	1.355(36)	96.5(51.5)	0.53(12)	2.78	-0.74%	-1.59%

Table D.7: Parameters of general exponential fits at $(\beta,\kappa) = (5.6, 0.1575)$ (full L-range).

Fit type	H	$[L_1,L_2]$	$m_H\,[\mathrm{GeV}]$	$c_1\,[\mathrm{GeV}^{-1/2}]$	c_2	χ^2/df	$\Delta(L_{\max})$	$\Delta(L=\infty)$
exp	PS	12,24	0.481(20)	133.6(121.6)	0.66(18)	3.17	-0.46%	-1.83%
exp	V	12,24	0.841(90)	64.1(154.8)	0.50(49)	8.56	-1.01%	-2.78%
exp	N	12,24	1.1655(16)	61.22(90)	0.3553(30)	< 0.01	-0.01%	-5.10%

Table D.8: Parameters of general exponential fits at $(\beta,\kappa) = (5.6, 0.158)$ (full L-range).

Fit type	H	$[L_1,L_2]$	$m_H\,[\mathrm{GeV}]$	$c_1\,[\mathrm{GeV}^{-1/2}]$	c_2	χ^2/df	$\Delta(L_{\max})$	$\Delta(L=\infty)$
exp	PS	12,16	0.410	111.99	6.695		-2.22%	-2.22%
exp	V	12,16	0.694	1.69	-0.03		0.45%	-8.48%
exp	N	12,16	0.857	6.39	-0.03		0.77%	-22.40%

Table D.9: Parameters of general exponential fits at $(\beta,\kappa) = (5.32144, 0.1665)$ (full L-range).

Fit type	H	$[L_1,L_2]$	$m_H\,[\mathrm{GeV}]$	$c_1\,[\mathrm{GeV}^{-1/2}]$	χ^2/df	$\Delta(L_{\max})$	$\Delta(L=\infty)$
exp $(c_2=m_{\mathrm{PS}})$	PS	10,24	0.624(13)	65.9(4.2)	5.59	-2.41%	-2.91%
exp $(c_2=m_{\mathrm{PS}})$	V	10,24	0.9125(92)	63.5(5.6)	1.19	-0.17%	-0.51%
exp $(c_2=m_{\mathrm{PS}})$	N	10,24	1.372(22)	142.7(9.5)	2.37	0.18%	-0.32%
exp $(c_2=m_{\mathrm{PS}})$	PS	12,24	0.632(12)	52.7(9.4)	3.70	-1.28%	-1.64%
exp $(c_2=m_{\mathrm{PS}})$	V	12,24	0.9092(98)	72.6(8.7)	1.18	-0.52%	-0.87%
exp $(c_2=m_{\mathrm{PS}})$	N	12,24	1.361(22)	167.9(17.8)	1.99	-0.59%	-1.13%
exp $(c_2=m_{\mathrm{PS}})$	PS	14,24	0.637(13)	42.3(14.9)	3.78	-0.66%	-0.94%
exp $(c_2=m_{\mathrm{PS}})$	V	14,24	0.910(15)	73.1(19.8)	2.32	-0.46%	-0.80%
exp $(c_2=m_{\mathrm{PS}})$	N	14,24	1.357(35)	184.9(53.3)	3.69	-0.88%	-1.44%
exp $(c_2=m_{\mathrm{PS}})$	PS	16,24	0.642	15.1			-0.09%
exp $(c_2=m_{\mathrm{PS}})$	V	16,24	0.916	34.1			-0.15%
exp $(c_2=m_{\mathrm{PS}})$	N	16,24	1.372	123.8			-0.36%

Table D.10: Parameters of $\exp(-m_{\mathrm{PS}}L)/L^{3/2}$-fits in various L-intervals at $(\beta,\kappa)=(5.6,0.1575)$.

Fit type	H	$[L_1,L_2]$	$m_H\,[\mathrm{GeV}]$	$c_1\,[\mathrm{GeV}^{-1/2}]$	χ^2/df	$\Delta(L_{\max})$	$\Delta(L=\infty)$
exp $(c_2=m_{\mathrm{PS}})$	PS	12,24	0.466(20)	47.9(4.2)	3.86	-1.50%	-4.91%
exp $(c_2=m_{\mathrm{PS}})$	V	12,24	0.836(45)	53.1(10.0)	4.31	-1.27%	-3.41%
exp $(c_2=m_{\mathrm{PS}})$	N	12,24	1.208(20)	104.1(5.1)	0.50	1.30%	-1.65%
exp $(c_2=m_{\mathrm{PS}})$	PS	14,24	0.469(27)	46.1(6.6)	6.29	-1.05%	-4.22%
exp $(c_2=m_{\mathrm{PS}})$	V	14,24	0.827(66)	58.6(19.6)	7.75	-2.12%	-4.40%
exp $(c_2=m_{\mathrm{PS}})$	N	14,24	1.195(15)	114.1(5.4)	0.21	0.39%	-2.74%
exp $(c_2=m_{\mathrm{PS}})$	PS	16,24	0.479	34.8			-2.17%
exp $(c_2=m_{\mathrm{PS}})$	V	16,24	0.859	19.7			-0.70%
exp $(c_2=m_{\mathrm{PS}})$	N	16,24	1.189	127.9			-3.18%

Table D.11: Parameters of $\exp(-m_{\mathrm{PS}}L)/L^{3/2}$-fits in various L-intervals at $(\beta,\kappa)=(5.6,0.158)$.

Fit type	H	$[L_1,L_2]$	$m_H\,[\mathrm{GeV}]$	$c_1\,[\mathrm{GeV}^{-1/2}]$	χ^2/df	$\Delta(L_{\max})$	$\Delta(L=\infty)$
exp $(c_1=C, c_2=m_{\mathrm{PS}})$	PS	12,16	0.4093(79)		1.99	-2.29%	-2.29%
exp $(c_2=m_{\mathrm{PS}})$	V	12,16	0.756(20)	18.4(26.8)	0.86	0.64%	-0.31%
exp $(c_2=m_{\mathrm{PS}})$	N	12,16	1.088(42)	75.0(50.6)	2.32	1.19%	-1.46%
exp $(c_1=C, c_2=m_{\mathrm{PS}})$	PS	14,16	0.412(12)		3.22	-1.58%	-1.58%
exp $(c_2=m_{\mathrm{PS}})$	V	14,16	0.733395	66.446			-3.31%
exp $(c_2=m_{\mathrm{PS}})$	N	14,16	1.03317	186.934			-6.41%

Table D.12: Parameters of $\exp(-m_{\mathrm{PS}}L)/L^{3/2}$-fits in var. L-intervals at $(\beta,\kappa)=(5.32144,0.1665)$.

Fit type	H	$[L_1,L_2]$	$m_H\,[\mathrm{GeV}]$	$c_1\,[\mathrm{GeV}^{-1/2}]$	χ^2/df	$\Delta(L_{\max})$	$\Delta(L=\infty)$
exp $(c_2=m_{\mathrm{PS}})$	PS	10,16	0.5912(48)	62.35(85)	0.22	-7.39%	-8.04%
exp $(c_2=m_{\mathrm{PS}})$	V	10,16	0.902(20)	56.7(7.1)	1.52	-1.19%	-1.61%
exp $(c_2=m_{\mathrm{PS}})$	N	10,16	1.363(40)	124.3(11.1)	3.09	-0.38%	-0.99%
exp $(c_2=m_{\mathrm{PS}})$	PS	12,16	0.59829(24)	59.909(72)	<0.01	-6.36%	-6.95%
exp $(c_2=m_{\mathrm{PS}})$	V	12,16	0.883(22)	71.2(10.7)	1.00	-3.25%	-3.74%
exp $(c_2=m_{\mathrm{PS}})$	N	12,16	1.331(53)	151.2(25.6)	3.12	-2.62%	-3.31%

Table D.13: Parameters of infinite-volume extrapolation at $(\beta,\kappa)=(5.6,0.1575)$.

Fit type	H	$[L_1,L_2]$	$m_H\,[\mathrm{GeV}]$	$c_1\,[\mathrm{GeV}^{-1/2}]$	χ^2/df	$\Delta(L_{\max})$	$\Delta(L=\infty)$
exp $(c_2=m_{\mathrm{PS}})$	PS	12,16	0.343(50)	35.8(5.3)	0.54	-21.46%	-29.84%
exp $(c_2=m_{\mathrm{PS}})$	V	12,16	0.72(14)	37.2(12.8)	6.31	-11.75%	-16.68%
exp $(c_2=m_{\mathrm{PS}})$	N	12,16	1.15393(39)	58.440(40)	<0.01	-0.59%	-6.05%

Table D.14: Parameters of infinite-volume extrapolation at $(\beta,\kappa)=(5.6,0.158)$.

List of Tables

List of Figures

Bibliography

[1] K. Hagiwara *et al.* [Particle Data Group Collaboration], "Review Of Particle Physics," Phys. Rev. D **66** (2002) 010001.

[2] D. J. Gross and F. Wilczek, Phys. Rev. Lett. **30** (1973) 1343; S. Weinberg, Phys. Rev. Lett. **31** (1973) 494; H. Fritzsch, M. Gell-Mann and H. Leutwyler, Phys. Lett. B **47** (1973) 365.

[3] S. L. Glashow, Nucl. Phys. **22** (1961) 579; S. Weinberg, Phys. Rev. Lett. **19** (1967) 1264; A. Salam and J. C. Ward, Phys. Lett. **13** (1964) 168; A. Salam in *Elementary particle physics (Nobel Symp. No. 8)* (ed. N. Svartholm) Almqvist and Wilsell, Stockholm (1968).

[4] D. J. Griffiths, "Introduction To Elementary Particles," John Wiley, Singapore (1987).

[5] M. E. Peskin and D. V. Schroeder, "An Introduction To Quantum Field Theory," Addison-Wesley, Reading, Mass. (1995).

[6] C. N. Yang and R. L. Mills, Phys. Rev. **96** (1954) 191.

[7] G. 't Hooft, Nucl. Phys. B **33** (1971) 173, Nucl. Phys. B **35** (1971) 167.

[8] H. D. Politzer, Phys. Rev. Lett. **30** (1973) 1346, Phys. Rept. **14** (1974) 129; D. J. Gross and F. Wilczek, Phys. Rev. Lett. **30** (1973) 1343, Phys. Rev. D **8** (1973) 3633.

[9] S. Mandelstam, Phys. Rept. **23** (1976) 245.

[10] M. Creutz, "Quarks, Gluons And Lattices," Cambridge University Press, Cambridge (1983).

[11] R. Gupta, "Introduction to lattice QCD," arXiv:hep-lat/9807028.

[12] I. Montvay and G. Munster, "Quantum Fields On A Lattice," Cambridge University Press, Cambridge (1994).

[13] K. G. Wilson, Phys. Rev. D **10** (1974) 2445.

[14] R. P. Feynman, Rev. Mod. Phys. **20** (1948) 367.

[15] S. Aoki, S. Hashimoto, N. Ishizuka, K. Kanaya and Y. Kuramashi (eds.), "Lattice Field Theory. Proceedings, 21st International Symposium, Lattice 2003, Tsukuba, Japan, July 15-19, 2003," Nucl. Phys. B, Proc. Suppl. 129/130 (2004).

[16] K. Symanzik, Nucl. Phys. B **226** (1983) 187, 205.

[17] C. R. Allton *et al.* [UKQCD Collaboration], arXiv:hep-lat/0403007.

[18] F. Farchioni, I. Montvay and E. Scholz [qq+q Collaboration], arXiv:hep-lat/0403014.

[19] Y. Namekawa *et al.* [CP-PACS Collaboration], arXiv:hep-lat/0404014.

[20] S. Duane, A. D. Kennedy, B. J. Pendleton and D. Roweth, Phys. Lett. B **195** (1987) 216.

[21] T. Lippert [SESAM/TXL Collaboration], Nucl. Phys. Proc. Suppl. **106** (2002) 193 [arXiv:hep-lat/0203009].

[22] A. Ukawa [CP-PACS and JLQCD Collaborations], Nucl. Phys. Proc. Suppl. **106** (2002) 195.

[23] H. Wittig [UKQCD, QCDSF and ALPHA Collaborations], Nucl. Phys. Proc. Suppl. **106** (2002) 197 [arXiv:hep-lat/0203021].

[24] S. Aoki *et al.* [CP-PACS Collaboration], Phys. Rev. Lett. **84** (2000) 238 [arXiv:hep-lat/9904012], Phys. Rev. D **67** (2003) 034503 [arXiv:hep-lat/0206009].

[25] K. G. Wilson, CLNS-321 *New Phenomena In Subnuclear Physics. Part A. Proceedings of the First Half of the 1975 International School of Subnuclear Physics, Erice, Sicily, July 11 - August 1, 1975, ed. A. Zichichi, Plenum Press, New York, 1977, p. 69, CLNS-321*

[26] J. B. Kogut and L. Susskind, Phys. Rev. D **11** (1975) 395.

[27] C. T. H. Davies *et al.* [HPQCD-MILC-UKQCD Collaboration], Phys. Rev. Lett. **92** (2004) 022001 [arXiv:hep-lat/0304004].

[28] C. Aubin *et al.* [HPQCD-MILC-UKQCD Collaboration], arXiv:hep-lat/0405022.

[29] D. B. Kaplan, Phys. Lett. B **288** (1992) 342 [arXiv:hep-lat/9206013].

[30] R. Narayanan and H. Neuberger, Phys. Rev. Lett. **71** (1993) 3251 [arXiv:hep-lat/9308011], Nucl. Phys. B **443** (1995) 305 [arXiv:hep-th/9411108]; H. Neuberger, Phys. Lett. B **417** (1998) 141 [arXiv:hep-lat/9707022].

[31] J. van den Eshof, A. Frommer, T. Lippert, K. Schilling and H. A. van der Vorst, Comput. Phys. Commun. **146**, 203 (2002) [arXiv:hep-lat/0202025]; G. Arnold, N. Cundy, J. van den Eshof, A. Frommer, S. Krieg, T. Lippert and K. Schafer, arXiv:hep-lat/0311025; N. Cundy, J. van der Eshof, A. Frommer, S. Krieg, T. Lippert and K. Schafer, arXiv:hep-lat/0405003.

[32] Z. Fodor, S. D. Katz and K. K. Szabo, arXiv:hep-lat/0311010.

[33] C. W. Bernard *et al.*, Phys. Rev. D **64** (2001) 054506 [arXiv:hep-lat/0104002].

[34] T. Kaneko *et al.* [CP-PACS Collaboration], Nucl. Phys. Proc. Suppl. **129** (2004) 188 [arXiv:hep-lat/0309137].

[35] N. Eicker *et al.* [SESAM Collaboration], Phys. Rev. D **59** (1999) 014509 [arXiv:hep-lat/9806027].

[36] T. Lippert *et al.* [SESAM/TχL Collaboration], Nucl. Phys. Proc. Suppl. **60A** (1998) 311 [arXiv:hep-lat/9707004].

[37] N. Eicker, T. Lippert, B. Orth and K. Schilling [SESAM/TχL Collaboration], Nucl. Phys. Proc. Suppl. **106** (2002) 209 [arXiv:hep-lat/0110134].

[38] C. R. Allton *et al.* [UKQCD Collaboration], Phys. Rev. D **65** (2002) 054502 [arXiv:hep-lat/0107021]; Phys. Rev. D **60** (1999) 034507 [arXiv:hep-lat/9808016].

[39] A. Ali Khan *et al.* [CP-PACS Collaboration], Phys. Rev. D **65** (2002) 054505 [Erratum-ibid. D **67** (2003) 059901] [arXiv:hep-lat/0105015], Phys. Rev. Lett. **85** (2000) 4674 [Erratum-ibid. **90** (2003) 029902] [arXiv:hep-lat/0004010].

[40] S. Aoki *et al.* [JLQCD Collaboration], Phys. Rev. D **68** (2003) 054502 [arXiv:hep-lat/0212039].

[41] H. Stuben [QCDSF-UKQCD Collaboration], Nucl. Phys. Proc. Suppl. **94** (2001) 273 [arXiv:hep-lat/0011045].

[42] S. Weinberg, PhysicaA **96** (1979) 327.

[43] J. Gasser and H. Leutwyler, Annals Phys. **158** (1984) 142.

[44] C. W. Bernard and M. F. L. Golterman, Phys. Rev. D **49** (1994) 486 [arXiv:hep-lat/9306005].

[45] S. R. Sharpe, Phys. Rev. D **56** (1997) 7052 [Erratum-ibid. D **62** (2000) 099901] [arXiv:hep-lat/9707018].

[46] M. F. L. Golterman and K. C. L. Leung, Phys. Rev. D **57** (1998) 5703 [arXiv:hep-lat/9711033].

[47] S. R. Sharpe and R. J. Singleton, Phys. Rev. D **58** (1998) 074501 [arXiv:hep-lat/9804028].

[48] G. Rupak and N. Shoresh, Phys. Rev. D **66** (2002) 054503 [arXiv:hep-lat/0201019].

[49] O. Bär, G. Rupak and N. Shoresh, arXiv:hep-lat/0306021.

[50] S. Aoki, Phys. Rev. D **68** (2003) 054508 [arXiv:hep-lat/0306027].

[51] B. Orth, N. Eicker, T. Lippert, K. Schilling, W. Schroers and Z. Sroczynski, Nucl. Phys. Proc. Suppl. **106** (2002) 269 [arXiv:hep-lat/0110158].

[52] B. Orth, T. Lippert and K. Schilling, Nucl. Phys. Proc. Suppl. **129** (2004) 173 [arXiv:hep-lat/0309085].

[53] M. Lüscher, Commun. Math. Phys. **104** (1986) 177;

[54] M. Lüscher, "On A Relation Between Finite Size Effects And Elastic Scattering Processes," DESY 83/116, *Lecture given at Cargese Summer Inst., Cargese, France, Sep 1-15, 1983.*

[55] B. Sheikholeslami-Sabzevari, Phys. Lett. B **227** (1989) 439.

[56] M. Fukugita, H. Mino, M. Okawa and A. Ukawa, Phys. Rev. Lett. **68** (1992) 761.

[57] M. Fukugita, H. Mino, M. Okawa, G. Parisi and A. Ukawa, Phys. Lett. B **294** (1992) 380, Nucl. Phys. Proc. Suppl. **30** (1993) 365.

[58] M. Fukugita, N. Ishizuka, H. Mino, M. Okawa and A. Ukawa, Phys. Rev. D **47** (1993) 4739.

[59] S. Aoki, T. Umemura, M. Fukugita, N. Ishizuka, H. Mino, M. Okawa and A. Ukawa, Nucl. Phys. Proc. Suppl. **34** (1994) 363 [arXiv:hep-lat/9311049].

[60] S. Aoki, T. Umemura, M. Fukugita, N. Ishizuka, H. Mino, M. Okawa and A. Ukawa, Phys. Rev. D **50** (1994) 486.

[61] C. W. Bernard, T. A. DeGrand, C. DeTar, S. Gottlieb, A. Krasnitz, R. L. Sugar and D. Toussaint [MILC Collaboration], Nucl. Phys. Proc. Suppl. **30** (1993) 369 [arXiv:hep-lat/9211007].

[62] C. W. Bernard *et al.*, Phys. Rev. D **48** (1993) 4419 [arXiv:hep-lat/9305023].

[63] S. Gottlieb, Nucl. Phys. Proc. Suppl. **53** (1997) 155 [arXiv:hep-lat/9608107].

[64] D. Becirevic and G. Villadoro, Phys. Rev. D **69** (2004) 054010 [arXiv:hep-lat/0311028].

[65] G. Colangelo and S. Dürr, Eur. Phys. J. C **33** (2004) 543 [arXiv:hep-lat/0311023]; G. Colangelo, S. Dürr and R. Sommer, Nucl. Phys. Proc. Suppl. **119** (2003) 254 [arXiv:hep-lat/0209110].

[66] A. A. Khan *et al.* [QCDSF-UKQCD Collaboration], arXiv:hep-lat/0312030.

[67] M. Guagnelli, K. Jansen, F. Palombi, R. Petronzio, A. Shindler and I. Wetzorke [Zeuthen-Rome (ZeRo) Collaboration], arXiv:hep-lat/0403009.

[68] D. Arndt and C. J. D. Lin, arXiv:hep-lat/0403012.

[69] S. R. Beane, arXiv:hep-lat/0403015.

[70] G. Colangelo and C. Haefeli, arXiv:hep-lat/0403025.

[71] J. Gasser and H. Leutwyler, Phys. Lett. B **184** (1987) 83, Phys. Lett. B **188** (1987) 477, Nucl. Phys. B **307** (1988) 763.

[72] H. Leutwyler, Phys. Lett. B **189** (1987) 197.

[73] P. Hasenfratz and H. Leutwyler, Nucl. Phys. B **343** (1990) 241.

[74] R. Sommer, Nucl. Phys. B **411** (1994) 839 [arXiv:hep-lat/9310022].

[75] A. Frommer, V. Hannemann, B. Nockel, T. Lippert and K. Schilling, Int. J. Mod. Phys. C **5** (1994) 1073 [arXiv:hep-lat/9404013];

[76] S. Fischer, A. Frommer, U. Glässner, T. Lippert, G. Ritzenhöfer and K. Schilling, Comput. Phys. Commun. **98** (1996) 20 [arXiv:hep-lat/9602019].

[77] I. Montvay, Nucl. Phys. B **466** (1996) 259 [arXiv:hep-lat/9510042].

[78] F. Farchioni, C. Gebert, I. Montvay and L. Scorzato, Eur. Phys. J. C **26** (2002) 237 [arXiv:hep-lat/0206008].

[79] A. C. Irving [UKQCD Collaboration], arXiv:hep-lat/0208065.

[80] Y. Namekawa *et al.* [CP-PACS Collaboration], arXiv:hep-lat/0209073.

[81] C. Battista *et al.*, Int. J. of High Speed Comp. **5** (1993) 637; R. Tripiccione, Int. J. Mod. Phys. C **4** (1993) 425.

[82] F. Aglietti *et al.*, Nucl. Instrum. Meth. A **389** (1997) 56.

[83] N. Eicker, C. Best, T. Lippert and K. Schilling, Nucl. Phys. Proc. Suppl. **83** (2000) 798 [arXiv:hep-lat/9909146].

[84] N. Attig, S. Güsken, P. Lacock, T. Lippert, K. Schilling, P. Überholz and J. Viehoff, Lect. Notes Comput. Sci. **1401** (1998) 183.

[85] P. W. Higgs, Phys. Lett. **12** (1964) 132, Phys. Rev. Lett. **13** (1964) 508, Phys. Rev. **145** (1966) 1156.

[86] K. Osterwalder and R. Schrader, Commun. Math. Phys. **31** (1973) 83, Commun. Math. Phys. **42** (1975) 281.

[87] H. B. Nielsen and M. Ninomiya, Phys. Lett. B **105** (1981) 219.

[88] R. Frezzotti and G. C. Rossi, arXiv:hep-lat/0306014.

[89] B. Sheikholeslami and R. Wohlert, Nucl. Phys. B **259** (1985) 572.

[90] G. P. Lepage and P. B. Mackenzie, Phys. Rev. D **48** (1993) 2250 [arXiv:hep-lat/9209022].

[91] M. Lüscher, R. Narayanan, P. Weisz and U. Wolff, Nucl. Phys. B **384** (1992) 168 [arXiv:hep-lat/9207009].

[92] K. Jansen and R. Sommer [ALPHA Collaboration], Nucl. Phys. B **530** (1998) 185 [Erratum-ibid. B **643** (2002) 517] [arXiv:hep-lat/9803017].

[93] K. G. Wilson, Phys. Rev. **179** (1969) 1499.

[94] Y. Iwasaki, Nucl. Phys. B **258** (1985) 141.

[95] For a review, see *e.g.*: P. Hasenfratz, arXiv:hep-lat/9803027.

[96] K. Orginos, D. Toussaint and R. L. Sugar [MILC Collaboration], Phys. Rev. D **60** (1999) 054503 [arXiv:hep-lat/9903032].

[97] A. Hasenfratz and F. Knechtli, Phys. Rev. D **64** (2001) 034504 [arXiv:hep-lat/0103029].

[98] R. Sommer *et al.* [ALPHA Collaboration], arXiv:hep-lat/0309171.

[99] P. H. Ginsparg and K. G. Wilson, Phys. Rev. D **25** (1982) 2649.

[100] S. Elitzur, Phys. Rev. D **12** (1975) 3978.

[101] K. Splittorff, Phys. Rev. D **68** (2003) 054504 [arXiv:hep-lat/0305013].

[102] R. Frezzotti, P. A. Grassi, S. Sint and P. Weisz, Nucl. Phys. Proc. Suppl. **83** (2000) 941 [arXiv:hep-lat/9909003], JHEP **0108** (2001) 058 [arXiv:hep-lat/0101001].

[103] For a recent review, see: R. Frezzotti, Nucl. Phys. Proc. Suppl. **119** (2003) 140 [arXiv:hep-lat/0210007].

[104] S. Weinberg, Phys. Rev. Lett. **17** (1966) 616.

[105] T. Becher and H. Leutwyler, JHEP **0106** (2001) 017 [arXiv:hep-ph/0103263].

[106] G. Höhler, F. Kaiser, R. Koch and E. Pietarinen, "Handbook Of Pion Nucleon Scattering," published by Fachinform. Zentr. Karlsruhe 1979, 440 P. (Physics Data, No.12-1 (1979)).

[107] H. Neuberger, Phys. Rev. Lett. **60** (1988) 889, Nucl. Phys. B **300** (1988) 180; P. Hasenfratz and H. Leutwyler, Nucl. Phys. B **343** (1990) 241; F. C. Hansen, Nucl. Phys. B **345** (1990) 685.

[108] M. Procura, T. R. Hemmert and W. Weise, Phys. Rev. D **69** (2004) 034505 [arXiv:hep-lat/0309020].

[109] T. Becher and H. Leutwyler, Eur. Phys. J. C **9** (1999) 643 [arXiv:hep-ph/9901384].

[110] Z. Sroczynski, "HMC for ALiCE," unpublished, Wuppertal (2002).

[111] W. Gropp and E. Lusk, ANL-96-6 (1996); ANL-96-5 (1996).

[112] Z. Sroczynski, Nucl. Phys. Proc. Suppl. **119** (2003) 1047 [arXiv:hep-lat/0208079].

[113] Z. Sroczynski, N. Eicker, T. Lippert, B. Orth and K. Schilling, arXiv:hep-lat/0307015.

[114] S. Gottlieb, W. Liu, D. Toussaint, R. L. Renken and R. L. Sugar, Phys. Rev. D **35** (1987) 2531.

[115] R. C. Brower, T. Ivanenko, A. R. Levi and K. N. Orginos, Nucl. Phys. B **484** (1997) 353 [arXiv:hep-lat/9509012].

[116] P. B. Mackenzie, Phys. Lett. B **226** (1989) 369.

[117] T. Lippert, Habilitationsschrift, Wuppertal (2001).

[118] T. Lippert *et al.* [TXL Collaboration], Nucl. Phys. Proc. Suppl. **63** (1998) 946 [arXiv:hep-lat/9712020].

[119] B. L. Ioffe, Nucl. Phys. B **188** (1981) 317 [Erratum-ibid. B **191** (1981) 591]; F. Fucito, G. Martinelli, C. Omero, G. Parisi, R. Petronzio and F. Rapuano, Nucl. Phys. B **210** (1982) 407.

[120] S. Güsken, Nucl. Phys. Proc. Suppl. **17** (1990) 361.

[121] A. Frommer, B. Nockel, S. Güsken, T. Lippert and K. Schilling, Int. J. Mod. Phys. C **6** (1995) 627 [arXiv:hep-lat/9504020].

[122] F. James, CERN Program Library Long Writeup **D 506** (1998).

[123] CERN Program Library, `http://cernlib.web.cern.ch/cernlib/`

[124] N. Eicker, Dissertation (in German), WUB DIS 2001 11, Wuppertal (2001).

[125] G. S. Bali *et al.* [TXL Collaboration], Phys. Rev. D **62** (2000) 054503 [arXiv:hep-lat/0003012].

[126] B. Bolder *et al.*, Phys. Rev. D **63** (2001) 074504 [arXiv:hep-lat/0005018].

[127] M. Albanese *et al.* [APE Collaboration], Phys. Lett. B **192** (1987) 163.

[128] G. S. Bali and K. Schilling, Phys. Rev. D **46** (1992) 2636.

[129] M. Fukugita, Y. Oyanagi and A. Ukawa, Phys. Rev. D **36** (1987) 824.

[130] S. Antonelli *et al.*, Phys. Lett. B **345** (1995) 49 [arXiv:hep-lat/9405012].

[131] J. Bijnens, G. Colangelo, G. Ecker, J. Gasser and M. E. Sainio, Phys. Lett. B **374** (1996) 210 [arXiv:hep-ph/9511397], Nucl. Phys. B **508** (1997) 263 [Erratum-ibid. B **517** (1998) 639] [arXiv:hep-ph/9707291].

[132] S. R. Beane, arXiv:hep-lat/0403030.

Danksagung

An erster Stelle möchte ich meinem Doktorvater, Herrn Prof. Dr. Klaus Schilling, für die Ermöglichung dieser Arbeit und sein Vertrauen danken. Seine Unterstützung, seine Diskussionsbereitschaft und seine Anregungen waren wesentliche Voraussetzungen für das Gelingen des Projekts. Mein großer Dank gilt ebenso Herrn Priv.-Doz. Dr. Dr. Thomas Lippert. Seine Ideen, seine Unterstützung und seine unermüdliche Einsatzbereitschaft haben mich immer wieder inspiriert und motiviert.

Beiden möchte ich besonders auch für ihre Verdienste um die Beantragung und Bereitstellung der technischen und organisatorischen Rahmenbedingungen danken, die für den Erfolg der Arbeit maßgeblich waren. Dazu gehören sowohl die erheblichen Computerressourcen der Universität und des NIC, zu denen ich Zugang hatte, als auch die finanzielle Unterstützung von Seiten der DFG und der EU, die mir im Rahmen eines Graduiertenkollegs und eines IHP Netzwerkes die Teilnahme an vielen interessanten wissenschaftlichen Begegnungen ermöglicht hat.

Für den reibungslosen Betrieb der Rechner des NIC in Jülich und Zeuthen möchte ich mich in diesem Zusammenhang bei den dortigen Kollegen und Kolleginnen bedanken.

Ein besonders herzlicher Dank gilt Herrn Dr. Stephan Dürr für einige wertvolle Diskussionen und die Bereitschaft, mir die nummerischen Daten zu seiner Arbeit über die Volumenabhängigkeit der Pionmasse zur Verfügung zu stellen.

Bei Thomas Düssel bedanke ich mich für seine Hilfe bei der Bestimmung von r_0.

Des weiteren möchte ich mich herzlich bei den Freunden und Kollegen bedanken, mit denen ich in Wuppertal eine schöne Zeit verbringen durfte. Dazu gehören besonders Dr. Hartmut Neff und meine Zimmergenossen Dr. Guido Arnold und Dr. Norbert Eicker. Letzterem danke ich auch für seine Hilfbereitschaft in vielen kleinen und größeren Computerangelegenheiten. Weitere, teils langjährige gute Wegbegleiter waren u.a. Dr. Sabrina Casanova, Dr. Nigel Cundy, Dr. Thorsten Feldmann, Priv.-Doz. Dr. Rainer Jakob, Stefan Krieg, Dr. Carsten Merten, Dr. Kornelija Passek-Kumericki, Dr. Oliver Passon, Zdravko Prkacin, Dr. Marcus Richter, Dr. Wolfram Schroers, Dr. Zbigniew Sroczynski, Dr. Thorsten Struckmann, Dr. Antonios Tsapalis, Dr. Jochen Viehoff, Dr. Carsten Vogt, sowie meine früheren Zimmerkollegen Bram Bolder, Thomas Moschny und Dr. Andreas Schmitz. In meiner Anfangszeit in Wuppertal konnte ich außerdem auf den Rat und die Hilfe von Priv.-Doz. Dr. Stephan Güsken und Prof. Dr. Peer Überholz zählen.

Ein besonderer Dank für ihre immer engagierte Hilfsbereitschaft gilt den Damen des Theorie-Sekretariats, Frau Anita Wied und Frau Sabine Hoffmann.

Schließlich möchte ich mich von ganzem Herzen bei meiner Familie bedanken, die mich von jeher in allen meinen Vorhaben unterstützt hat. Ihr bedingungsloser Rückhalt hat mir immer sehr viel bedeutet.

Zu guter Letzt gebührt meiner Freundin Renate mein aufrichtiger Dank für ihre Zuneigung und ihre unendliche Geduld.

Boris Orth

Wuppertal, Juni 2004